KU LEUVEN

ARENBERG DOCTORAL SCHOOL
Faculty of Engineering Science

Improved modeling and real-time simulation of near-range atmospheric dispersion of radioactive gases

Lieven Vervecken

Supervisor:
Prof. Dr. Ir. Johan Meyers
Dr. Johan Camps, co-supervisor

Dissertation presented in partial
fulfillment of the requirements for the
degree of Doctor in Engineering

October 2015

Improved modeling and real-time simulation of near-range atmospheric dispersion of radioactive gases

Lieven VERVECKEN

Examination committee:
Prof. Dr. Ir. Hugo Hens, chair
Prof. Dr. Ir. Johan Meyers, supervisor
Dr. Johan Camps, co-supervisor
Prof. Dr. Nicole Van Lipzig
Prof. Dr. Ir. Karl Meerbergen
Prof. Dr. Ir. Bert Blocken
(TU Eindhoven, Netherlands)
Dr. Spyros Andronopoulos
(NCSR Democritos, Greece)

Dissertation presented in partial
fulfillment of the requirements for
the degree of Doctor in Engineering

October 2015

Uitgegeven in eigen beheer, Lieven Vervecken, Celestijnenlaan 300 box 2420, B-3001 Heverlee (Belgium)

Preface

Dit werk is het resultaat van mijn doctoraatsonderzoek aan de KU Leuven, afdeling Toegepaste Mechanica en Energieconversie (TME), en het SCK • CEN, expertisegroep Maatschappij en Beleidsondersteuning (SPS), en kadert in het doctoraatsprogramma van de SCK • CENAcademy. Ik bestudeer hierin hoe de numerieke stromingsmechanica aangewend kan worden voor de simulatie van de verspreiding van radioactieve gassen. Dit boodt mij de kans om mijn kennis van de stromingsmechanica en nucleaire wetenschappen samen te brengen in één groot geheel. Met veel enthousiasme heb ik aan het doctoraat gewerkt en ik ben oprecht trots op het resultaat. Ik had echter niet tot dit punt kunnen komen zonder de hulp en steun van enkele personen tot wie ik graag een kort dankwoord richt.

Allereerst wil ik promotor professor Johan Meyers bedanken voor de uitgebreide begeleiding tijdens de afgelopen jaren. Op vrijwillige basis heeft hij de rol van promotor op zich genomen en deze rol heeft hij gedurende 4 jaar met veel enthousiasme vervuld. Ik kan oprecht stellen dat ik zonder onze talrijke inhoudelijke besprekingen, zijn feedback na presentaties en zijn input bij het schrijven van de papers, het doctoraat nooit tot dit niveau had kunnen brengen.

Even belangrijk bij de ondersteuning van dit werk was co-promotor Johan Camps. Zijn inzicht in het probleem en deskundige kennis van de stralingsbescherming hebben een onmiskenbare meerwaarde betekend bij de uitwerking van het project.

I would also like to thank all the members of my examination committee for their interest in my work and for critically reviewing the dissertation. The comments and suggestions they provided further improved the overall quality of the work.

Ook mijn collega's uit Mol en Leuven wil ik graag bedanken, en in het bijzonder diegene waarmee ik het kantoor heb gedeeld. Elk van hen heeft op zijn eigen manier bijgedragen tot de zeer positieve ervaring die ik aan dit doctoraat overhoud.

Het project zou ook niet tot stand zijn kunnen komen zonder de ondersteuning van de ICTS afdelingen van KU Leuven en SCK • CEN. Ongeacht het probleem stonden zij steeds klaar om mij verder te helpen en samen naar oplossingen te zoeken.

Een speciaal woord van dank richt ik graag tot mijn familie en vrienden. In het bijzonder denk ik dan aan mijn ouders en mijn drie zussen. Ondanks dat zij niet altijd begrepen waar ik juist mee bezig was, zijn zij mij steeds blijven steunen en interesse blijven tonen in mijn werk. Allerlaatst, maar niet allerminst, wil ik mijn vriendin An bedanken voor haar steun, begrip en oneindig geduld. Zij stond steeds klaar om samen successen te vieren en mij door de moeilijkere periodes heen te helpen.

Lieven Vervecken
Leuven, October 2015

Abstract

In the event of the release of a radiological pollutant into the atmosphere, a fast and accurate estimation of the pollutant dispersion is vital for the initial emergency assessment. To this end, many dispersion models have been developed to evaluate the impact of the release on the environment. Unfortunately, the limited ability to account for vegetation, buildings and other large structures in most of these models, restricts their applicability at the near-range, i.e. within the first few hundred meters from the nuclear installation. In recent years, Computational Fluid Dynamics (CFD) has proven to be a promising technique for atmospheric dispersion studies in the direct vicinity of the pollutant source, using either Reynold-Averaged Navier-Stokes (RANS) turbulence modeling or large eddy simulation (LES) turbulence modeling. Its main drawback however, is its computation speed which is by several orders of magnitude too slow for real-time emergency assessment. This thesis investigates how CFD can be applied in the context of nuclear emergency preparedness and response. The focus is on both improving the accuracy of CFD as a base model, and on the formulation of fast reduced order models (ROMs) that retain the accuracy of CFD.

We first focus on improving RANS modeling of atmospheric dispersion. The main advantage of performing RANS simulations is the lower computational cost compared to LES. A frequently recurring error corresponds to the observation of a large discrepancy in lateral plume spread between simulations and experimental data, combined with a significant overestimation of the concentrations in a vertical plane through the point of release and parallel with the wind direction. We argue that this is due to the fact that fluctuations in wind directions observed in experiments are only partly accounted for by the modeled turbulence. Therefore, a simple approach is introduced to estimate, based on experiments, the correct level of variability in wind direction that is required as additional boundary condition for the simulations. It is illustrated that including this unmodeled wind variability significantly improves predictions over traditional RANS models, and the Gaussian model.

A second part of this work looks into LES. The added value of LES over RANS is its improved accuracy which results from including the motion of the large eddies in the simulation. Accordingly, also the dispersion due to turbulent eddies is better captured. We make use of LES to study the variability of radiological dose rate at ground level due to instantaneous turbulent mixing processes. For this, the CFD model is coupled with dose rate models for beta and gamma radiation. By performing a set of time-dependent simulations of a constant release into an open field, the dose rate at ground level is computed. A large variability of the dose rate is observed. We show that the dose rate from gamma radiation can be reduced effectively by performing time-averaging. Yet, it is illustrated that neglecting this variability can result in errors up to a factor of four on the dose estimation when long-term measurements are used to estimate the resulting dose from short-term exposures. In case of beta radiation, variability in dose rate remains very high, even after averaging over a long time-period. These results indicate that the gamma dose measurements from nearby sensors cannot be used to accurately estimate the dose from beta radiation.

Finally, the third part of the work aims at constructing fast ROMs that retain full CFD accuracy. To this end, we focus on deriving a ROM by projection of the CFD model onto a Krylov-subspace that is produced by the Arnoldi algorithm. The method results in a stable ROM, and the algorithm is formulated in such a way that it can be used with any choice of CFD solver. First, the model reduction is applied to the forward simulation of the pollutant dispersion at the Doel Nuclear Power Station. It is illustrated that, after initialization, the ROM runs 25 times faster than real-time, including a possible dose assessment. Next, the model reduction methodology is used for the development of a method for the fast reconstruction of transient, multi-source emissions. The problem of the source reconstruction is formulated as a regularized least squares problem comparing the measurements to model predictions. By limiting the possible source locations to a finite number of possibilities, the Arnoldi algorithm can be applied to reduce the order of the problem. The size of the resulting system is reduced to such extent that the required time to solve the system is in the order of the simulated physical time span. Using a number of case studies, it is demonstrated that the method is both effective and robust for the source estimation of one or multiple possible sources from near-range measurements.

Beknopte samenvatting

Bij het vrijkomen van een radiotoxisch gas is een snelle en nauwkeurige inschatting van de verspreiding van het gas van vitaal belang voor de initiële beoordeling van het noodgeval. Hiertoe zijn er reeds verscheidene modellen ontwikkeld die de impact op de omgeving beoordelen in functie van de afstand tot het ongeval. Helaas zijn deze modellen slechts beperkt toepasbaar op de zone binnen een straal van enkele honderden meters van de nucleaire installatie. Vooral de beperkte mogelijkheid om vegetatie, gebouwen en andere grote structuren in rekening te brengen, speelt hierbij een belangrijke rol. De numerieke stromingsleer (CFD, *EN: Computational Fluid Dynamics*) heeft de laatste jaren bewezen een veelbelovende techniek te zijn voor dispersiestudies in deze zeer nabije omgeving van het ongeval. Hierbij wordt voor de modellering van de turbulentie in het windveld zowel van Reynolds-gemiddelde Navier-Stokesvergelijkingen (RANS) als van simulaties van grote wervelingen (LES, *EN: large eddy simulations*) gebruik gemaakt. Het belangrijkste nadeel van deze techniek is echter dat de berekeningssnelheid meerdere grootteorden te klein is om inzetbaar te zijn in noodsituaties. In deze thesis wordt bestudeerd hoe CFD in de context van paraatheid en reactie op nucleaire noodsituaties kan worden aangewend. De focus ligt hierbij zowel op het verbeteren van de nauwkeurigheid van CFD als basismodel, als op de ontwikkeling van snelle, lagere orde modellen die de nauwkeurigheid van CFD behouden.

We richten ons eerst op het verbeteren van het modelleren van de atmosferische dispersie met RANS. Het belangrijkste voordeel van het gebruik van RANS simulaties is de lagere rekenkost in vergelijking met LES. Een vaak geobserveerde afwijking tussen experimenten en traditionele RANS-simulaties uit zich in een aanzienlijke onderschatting van de laterale pluimbreedte en een sterke overschatting van de concentratie in het vlak doorheen de bron en parallel aan de windrichting. We stellen dat dit te wijten is aan het feit dat slechts een deel van de variaties in windrichting door de gemodelleerde turbulentie in rekening wordt gebracht. Daarom wordt een eenvoudige methodiek geïntroduceerd die op basis van experimenten toelaat om de hoeveelheid

niet-gemodelleerde variabiliteit af te schatten. Deze afschatting is nodig als bijkomende randvoorwaarde voor de RANS-simulaties van de gasdispersie. We tonen aan dat het in rekening brengen van niet-gemodelleerde variaties in windrichting de voorspellingen significant verbeteren in vergelijking met de traditionele RANS-simulaties en het Gaussiaans model.

Een tweede deel van dit werk maakt gebruik van LES. De toegevoegde waarde van LES ten opzichte van RANS is de grotere nauwkeurigheid. Deze volgt rechtstreeks uit het in rekening brengen van de grote wervelingen in het windveld. Overeenkomstig hieraan wordt ook de verspreiding van het gas ten gevolge van turbulente wervelingen beter voorgesteld. We gebruiken LES om de variabiliteit in radiologisch dosistempo ten gevolge van turbulente mengprocessen te bestuderen. Hiertoe wordt het LES model gekoppeld aan modellen voor het bepalen van het dosistempo door bèta- en gammastraling. Een reeks dispersiesimulaties over een open veld met constant uitstootdebiet toont de grote variabiliteit in ogenblikkelijke dosistempo's. We illustreren dat met tijdsgemiddelde metingen de variabiliteit in dosistempo van gammastraling wel doeltreffend kan worden verminderd. Dit tijdsmiddelen kan echter resulteren in fouten tot een factor vier wanneer metingen over langere periodes worden gebruikt voor de afschatting van de dosis ten gevolge van een korte blootstelling. Bij bètastraling blijft na tijdsmiddelen, zelfs over een lange periode, de variabiliteit zeer hoog. Dit wijst erop dat dosismetingen van gammastraling niet gebruikt kunnen worden voor een betrouwbare afschatting van de dosis door bètastraling.

Het laatste deel van deze thesis beoogt de ontwikkeling van een lagere orde model dat een kortere rekentijd vraagt maar de nauwkeurigheid van CFD simulaties behoudt. In het bijzonder leggen we ons toe op de modelreductie van het CFD-model door projectie op een Krylov-deelruimte. Deze deelruimte wordt opgebouwd aan de hand van het Arnoldi algoritme. Het algoritme wordt zodanig geformuleerd dat het kan worden gebruikt met eender welk CFD-softwarepakket. We illustreren dat na initialisatie, deze methode resulteert in een 2500 maal snellere simulatie, inclusief een mogelijke dosistempoberekening. Vervolgens wordt deze methode gebruikt voor de snelle en accurate reconstructie van één of meerdere tijdsafhankelijke bronnen op basis van metingen in de zeer nabije omgeving. Het probleem wordt geformuleerd als een geregulariseerd kleinste-kwadratenprobleem waarbij metingen met voorspellingen worden vergeleken. Door het aantal mogelijke bronnen te beperken tot een eindig aantal opties kan modelreductie worden toegepast. Hierdoor reduceert het aantal vrijheidsgraden sterk waardoor de simulatietijd afneemt tot dezelfde grootteorde als de gesimuleerde fysische tijd. Met behulp van enkele casestudies wordt aangetoond dat de voorgestelde methode zowel doeltreffend als robuust is.

Nomenclature

Abbreviations

ABL	Atmospheric Boundary Layer
CFD	Computational Fluid Dynamics
DOF	Degrees of freedom
FANC	Federal Agency for Nuclear Control
GCI	Grid Convergence Index
IAEA	International Atomic Energy Agency
ICRP	International Commission on Radiological Protection
LES	Large-Eddy Simulation
MOR	Model Order Reduction
NERIS	European Platform on Preparedness for Nuclear and Radiological Emergency Response and Recovery
PDE	Partial Differential Equation
RANS	Reynolds-Averaged Navier–Stokes
RODOS	Real-time Online DecisiOn Support
ROM	Reduced Order Model
SGS	Subgrid-scale

Roman symbols

A	Discrete representation of the advection and the diffusion operator
b	Source vector
B	Buildup factor
c	Concentration
$c_{s,\Delta}$	Smagorinsky coefficient
C	Output matrix
$\dot{d}_\beta$	Radiological dose rate from beta radiation
$\dot{d}_\gamma$	Radiological dose rate from gamma radiation

$\bar{E}_\beta$	Average beta energy released per disintegration
E_γ	Gamma energy released per disintegration
f	Coriolis parameter
FB	Fractional bias
FAC2	Fraction of predictions within a factor of two of observations
FAC10	Fraction of predictions within a factor of ten of observations
k	Turbulent kinetic energy
K	Unit conversion factor
G	Filter convolution kernel
H	Pollutant release height
$\mathcal{J}$	Cost functional
$\mathcal{K}_r$	Krylov subspace of order r
L	Reference length; Monin-Obukhov length
n	Number of grid cells
nt	Number of time steps
N	Number of measurements
M	Number of measurement locations
NMSE	Normalized mean square error
p	Pressure
P_k	Turbulent production term
r	Order of the ROM
R	Reference pollutant release rate
Re	Reynolds number
S	Strain rate tensor; Number of source locations
S_p	Pollutant source term
Sc_t	Turbulent Schmidt number
Sc_{sgs}	SGS Schmidt number
t	Time
T	Measurement time horizon
$\boldsymbol{u}$	Velocity
u_τ	Friction velocity
U	Reference velocity
v	Column of matrix V
V	Domain volume; Projection matrix
VG	Geometric variance
y	Output vector
z_0	Roughness length

Greek symbols

α	Instantaneous wind angle
β	Regularization parameter

δ	Boundary layer thickness
Δ	LES filter width
ε	Dissipation rate of the turbulent kinetic energy
γ	Regularization parameter
κ	Von Kármán constant
λ	Radioactive decay constant
μ	Linear attenuation coefficient in air
μ_{en}	Energy absorption coefficient
ν	Kinematic viscosity
ν_t	Turbulent viscosity
ν_{sgs}	SGS eddy viscosity
Ω	Physical domain
ϕ	Gamma fluence rate
ϕ_M	Stability function
ψ	Output function ($y = f_i(c)$)
Ψ	Discrete representation of f_i
ρ	Density of the receptor
ρ_0	Air density
σ	Standard deviation; Pollutant source
ς	Adjoint concentration
$\boldsymbol{\tau}$	Stress tensor
τ_w	Wall shear stress

Subscripts

CFD	Solution of the CFD model
e	Incorporated as an external boundary condition
E	Experimental value
i	Cell i
m	Representend in a CFD model
r	Reduced order quantity
ROM	Solution of the ROM
S	Simulated value
$\boldsymbol{x}_0$	At location $\boldsymbol{x}_0$
x, x_1	Streamwise direction
y, x_2	Spanwise direction
z, x_3	Vertical direction

Superscripts

k	Time step index k
r	Order of the reduced model

Miscellaneous symbols

$\langle\cdot\rangle$	Time average
$\tilde{\bullet}$	Quantity filtered at grid scale; Discrete quantity
$\hat{\bullet}$	Quantity filtered at test-filter scale; Measurement
$\overline{\bullet}$	Quantity filtered at a second test-filter scale; Reduced order quantity
$()'$	Fluctuating part in Reynolds decomposition ($\phi = \langle\phi\rangle + \phi'$)
$()^T$	Transpose of a matrix
$()^*$	Non-dimensional symbol; Matrix of the inverse system

Contents

List of Figures

List of Tables

Chapter 1

Introduction

Nuclear and radiological accidents from the past have demonstrated the detrimental impact radiotoxic clouds can have on the environment (see, e.g., Ref. [85]). A proper estimation of the pollutant dispersion and the resulting dose received by the general public after a release of radionuclides in the atmosphere is indispensable to minimize possible health risks during the nuclear emergencies [68]. To that end, the International Commission on Radiological Protection (ICRP) and the International Atomic Energy Agency (IAEA) provide recommendations and guidance on protection against ionizing radiation. These recommendations are commonly used as basis for the local legislation of countries. In Belgium, the Royal Decree KB 17/10/2003 specifies the nuclear and radiological emergency planning for Belgium and is motivated by these recommendations. Among others, this decree obliges the large nuclear facilities to have computational models at their disposal for the impact assessment up to a few tens of kilometers downwind from the point of release.

In particular during the emergency preparedness and response phases, impact assessment models are of great use. For instance, the models allow to simulate hypothetical accident scenarios during the preparedness phase. Such exercises serve to ensure that individuals and authorities are able to respond effectively to nuclear accidents, e.g. by the development of response plans and by training in communication. In case of a real accident, models are first used for the localization and the reconstruction of the source by exploiting measurement data. Next, the computed source term serves as input to perform the impact assessment at other locations. Based on the predicted impact, effective countermeasures can be defined and imposed.

The emergency response phase is usually triggered by the detection of a

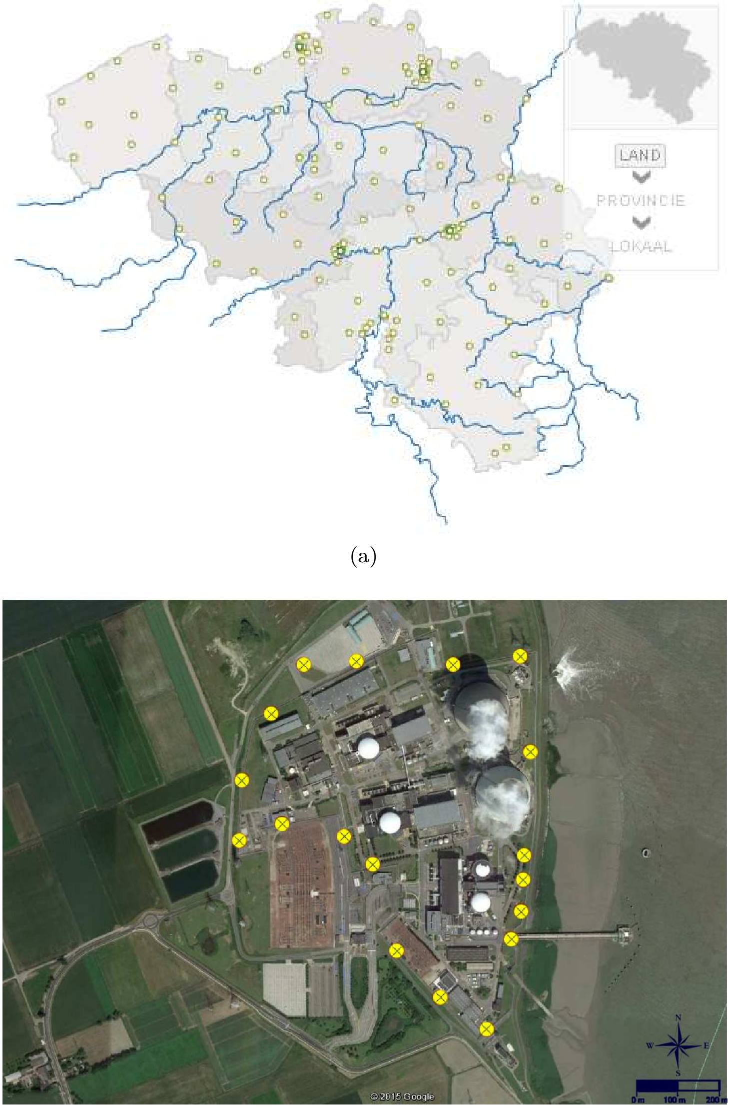

(a)

(b)

Figure 1.1: Telerad measurement stations (a) in Belgium (figure retrieved from http://www.telerad.fgov.be on June 24, 2015 [46], reprinted with permission), and (b) at the Doel Nuclear Power Station.

radiological dose rate above a certain threshold by a radioactivity detection network. The Belgian TELERAD network is an example of such a radioactivity detection network. It continuously monitors the radioactivity in the air, providing time-integrated dose rate measurements every 10 minutes [128]. The network consists of more than 200 measurement stations placed all over Belgium on a grid of 20 km by 20 km as shown in Fig. 1.1a. In the vicinity of nuclear installations the measurement stations are placed more densely. This is illustrated in Fig. 1.1b for the Doel Nuclear Power Station, located to the North of Antwerp (Belgium) on the left bank of the river Scheldt. Note that the placement of the measurement stations this densely at the near-range, i.e. within a few hundred meters from the nuclear installation, is particularly favorable for rapid pollutant detection after an accident.

The aim of this dissertation is to investigate the atmospheric dispersion of radioactive gases at the near-range in the framework of nuclear emergency preparedness and response. To this end, Computational Fluid Dynamics (CFD) and model reduction techniques are studied. It is the aim to be able to perform real-time simulation of the pollutant dispersion so that the rapid pollutant detection at the near-range can be effectively exploited. In the next sections, first the state of the art is introduced on atmospheric dispersion assessments, with a focus on numerical simulations. Real-time simulation of near-range dispersion is discussed next, followed by a discussion on the use of Reynolds-Averaged Navier–Stokes (RANS) and Large-Eddy Simulations (LES) for dispersion simulations. In Section 1.4, the aims and objectives of this work are specified, and in Section 1.5 the outline of the thesis is presented.

1.1 State-of-the-Art

In order to assist in the optimization of the protection strategy after a nuclear accident, on-line risk management tools such as RODOS (Real-time Online DecisiOn Support) are being developed (see, e.g., Ref. [137], or Ref. [77]). To this end, fast and accurate models for the atmospheric dispersion of the radioactive nuclides released are crucial [80].

The difference in dispersion models is in the first place determined by the modeled region of interest in terms of the distance to the pollutant source. Depending on the distance, the transport is dominated by atmospheric disturbances at different scales. The scales can be related to atmospheric effects dominating at the near-range, the local range, the regional scale and the long range. Multiple definitions are found in the literature to define the different scales. For instance, these can be based on a temporal scale such as the diffusion time (see, e.g., Ref. [20]), or a spatial scales related to the atmospheric motion (see, e.g., Ref. [43]). Overall, the near-range is approximately found from the location of release up to a few kilometers. At this scale, local turbulence and geometrical features in the landscape such as buildings, cooling towers and vegetation are very important. At the local scale, local thermal circulations and landscape characteristics dominate what occurs from a few up to about 50 km from the source. The regional scale is found next and transitions into the long range from about 500 km upward. Since the dominant scales can allow to make physical assumptions and mathematical approximations, a model is often developed for a particular scale of interest. Extensive discussions on different atmospheric dispersion models, including their advantages and limitations, are presented by Holmes and Morawska [65] and Leelőssy *et al.* [80]. In the following, we briefly present three of the main classes of air pollution modeling tools: Gaussian models, Lagrangian models, and CFD models. A schematic representation of the principle behind the different modeling methods presented is shown in Fig. 1.2.

Gaussian models are widely used to simulate the dispersion of a pollutant at the local scale. The analytical model is derived from the advection-diffusion equation by assuming a uniform, steady-state wind field and a steady-state point source. This results in a concentration profile that is constant in time and that follows a Gaussian profile in span-wise and vertical direction. The profile is a function of the pollutant release rate, the mean horizontal wind velocity, the pollutant release height, and the standard deviations σ_y and σ_z which describe the span-wise and vertical distribution. These standard deviations are often derived from experiments and expressed as a function of the downwind distance and the atmospheric stratification (see, e.g., Ref [24] and Ref. [22]). Because of their simplicity, Gaussian models are among the fastest models available. Examples of Gaussian models used at present include AERMOD [35], ADMS [27] and ALOHA [107]. An extension to the Gaussian model is used in the NOODPLAN models, which have been developed at SCK • CEN. The dispersion at the local scale is modeled using a segmented bi-Gaussian plume approach [26]. In this approach, the plume is broken up into plume segments corresponding to fixed time periods of 10-minutes. This enables to account for time-varying releases and changes in atmospheric conditions. The shape of the plume segments is determined using the Bultynck-Malet dispersion parameters [24] although a correction is applied to account for the difference in original sampling time and the 10-minute periods. A customized version of the NOODPLAN models is available for the Nuclear Power Plans at Doel, at Tihange and for the nuclear facilities in Mol. An example of the output from the Tihange NOODPLAN model is shown in Fig. 1.3.

Instead of a continuous release, a series of consecutive released puffs or particles

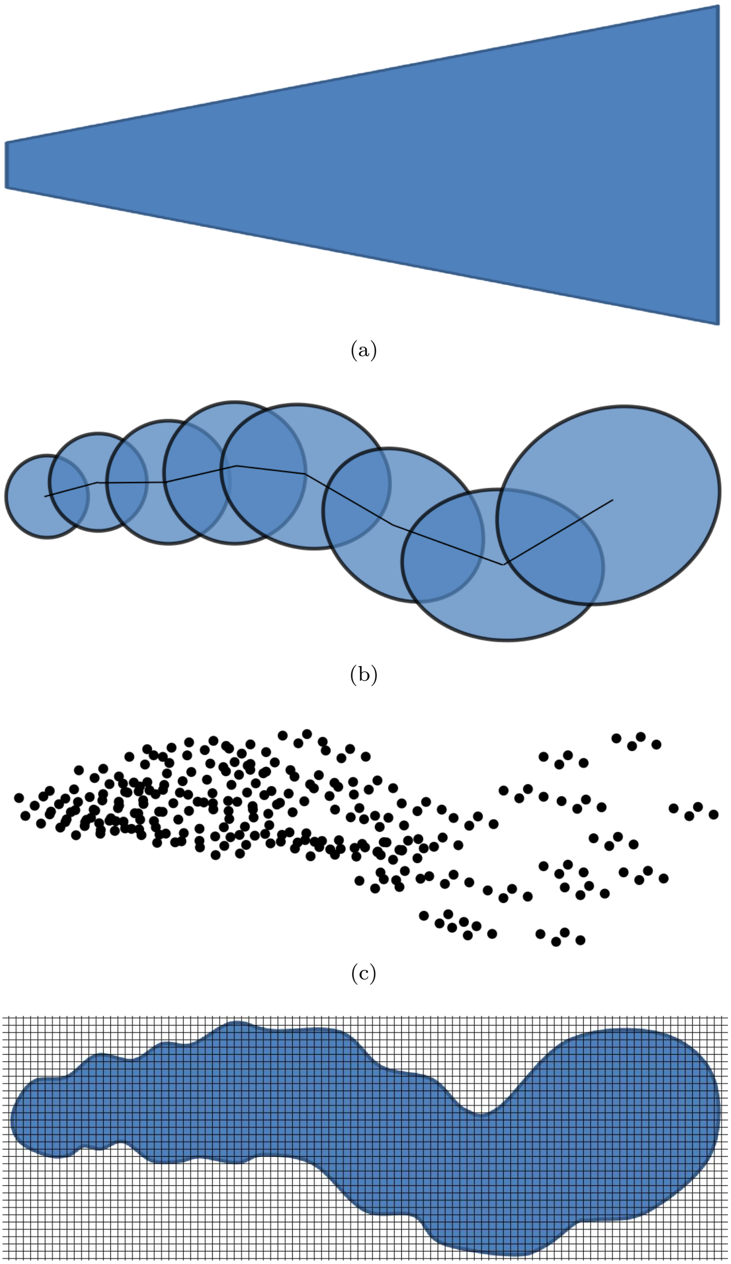

(a)

(b)

(c)

(d)

Figure 1.2: Graphical representation of the principle behind (a) Gaussian models, (b) Lagrangian puff models, (c) Lagrangian particle models, (d) CFD models.

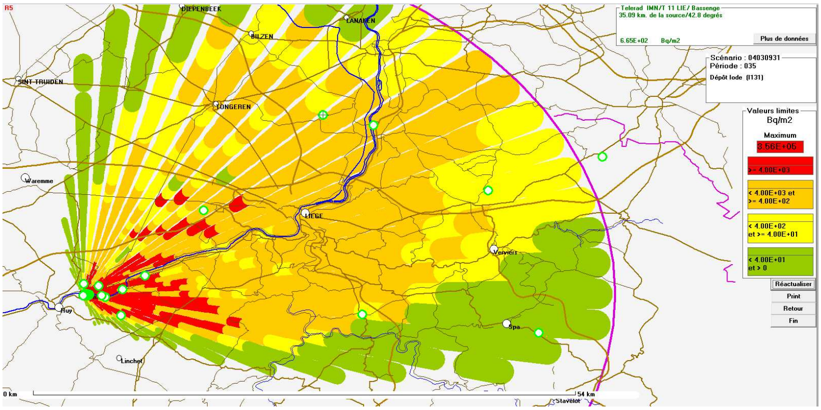

Telerad IMN/T 11 LIE/ Bassenge
35.09 km. de la source/42.8 degrés
6.65E+02 Bq/m2

Scénario : 04030931
Période : 035
Dépôt Iode (I131)

Valeurs limites
Bq/m2
Maximum 3.56E+05
🟥 >= 4.00E+03
🟧 < 4.00E+03 et >= 4.00E+02
🟨 < 4.00E+02 et >= 4.00E+01
🟩 < 4.00E+01 et > 0

Figure 1.3: Illustration of the NOODPLAN model output for a hypothetical accident at Tihange Nuclear Power Station.

is used to simulate the release in Lagrangian models. Depending on the model, a one-, two- or three-dimensional wind field is required as input. This is typically computed by a separate flow field model or it is constructed based on meteorological data. In Lagrangian puff models, a puff is modeled as a three-dimensional Gaussian distribution of concentration within the puff volume. The puff is therefore characterized by the location of the center and three diffusion parameters σ_x, σ_y and σ_z. Models predict the trajectory of the center and the evolution of diffusion parameters. The total concentration is obtained by adding up every puff in the domain. For instance RIMPUFF [135] and CALPUFF [120] operate with this method. A variation on this type of modeling is used in ATSTEP. This model simulates the dispersion of airborne radioactive contaminants using time-integrated elongated puffs instead of a larger number of tri-Gaussian puffs [98]. Lagrangian particle models represent the pollutant using a discrete number of computational particles as shown in Fig. 1.2c. The particles are transported along the given wind field, possibly with the addition of a random component as a way to account for turbulence. The computational domain is divided in separate cells and the number of particles in each cell is determined. By summing the loads of the particles in each cell and subsequently dividing the sum by the cell volume, the mean concentration in each cell is obtained. The dispersion models DIPCOT [4] and LASAT [70] are examples of these types of models, but note that DIPCOT can also operate as Lagrangian puff model.

In most of the Gaussian and Lagrangian local range models, different parametrization or additional correction factors can be applied to the account for, among others, plume rise, building down wash, and deposition [59, 127].

Yet, the accuracy of these corrections are strongly site-dependent. The limited ability to include buildings, vegetation and other large structures in particular can hamper the accurate extrapolation of the local scale dispersion models to the near-range. To deal with this, dedicated Lagrangian models have been developed for the near-range as well. Examples are QUIC [154] and Micro-SWIFT [89]. These models often use empirical algorithms and mass conservation to quickly compute 3D flow fields around building complexes. The dispersion calculation is performed next assuming that the pollutant does not influence the flow field. While these models can run relatively fast, their accuracy is again strongly pollutant- and site-dependent.

In recent years, CFD has proven to be a promising technique for atmospheric dispersion studies at the near-range [62, 140, 18, 141]. Either using Reynolds-Averaged Navier–Stokes (RANS) simulations or Large-Eddy Simulations (LES), CFD offers a large potential to increase the accuracy of the dispersion simulation with respect to existing models. This is particularly true for the built environment where the complex geometry can result in complex dispersion patterns [17, 78, 53, 58]. CFD is already frequently employed in the context of radiological protection. Vach and Duong [147] performed a series of CFD simulations to quantify the ground concentration and deposition fields of passive particles presumably emitted from a nuclear power plant. The radioactive plume was represented as a collection of Lagrangian particles which were dispersed on a steady velocity background obtained using RANS turbulence modeling. A similar approach was followed by Gallego *et al.* [50] in their effort to analyze the traveling distance of radioactive particles, emitted by a nuclear power plant. Despite the fact that no gamma dose assessment was performed in these studies, Raza and Avila [105] illustrated that the resulting dose from these particles can be computed by treating each as a point source and by adding the contribution from each particle in the domain. Instead of using the Lagrangian description, Xie *et al.* [157] followed an Eulerian approach in combination with a RANS simulation of the wind field to simulate the dispersion of ^{222}Rn released from a uranium mine ventilation shaft. Subsequently, the effective dose rate to the public was estimated by multiplying the resulting concentration with dose conversion factors [158]. Also Duarte *et al.* [39] applied this approach for the radiological assessment of the fall of a radioactive waste package. Instead of RANS, de Sampaio *et al.* [37] used LES modeling and examined the time-evolution of the dispersion of radionuclides in the vicinity of nuclear power plants, illustrating the importance of the local phenomena on the dispersion problem. Also Fuka and Brechler [49] and Nakayama *et al.* [90] employed LES to simulate the dispersion of radioactive matter.

Recently a model inter-comparison study on near-range dose rate calculations

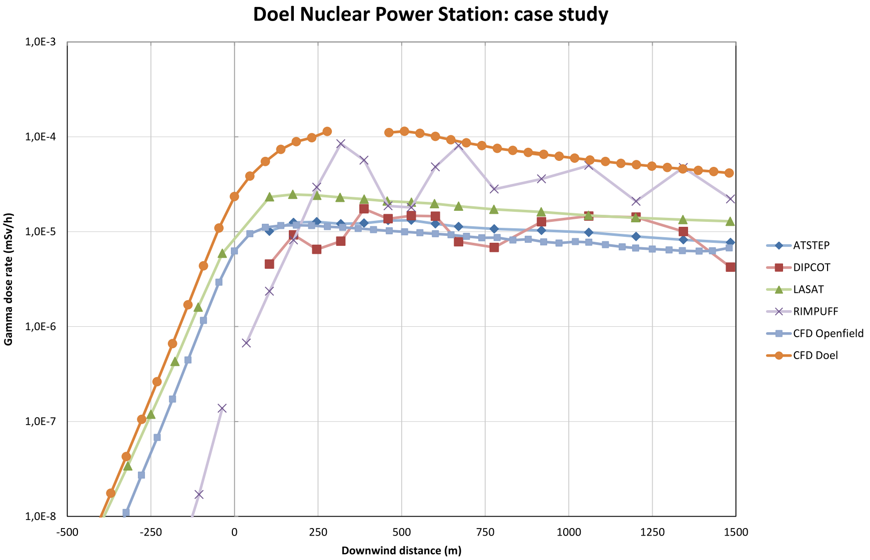

Figure 1.4: Comparison between four dose-assessment models implemented in RODOS and two CFD models.

using local scale models was performed by Gueibe *et al.* [56]. The Doel Nuclear Power Station was the subject of interest. More precisely, the resulting dose from a steady release from the Doel 3 chimney, emitting Xenon-133 at a rate of 3.6 TBqh^{-1}, was compared using widespread dispersion models implemented in RODOS, the Doel NOODPLAN model, and a custom Comsol Multiphysics model. For the study, the wind was set to come from the southwest, which is the prevailing wind direction for this location, the wind speed is set to 20 km h^{-1} at stack height (74 m), and a thermally neutral atmospheric boundary layer (ABL) was assumed. In Fig. 1.4, the results of the RODOS models included in the study are shown together with the results of two CFD models. The 'CFD Doel' model includes the buildings present on-site in the simulation while the 'CFD Openfield' simply assumes an open field (see Chapter 2 for the model details). The gamma dose rate in an open field is comparable to the RODOS models. This is expected as many of the local models predict the dispersion based on wind fields that do not take the buildings into account. However, a non-negligible increase in dose rate at the near-range is found in case the buildings are taken into account ('CFD Doel'). In particular within the first few hundreds of meters to the source, this difference runs up to more than an order of magnitude. The effect of this difference is twofold. Firstly, if the source term is estimated based on near-range measurements using models that cannot effectively account for the buildings, it is likely to get significantly overestimated. When the estimated source term is subsequently applied to long-range models, overly conservative countermeasures might be taken at longer distance. Secondly, when the effective dose to the employers on site is estimated using a known source term, models that do not accuractely include the buildings are likely to result in a significant underprediction.

1.2 Real-time simulation of near-range dispersion

Ideally, the source reconstruction after the pollutant detection and subsequently the model evaluation determining the impact at other locations runs faster than real-time. Despite the wide range of models available, Leelőssy *et al.* [80] identified that there is currently no accurate near-range atmospheric dispersion modeling approach available with a runtime comparable to Gaussian or Lagrangian models. Also the European Platform on Preparedness for Nuclear and Radiological Emergency Response and Recovery (NERIS) set improving the near-range and urban modeling of atmospheric releases of radiological or nuclear material as a priority. Their objective is to extend the capabilities of decision support systems to improve the reliability and the precision of atmospheric dispersion predictions [40].

The near-range can be specifically interesting to determine the location and the magnitude of the maximal impact of potential releases which might occur close to the release point. Also the planning of evacuation routes, the impact assessment on the operators mitigating an incident, and the optimization of the monitoring equipment locations around the site can be addressed by an effective near-range dispersion model. However, most of all, a fast and accurate model would be particularly useful for the real-time estimation of the release rate based on data assimilation of near-range measurements since this can provide essential input to models effective at other scales. Much attention is devoted to address this challenge, focusing on single point sources [72, 123], multiple point sources [124, 126, 150], steady state release [2, 126] and transient releases [2, 57, 161]. The source inverse modeling can be categorized into probabilistic and optimization methods [146, 162]. The former focus on reconstructing probabilities of the source parameters. These techniques are often based on Bayesian inference [72, 150] and Markov chain Monte Carlo sampling [33, 57]. Although other methods such as minimum relative entropy method are also found [84]. With the optimization approach, the source parameters are chosen such that a predefined objective, e.g. the error between simulation and measurements, is minimized [2, 74, 83, 126]. Each of these methods may require several iterations, requiring the forwards and/or backward model to be solved multiple times. Application of the methods to a full size CFD model is therefore often considered computationally too expensive [60, 84, 91, 118]. Because of this lack of a fast model for accurate source characterization of one or multiple simultaneous sources, Gaussian-based models or other simplified models are used instead (See, e.g. Ref. [83, 84, 113]).

In an endeavor to reduce the computational cost of running CFD models, Senocak *et al.* [122] focused on reducing the simulation time by improving the numerical methods and parallel computing strategies. Gowardhan *et al.* [54] chose to trade some of the accuracy for a gain in simulation speed by simplifying the model. Alternatively, a reduced order model (ROM) might be derived from a CFD model but this has not been explored in the past. As indicated below, this will be a part of the objectives of this dissertation.

1.3 RANS and LES for dispersion simulations

Both RANS and LES turbulence modeling are used in atmospheric dispersion studies. The main advantage of performing RANS simulations is the lower computational cost compared to LES. This is due to the fact that in RANS all turbulence is modeled while in LES only smaller eddies are modeled, i.e. the motion of the largest eddies is included in the simulation. LESs are therefore inherently unsteady and a longer time period needs to be simulated to obtain a statistically converged result. The main advantage of LES over RANS however, is its improved accuracy, and the fact that dispersion due to turbulent eddies is better captured. To date however, no LES model has been coupled to radiological dose models to assess the effect of the turbulence in the atmospheric boundary layer. Such an analysis of a time-dependent simulation can provide keen insight into the behavior of the radiological dose rate at ground level.

One of the major challenges associated with RANS modeling in atmospheric dispersion simulations is accuracy. A frequently recurring error corresponds to the observation of a large discrepancy in lateral spread between simulations and experimental data, combined with a significant overestimation of the concentrations in a vertical plane through the point of release and parallel with the wind direction. These observations occur both in simple open-field studies [29, 38, 61, 67, 76, 109, 132], and in studies with more complicated geometry, such as buildings [15, 17, 61, 67, 104, 109]. It has been suggested repeatedly that this is due to an underestimation of the turbulent diffusion by the RANS model [15, 29, 38]. Therefore, e.g., Chan *et al.* [29] and Bellasio and Tamponi [15] introduced an anisotropic diffusion coefficient to cope with this issue, while Demael and Carissimo [38] simply added a constant value in the horizontal direction to the effective diffusivity. However, other authors link deficiencies in lateral spreading to effects of non-stationary wind conditions. Hanna *et al.* [61] applied non-stationary inflow boundary conditions to include a meandering effect in the wind field, effectively increasing the horizontal diffusion as well. Labovský and Jelemenský [76] also used non-stationary boundary conditions, in this case to impose experimentally measured atmospheric data at the inflow boundary. In similar approaches, Quinn *et al.* [104], and Tang *et al.* [132] weighted a set of steady-state RANS solution over the distribution of wind directions, changing their single-wind CFD model to a time-averaged variable-wind CFD model. This weighting approach was further carefully studied by Huber *et al.* [67] who notes that lateral spreading of pollutants is now significantly overpredicted.

1.4 Aims and Objectives

The purpose of the PhD is to investigate the near-range atmospheric dispersion modeling in the context of preparedness and response to nuclear emergencies. Three main objectives are pursued in this work. The first is related to the improvement of current modeling techniques, the second and the third are related to the real-time simulation of the pollutant dispersion. More specifically, the objectives for the current dissertation can be summarized as follows:

1. The improvement of the accuracy of near-range atmospheric dispersion simulations of radioactive gases. To this end, the variability in wind direction in RANS simulations is studied thoroughly. In addition, the variability of radiological dose rate from cloud shine due to instantaneous turbulent mixing processes is examined through LESs.
2. The development of a fast model for the time-dependent pollutant dispersion simulation in the built environment. In particular, the construction of a Reduced Order Model (ROM) using the often employed Arnoldi algorithm is targeted.
3. The development of a model for fast pollutant source identification and source reconstruction based on time-dependent near-range measurements. The problem is formulated as an optimization problem to which the ROM methodology can be applied.

An Eulerian approach is followed for the simulation of a non-buoyant, non-reactive gas in a neutral atmospheric boundary layer. The main advantage of imposing these restrictions is that the momentum equation and the scalar equation for the pollutant become fully decoupled. Such an approach is common for simulations of the near-range atmospheric dispersion using RANS [17, 18, 53, 109] or LES [28, 37, 114, 129]. Despite these restrictions, the model is well-suited for the simulation of the dispersion of (radioactive) noble gases such as ^{41}Ar and ^{133}Xe in a neutral ABL. These gases are inert and do not deposit. Both are frequently emitted in routine operation of various nuclear facilities [66, 111] and especially ^{133}Xe might be emitted in large quantities during nuclear accidents [42].

Throughout the text, the Doel Nuclear Power Station will serve as case study to illustrate the different methodologies developed. As shown in Fig. 1.1b, the site includes four reactor buildings, two hyperbolic cooling towers with a height of 176 m, and multiple other auxiliary buildings. The atmospheric conditions are taken the same as Gueibe *et al.* [56], i.e. wind is set to come from the southwest, the wind speed is set to 20 km h^{-1} at stack height (74 m), and a neutral boundary layer is presumed.

1.5 Outline

Chapter 2 introduces the governing equations for atmospheric dispersion modeling and presents the notation used in the text. In Section 2.2, the RANS equations are presented. Next, the LES equations are introduced in Section 2.3. The applied dose rate models for beta radiation and gamma radiation are discussed in Section 2.4. Finally, the practical implementation is discussed in Section 2.5

In Chapter 3, the variability in wind direction in RANS simulations is studied. In Section 3.1, a simple approach is proposed to estimate the wind direction variability taken into account by the RANS turbulence model. Further, the dispersion model used for the simulation is presented, including an extension towards thermal stratification. Subsequently, in Section 3.2 we detail the experiments that are considered in the current work, the numerical set-up of our simulations, and also briefly discuss a set of criteria to compare simulations to experiments. We test the approach by performing a series of dispersion simulations of the well- documented Prairie Grass experiments, and demonstrate that simulations improve significantly in Section 3.3. Finally, conclusions are presented in Section 3.4.

In Chapter 4, the variability of radiological dose rate from cloud shine due to instantaneous turbulent mixing processes is studied. To this end, LES is used to reconstruct the time-evolution of the turbulent dispersion of radioactive gases in the ABL, and it is coupled to a gamma dose rate model that is based on the point-kernel method with buildup factors. Section 4.1 details the numerical set-up of our simulations, The results of simulations are discussed in Section 4.2 with a particular focus on the variability of dose rates at ground level for different averaging times in the dose measurements. A summary of the conclusions are presented in Section 4.3.

Chapter 5 introduces an effective model reduction method that is based on the projection of the original model, which solves the transient advection-diffusion equation on a steady background velocity field, onto a Krylov subspace by means of the Arnoldi algorithm. The accuracy of the ROM is illustrated by performing a series of simulations of a time-dependent pollutant release at the Doel nuclear power station, located to the north of Antwerp (Belgium). First, in Section 5.1, we present the model order reduction methodology and we formulate the algorithm in such a way that the ROM can be derived using any CFD software package, commercial or non-commercial. Next, in Section 5.2 we detail the simulation cases considered in the current work and the numerical set-up of our simulations. Simulation results are discussed in Section 5.3. Finally, conclusions are presented in Section 5.4.

Subsequently, in Chapter 6, we focus on the development of a fast inverse modeling approach. Based on time-dependent measurements in the domain, the location and emission rates of time-dependent pollutant sources are identified and reconstructed. In Section 6.1, the problem is formulated as a regularized, least squares minimization problem and the first-order optimality conditions are discussed. In Section 6.2 a direct solution method using ROMs is presented. The cases studied are detailed in Section 6.3 and simulation results are elaborated in Section 6.4. The conclusions are presented in Section 6.5.

Finally, in Chapter 7, the main conclusions of this work and possible future research directions are discussed.

Chapter 2

Governing equations for atmospheric dispersion of radioactive gases

This chapter introduces the governing equations for the simulation of the dispersion in a neutral ABL, and presents the notation that is used in the text. We use an Eulerian approach to formulate the dispersion of the radionuclide as a transient three-dimensional advection-diffusion problem with radioactive decay. In Section 2.1, the incompressible Navier–Stokes equations for mass and momentum are introduced and the connection to RANS and LES turbulence modeling is explained. Next, the dispersion modeling using RANS simulation and LES is detailed in Section 2.2 and Section 2.3, respectively. The models for the computation of the radiological dose from beta radiation and from gamma radiation are subsequently presented in Section 2.4. Finally, the practical implementation is discussed in Section 2.5.

2.1 Navier–Stokes equations

The flow in an neutral atmospheric boundary layer can be described by the solution of the incompressible Navier–Stokes equations for mass and momentum. By taking L as a characteristic length scale, U as a characteristic velocity scale, ρ_0 as the air density, and by modeling the air as a Newtonian, homogeneous and isotropic fluid, the non-dimensionalized Navier–Stokes equations can be written as [101]

$$\nabla^* \cdot \boldsymbol{u}^* = 0, \tag{2.1}$$

$$\frac{\partial \boldsymbol{u}^*}{\partial t^*} + \boldsymbol{u}^* \cdot \nabla^* \boldsymbol{u}^* = -\nabla^* p^* + \frac{1}{Re} \nabla^2 \boldsymbol{u}^*, \tag{2.2}$$

where $Re = \rho U L / \mu$ is the Reynolds number with μ the dynamic viscosity of air, and where we introduced we the non-dimensional time, distance, velocity and pressure which are defined as $t^* = tU/L$, $x^* = x/L$, $\boldsymbol{u}^* = \boldsymbol{u}/U$ and $p^* = p/\rho_0 U^2$, respectively. The Coriolis force is neglected since the main focus of this work is in the lower layers of the ABL.

The Reynolds decomposition decomposes the instantaneous quantities into its time-averaged and fluctuating quantities, i.e. $\boldsymbol{u}^* = \langle \boldsymbol{u}^* \rangle + \boldsymbol{u}'^*$ and $p^* = \langle p^* \rangle + p'^*$ with $\langle \boldsymbol{u}' \rangle = 0$ and $\langle p' \rangle = 0$. By applying the Reynolds decomposition to Eqs. (2.1) and (2.2), and subsequently time-averaging the result, the RANS equations are obtained. Therefore, RANS equations describe the evolution of the mean flow properties. These are further discussed in Section 2.2.

Instead of the Reynolds decomposition, in Large-Eddy Simulations (LES) a filtering operation

$$\phi(\boldsymbol{x}, t) = \int_{-\infty}^{\infty} \int_{-\infty}^{\infty} \phi(\boldsymbol{r}, t') G(\boldsymbol{x} - \boldsymbol{r}, t - t') dt' d\boldsymbol{r}, \tag{2.3}$$

where G is the filter convolution kernel, is applied to the flow fields. By substituting the filtered fields in Eqs. (2.1) and (2.2), all flow scales larger than the filter size specified, which is typically in the order of the grid size, are explicitly resolved while the scales smaller than the filter size need to be modeled using LES turbulence models. Application of LES to the dispersion in the ABL is elaborated in Section 2.3.

2.2 Reynolds-averaged Navier–Stokes

2.2.1 Non-dimensional transport equations

The steady-state RANS equations for mass and momentum conservation for an incompressible fluid are obtained by applying the Reynolds decomposition to Eqs. (2.1) and (2.2) and subsequently time-averaging the result. These are given by

$$\nabla^* \cdot \langle \boldsymbol{u}^* \rangle = 0 \tag{2.4}$$

$$\langle \boldsymbol{u}^* \rangle \cdot \nabla^* \langle \boldsymbol{u}^* \rangle = -\nabla^* \langle p^* \rangle - \nabla \cdot \langle \boldsymbol{u}'^* \boldsymbol{u}'^* \rangle + \frac{1}{Re} \nabla^{*2} \langle \boldsymbol{u}^* \rangle \tag{2.5}$$

where $\langle \boldsymbol{u}'^* \boldsymbol{u}'^* \rangle$ is the mean Reynolds stresses tensor. For the ABL, typically $L \approx 1000$ m, $U \approx 1$ ms^{-1}, and $\nu \approx 1.5 \times 10^{-5}$ m^{2}s^{-1}, hence the Reynolds number is in the order of $Re \approx 10^8$. As a result, the contribution of the viscous term $\nabla^* \langle \boldsymbol{u}^* \rangle / Re$ to the momentum balance is negligible compared to $\langle \boldsymbol{u}'^* \boldsymbol{u}'^* \rangle$. Therefore, we neglect the term for the remainder of this dissertation. Note that very close to a wall, the mean velocity gradient can become significant, in particular at the distance smaller than $y^+ (= u_\tau y / \nu) \approx 20 \ldots 30$. Because of the size of the grid and the modeling of the rough wall, y^+ is at least one order magnitude larger in the current work.

The mean Reynolds stresses tensor is not resolved but usually modeled using an eddy viscosity turbulence model such that (using Einstein summation convention)

$$\langle u_i'^* u_j'^* \rangle = -2\nu_t^* \left(\langle S_{ij}^* \rangle - \frac{1}{3} k^* \delta_{ij} \right) \tag{2.6}$$

where $\langle \boldsymbol{S}^* \rangle = [\nabla^* \langle \boldsymbol{u}^* \rangle + (\nabla^* \langle \boldsymbol{u}^* \rangle)^T]/2$ is the mean strain rate tensor, ν_t^* is the turbulent viscosity, and $k^* \equiv 0.5 \langle u_i^* u_i^* \rangle$ is the turbulent kinetic energy. The isotropic component $(2/3 k^* \delta_{ij})$ is often absorbed into the pressure leading to a modified mean pressure [101].

The k-ε model and its variants are the most widely used models to provide turbulence closure in RANS simulations of near-range atmospheric dispersion problems [64]. We employ the standard k-ε model in which ν_t^* is modeled as

$$\nu_t^* = C_\mu \frac{k^{*2}}{\varepsilon^*}, \tag{2.7}$$

where k and ε follow from solving [131]

$$\nabla^* \cdot \langle \boldsymbol{u}^* \rangle k^* = \nabla^* \cdot \left(\frac{\nu_t^*}{\sigma_k} \nabla^* k^* \right) + P_k^* - \varepsilon^* \tag{2.8}$$

$$\nabla^* \cdot \langle \boldsymbol{u}^* \rangle \varepsilon^* = \nabla^* \cdot \left(\frac{\nu_t^*}{\sigma_\varepsilon} \nabla^* \varepsilon^* \right) + C_{\varepsilon 1} P_k^* \frac{\varepsilon^*}{k^*} - C_{\varepsilon 2} \frac{\varepsilon^{*2}}{k^*} \tag{2.9}$$

with $P_k^* = 2\nu_t^* \langle \boldsymbol{S}^* \rangle : \langle \boldsymbol{S}^* \rangle$, the turbulent production term and with C_μ, $C_{\varepsilon 1}$, $C_{\varepsilon 2}$, σ_k and σ_ε model constants. The default model coefficients are given in Table 2.1.

Table 2.1: $k-\varepsilon$ model constants [64].

	C_μ	$C_{\varepsilon 1}$	$C_{\varepsilon 2}$	σ_k	σ_ε	κ
Default	0.09	1.44	1.92	1.00	1.92	0.40
Modified	0.09	1.44	1.92	1.00	1.11	0.40

Richards and Hoxey [108] demonstrated that, if the model constants are chosen such that

$$\sigma_\varepsilon = \frac{\kappa^2}{C_{\varepsilon 2} - C_{\varepsilon 1}\sqrt{C_\mu}} \tag{2.10}$$

where $\kappa = 0.4$ is the vón Kármán constant, the exact solution of Eqs. (2.4), (2.5), (2.8) and (2.9) is given by

$$(u_x, u_y, u_z) = \left(0, 0, \frac{u_\tau}{\kappa}\ln\left(\frac{z}{z_0}\right)\right) \tag{2.11a}$$

$$k = \frac{u_\tau^2}{\sqrt{C_\mu}} \tag{2.11b}$$

$$\varepsilon = \frac{u_\tau^3}{\kappa z} \tag{2.11c}$$

where $u_\tau = \sqrt{\tau_w/\rho}$ is the friction velocity and z_0 is the aerodynamic roughness length (see, e.g., Ref. [152] for a discussion on the values for z_0). This corresponds to the expected solution for a fully developed, neutrally stratified surface-layer flow, assuming a constant shear stress, zero pressure gradient and horizontal homogeneity. The modified set of model coefficients, meeting the condition set in Eq. (2.10), are also given in Table 2.1. Since we are exclusively modeling neutral ABLs in the current work, the modified set of coefficients is employed in this thesis.

For the dispersion of radioactive and non-buoyant, non-reactive gases, an Eulerian approach is used. The dispersion is modeled using a time-dependent three-dimensional advection-diffusion problem. Neglecting the small effect of molecular diffusion at the scale of the mean concentration gradients, the evolution of the pollutant concentration is described by

$$\frac{\partial c^*}{\partial t^*} + \nabla^* \cdot \left(\langle \boldsymbol{u}^* \rangle c^*\right) = -\nabla^* \cdot \langle \boldsymbol{u}'^* c'^* \rangle - \lambda^* c^* + S_p^* \tag{2.12}$$

where $c^* = cUL^2/R$ is the non-dimensional concentration, $\lambda^* = \lambda L/U$ is the non-dimensional radioactive decay constant, and $S_p^* = SL^3/R$ is the non-

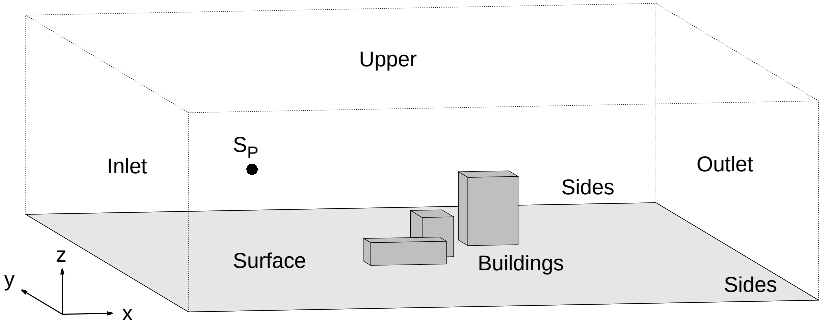

Figure 2.1: Outline of a typical simulation domain.

dimensional pollutant source term. We model the turbulent diffusion $\langle \boldsymbol{u}'^* c'^* \rangle$ with an eddy-diffusivity approach, i.e. [16]:

$$- \langle \boldsymbol{u}'^* c'^* \rangle \approx \frac{\nu_t^*}{Sc_t} \nabla^* c^* \tag{2.13}$$

with Sc_t the turbulent Schmidt number. In the current study we employ $Sc_t = 0.9$ (see, e.g., Ref. [139] for a discussion on values for the turbulent Schmidt number). Note that for small decay constants or for very high wind speeds, λ^* is approximately zero and the pollutant concentration becomes independent from radioactive decay $c^*(\lambda^*, Sc_t) \approx c^*(0, Sc_t)$.

2.2.2 Boundary conditions

An outline of a general simulation domain is given in Fig. 2.1. The coordinate system is always chosen such that the x-axis is in the streamwise direction and that the z-axis is in the vertical direction. Further, the domain dimensions are based on the COST 732 and AIJ guidelines [47, 138]. The boundary conditions are chosen in accordance to Richards and Hoxey [108]. At the inlet, the profiles given in Eqs. (2.11) are imposed, therefore implying that the region upstream is an homogeneous, infinitely large, open field with roughness length z_0. At the outlet, all variables are assumed fully developed in the flow direction, hence a zero gradient is set for all. A constant kinematic shear stress $\tau(z_t) = u_\tau^2$ is applied at the upper boundary and gradient conditions are imposed for k and ε based on the analytical profiles (cf. Eqs. (2.11)b-c)

$$\left.\frac{\partial k}{\partial z}\right|_{z=z_t} = 0, \qquad \left.\frac{\partial \varepsilon}{\partial z}\right|_{z=z_t} = -\frac{u_\tau^3}{k z_t^2} \tag{2.14}$$

where z_t equals the height of the domain. A wall shear stress model is applied to the ground surface and to the buildings. For the velocity a logarithmic velocity profile is enforced in the first grid cell corresponding to the profile of a rough wall for the ground surface and a smooth wall and the buildings, respectively. The wall functions for the turbulent quantities k and ε are given by

$$k_P = \frac{u_\tau^2}{\sqrt{C_\mu}} \tag{2.15}$$

$$\varepsilon_P = \frac{u_\tau^3}{\kappa z_P} \tag{2.16}$$

where u_τ is derived locally from the velocity field, and z_P is the distance of the first grid cell center to the wall. At the sides, the slip condition is set. At the inlet, the concentration is set to zero. At other boundaries, Neumann boundary conditions are applied.

Note that even when considering the simplest case of horizontally homogeneous conditions, discretization errors usually introduce streamwise gradients in the flow. This has been the subject of many studies [19, 64, 94, 131]. Sumner and Masson [131] illustrated that the errors can be fully eliminated using analytically derived correction factors and appropriate discretization schemes. Because the corrections are only valid for the simple case of an open field, however, they are not applied in the current work.

2.3 Large-Eddy Simulation

2.3.1 Non-dimensional transport equations

The incompressible, filtered Navier–Stokes equations are solved in order to obtain the turbulent velocity field $\tilde{\boldsymbol{u}}^*(\boldsymbol{x}, t)$ in the neutral ABL. The viscous term is neglected because viscosity is negligible at the resolved scales of very high Reynolds number flows [1, 21] and no near-ground viscous processes are resolved (as opposed to resolving the viscous sublayer, see, e.g., Ref. [101]). Hence, the continuity and momentum equation read

$$\nabla^* \cdot \tilde{\boldsymbol{u}}^* = 0 \tag{2.17}$$

$$\frac{\partial \tilde{\boldsymbol{u}}^*}{\partial t^*} + \tilde{\boldsymbol{u}}^* \cdot \nabla \tilde{\boldsymbol{u}}^* = -\nabla^* \tilde{p}^* - \nabla^* \cdot \boldsymbol{\tau}^* \tag{2.18}$$

where the non-dimensional variables $\tilde{\boldsymbol{u}}^*(\boldsymbol{x}, t)$ is the resolved velocity field, $\tilde{p}^*$ is the non-dimensional pressure and $\boldsymbol{\tau}^*$ is the non-dimensional SGS stress tensor which is defined by $\tau_{ij} = \widetilde{u_i u_j} - \tilde{u}_i \tilde{u}_j$. The Smagorinsky model is applied to model the deviatoric part of this stress tensor, such that (using Einstein summation convention)

$$\tau^*_{ij} - \frac{1}{3}\delta_{ij}\tau^*_{kk} \cong -2\nu^*_{sgs}\tilde{S}^*_{ij} = -2(c_{s,\Delta}\Delta^*)^2|\tilde{S}^*_{ij}|\tilde{S}^*_{ij} \tag{2.19}$$

where $\tilde{\boldsymbol{S}}^* = [\nabla^*\tilde{\boldsymbol{u}}^* + (\nabla^*\tilde{\boldsymbol{u}}^*)^T]/2$ is the resolved strain-rate tensor, $|\tilde{S}^*_{ij}| = (2\tilde{S}^*_{ij}\tilde{S}^*_{ij})^{1/2}$, $\nu^*_{sgs} = \nu_{sgs}/UL^2$ is the non-dimensional SGS eddy viscosity, and $\Delta^* = \Delta/L$ is the LES filter width. The trace of the Subgrid scale (SGS) stress tensor, $\tau_{kk}/3$, is not explicitly modeled, but instead absorbed into the pressure as is common practice in LES of incompressible flow.

The Lagrangian scale-dependent dynamic Smagorinsky model is employed to obtain a space and time dependent estimation of $c_{s,\Delta}$ [21]. This model is well-suited for the study of pollutant dispersion in the ABL as illustrated, among others, with studies on pollen transport in the ABL [28], on particle dispersion inside the canopy roughness sublayer [95], and on the pollutant dispersion in an urban environment [144]. The SGS turbulence model requires the solution of four additional transport equations [21]

$$\frac{\partial J_{LM}}{\partial t^*} + \nabla^* \cdot (\tilde{\boldsymbol{u}}^* J_{LM}) = \frac{1}{T_{2\Delta}}(L_{ij}M_{ij} - J_{LM}) \tag{2.20a}$$

$$\frac{\partial J_{MM}}{\partial t^*} + \nabla^* \cdot (\tilde{\boldsymbol{u}}^* J_{MM}) = \frac{1}{T_{2\Delta}}(M_{ij}M_{ij} - J_{MM}) \tag{2.20b}$$

$$\frac{\partial J_{QN}}{\partial t^*} + \nabla^* \cdot (\tilde{\boldsymbol{u}}^* J_{QN}) = \frac{1}{T_{4\Delta}}(Q_{ij}N_{ij} - J_{QN}) \tag{2.20c}$$

$$\frac{\partial J_{NN}}{\partial t^*} + \nabla^* \cdot (\tilde{\boldsymbol{u}}^* J_{NN}) = \frac{1}{T_{4\Delta}}(N_{ij}N_{ij} - J_{NN}) \tag{2.20d}$$

where $T_{2\Delta} = 1.5\Delta(J_{LM}J_{MM})^{-1/8}$, and $T_{4\Delta} = 1.5\Delta(J_{QN}J_{NN})^{-1/8}$ are time constants, and where variables L_{ij}, Q_{ij}, M_{ij} and N_{ij} are computed using their definitions

$$L_{ij} = \widehat{\tilde{u}^*_i\tilde{u}^*_j} - \hat{\tilde{u}}^*_i\hat{\tilde{u}}^*_j \tag{2.21a}$$

$$Q_{ij} = \overline{\tilde{u}^*_i\tilde{u}^*_j} - \bar{\tilde{u}}^*_i\bar{\tilde{u}}^*_j \tag{2.21b}$$

$$M_{ij} = 2\Delta^{*2}\left(\widehat{|\tilde{S}^*|\tilde{S}^*_{ij}} - \alpha^2\beta|\hat{\tilde{S}}^*|\hat{\tilde{S}}^*_{ij}\right) \tag{2.21c}$$

$$N_{ij} = 2\Delta^{*2}\left(\overline{|\tilde{S}^*|\tilde{S}^*_{ij}} - \alpha^4\beta^2|\bar{\tilde{S}}^*|\bar{\tilde{S}}^*_{ij}\right) \tag{2.21d}$$

Here, a tilde $(\tilde{\bullet})$, a caret $(\hat{\bullet})$, and a bar $(\overline{\bullet})$ represent a quantity filtered at grid scale (Δ), at test-filter scale $(\alpha\Delta)$, and at a second test-filter scale $(\alpha^2\Delta)$, respectively. Typically, $\alpha = 2$ and $\beta = 1$ [21]. Finally, the Smagorinsky coefficient is determined as

$$c_{s,\Delta}^2 = \frac{J_{LM}/J_{MM}}{\max\left(\frac{J_{QN}J_{MM}}{J_{NN}J_{LM}}, 0.125\right)} \tag{2.22}$$

where the clipping limit of 0.125 is added for stability.

The resolved flow field serves as an input to describe the dispersion of radioactive, non-buoyant, and non-reactive gases in the neutral ABL. The time-dependent three-dimensional advection-diffusion equation is employed to model the evolution of the non-dimensional concentration

$$\frac{\partial \tilde{c}^*}{\partial t^*} + \nabla^* \cdot \left(\tilde{\boldsymbol{u}}^*\, \tilde{c}^*\right) = \nabla^* \cdot \left(\tilde{\boldsymbol{u}}^* \tilde{c}^* - \widetilde{\boldsymbol{u}^* c^*}\right) - \lambda^* \tilde{c}^* + S^* \tag{2.23}$$

where $\tilde{c}^* = \tilde{c}UL^2/R$ is the non-dimensional concentration, and $\tilde{\boldsymbol{u}}^* \tilde{c}^* - \widetilde{\boldsymbol{u}^* c^*}$ is the sub-grid scale pollutant flux. In order to model the sub-grid scale pollutant flux, an eddy-diffusivity approach is used, i.e. [16]:

$$\tilde{\boldsymbol{u}}^* \tilde{c}^* - \widetilde{\boldsymbol{u}^* c^*} \approx \frac{\nu_{sgs}^*}{Sc_{sgs}} \nabla^* \tilde{c}^* \tag{2.24}$$

where Sc_{sgs} is the SGS Schmidt number. In the current study $Sc_{sgs} = 0.4$ is employed (adopted from Ref. [28]). A detailed discussion on the boundary conditions is included in Chapter 4.

2.4 Dose assessment

A dose from a radioactive cloud can be received through multiple pathways. Each pathway can result in either an external dose or an internal dose, depending whether the sources remain outside or move inside the body, respectively [136]. In case of the release of a radioactive cloud, the dominant pathways during the early stage of the nuclear accident are the external dose from cloud shine and the internal dose from inhalation. Further, we focus the discussion on beta and gamma radiation because these are directly measurable. Alpha radiation is not considered explicitly. However, we note that the dose assessment for alpha radiation is similar to that of beta radiation. Regardless the type of radiation, the dispersion of the gas is not affected by the radioactive decay. As a result, the dose models are fully decoupled from the transport models. As such, they can be applied as a post-processing step. First, the evaluation of the radiological dose from beta radiation is discussed in §2.4.1. Next, in §2.4.2, the assessment of the radiological dose from gamma radiation is presented.

2.4.1 Beta dose rate

The exposure to beta radiation from a radioactive plume emitting beta particles (which are electrons or sometimes positrons) can result in both an external and an internal dose. The external dose primarily originates from beta particles penetrating a few millimeters into the skin. Because of the limited travel distance of beta particles in air, in the range of 1 to 10 m [36, 127], beta particles at a larger distance do not contribute to the dose received. Therefore, as a first estimate, the skin dose rate at a location $\boldsymbol{x}_0$ can be computed by treating the plume as an infinite cloud with a concentration equal to the local concentration. This allows the beta dose rate in air to be computed as [127]:

$$\dot{d}_{\beta,\boldsymbol{x}_0} = K_\beta \bar{E}_\beta \lambda^* c^*(\boldsymbol{x}_0) \frac{R}{L^3} \tag{2.25}$$

with K_β a conversion factor accounting for the properties of air, $\bar{E}_\beta$ the average beta energy per disintegration, and $c(\boldsymbol{x}_0)$ the concentration at location $\boldsymbol{x}_0$. In order to account for the very limited range of beta particles in tissue, the skin dose rate is often corrected to only one-half of $\dot{d}_{\beta,\boldsymbol{x}_0}$. An additional correction factor can be applied to account for the fact that the dose rate at ground level is only one-half of the dose rate in an infinite cloud. Therefore, the correction factor increases from 0.5 at ground level to 1.0 an elevation equal to the maximum range of the beta particles involved [127].

The internal dose results from the inhalation of the radioactive gases. This leads to the irradiation of the lungs and, after uptake of the radionuclides by the body, the irradiation other organs. Unfortunately, describing the uptake and transport of radionuclides within the body, and the calculation of the resulting dose requires the use of complicated biological models (see, e.g., Ref. [136]). But it is clear that the amount of radioactive pollutant inhaled is directly proportional to the local concentration $c(\boldsymbol{x}_0)$. We therefore report on the local concentration when quantifying the dose from inhalation in this thesis.

2.4.2 Gamma dose rate

Gamma radiation can travel a considerable distance in air and has a large penetrating power. As a result, an external dose is received not only inside a radioactive plume, but also at locations at a distance from the plume. In addition, inhalation of contaminated air emitting gamma radiation contributes to the internal dose received. The latter, however, is of lesser concern compared to the inhalation dose from beta radiation. Therefore, for gamma radiation, we focus on quantification of the external dose.

It is well established that the gamma fluence rate observed by a receptor located at $\boldsymbol{x}_0 = (x_0, y_0, z_0)$ due to the decay of radioactive matter at location (x', y', z') can be computed using the point-kernel method with buildup factor [127]. To obtain the non-dimensional fluence rate $\phi^* = \phi L^2/R$ at location $\boldsymbol{x}_0$ due to the whole plume, this approach is applied to the continuous concentration field by integrating over the full domain (see, e.g., Ref. [97]):

$$\phi^*_{\boldsymbol{x}_0} = \frac{\lambda^*}{4\pi L} \int\int\int_V \frac{B(\mu, r)}{r^2} e^{-\mu r} c^* dx' dy' dz' \tag{2.26}$$

where $r^2 = (x_0 - x')^2 + (y_0 - y')^2 + (z_0 - z')^2$, V is the domain volume, μ is the linear attenuation coefficient in air and B is the dose buildup factor. Conversion of the local, non-dimensional fluence rate into the local dose rate can subsequently be achieved as

$$\dot{d}_{\gamma,\boldsymbol{x}_0} = \frac{K E_\gamma \mu_{en}}{\rho} \phi^*_{\boldsymbol{x}_0} \frac{R}{L^2} \tag{2.27}$$

with $K = 1.6 \times 10^{-13}\,\mathrm{Gy\ kg\ MeV^{-1}}$ a unit conversion factor, E_γ the gamma energy released per disintegration, μ_{en} the energy absorption coefficient and ρ the density of the receptor. The buildup factor acts as a correction factor to include, e.g., secondary radiation due to Compton scattering in addition to the unscattered primary radiation [5]. Different expressions are found in the literature to evaluate the buildup factor (see, e.g., Ref. [32, 143]). In this work, the parametrization in Taylor form is employed

$$B(\mu, r) = A e^{-\alpha_1 \mu r} + (1 - A) e^{-\alpha_2 \mu r} \tag{2.28}$$

where α_1, α_2 and A are tabled parameters, depending upon E_γ [5].

2.5 OpenFOAM

All simulations presented in this dissertation are performed using OpenFOAM (Open source Field Operation And Manipulation), a finite-volume simulation platform written in C++. This open source toolbox enables to perform CFD analyses using a range of preimplemented features but also offers the full freedom to customize and extend the code. The latter renders it particularly useful for research purposes.

In order to perform a dose assessment using RANS turbulence modeling, first the mean velocity field and turbulent viscosity are computed by solving the steady-state RANS equations for mass and momentum. Next, the advection diffusion equation for the pollutant dispersion is solved and the dose assessment is performed. Depending on whether time-dependent pollutant dispersion is considered or not, the latter two steps are performed simultaneously or sequentially, respectively. The simulation of the velocity field is performed using the time-dependent `pisoFoam` solver to make use of false time-stepping. A wide range of RANS models are provided by the code, including the $k-\varepsilon$ model used in this work. The customization of the model constants (cf. Table 2.1) can simply be done through modification of the corresponding input file. A default set of boundary conditions for atmospheric boundary layer simulations is also available. However, because the implementation is not fully consistent with the work of Richards and Hoxey [108], a reimplementation was performed. In addition, small modifications were required to adapt the default advection diffusion equation solver to the current needs.

Performing a time-dependent simulation using LES turbulence modeling requires the evaluation of the incompressible, filtered Navier–Stokes equations, the advection diffusion equation describing the pollutant transport and the dose evaluation at every time step. To this end, a series of extensions were made to the code. First, starting from `projectionFoam`, the implementation of an incremental projection scheme solver developed by Onder and Meyers [93], a new solver was developed solving the incompressible, filtered Navier–Stokes equations simultaneous with the scalar transport equation and the dose assessment. Second, the Lagrangian scale-dependent dynamic Smagorinsky model was implemented by extending the `dynLagrangian` turbulence model by adding a second `LESfilter` and the corresponding transport equations. This effort additionally lead to the detection and reporting of three bugs which were accommodated for in new OpenFOAM releases[1]. Third, a number of code optimizations were introduced and automated post processing tools were developed in order to shorten the simulation time.

Finally, radiological dose rate models are not included in the standard OpenFOAM installation. Therefore, a new class structure was set up which allows for the dose assessment from beta and gamma radiation using the models described in Section 2.4. In order to evaluate the buildup factor Eq. (2.28), sixth order polynomial fits in $\ln E_\gamma$ are constructed to compute α_1 and α_2

---

[1] For further details, see OpenFOAM Mantis Bug Tracker (www.openfoam.org/bugs/):

- Bug ID 0000706, submitted on December 18, 2012.
- Bug ID 0000794, submitted on March 20, 2013.
- Bug ID 0000816, submitted on April 15, 2013.

from the tabled values, while linear interpolation is used to compute A. The radiological data required is imported from external data files provided by Be *et al.* [13, 14]. Furthermore, decay schemes are automatically reconstructed and unstable daughter isotopes are automatically included in the simulation.

Chapter 3

Accounting for wind-direction fluctuations

In RANS simulation of atmospheric dispersion a large discrepancy in lateral spread between simulations and experimental data is often observed, combined with a significant overestimation of the concentrations in a vertical plane through the point of release and parallel with the wind direction. In an attempt to correct this, Quinn *et al.* [104], and Tang *et al.* [132] weighted a set of steady-state RANS solution over the distribution of wind directions, changing their single-wind CFD model to a time-averaged variable-wind CFD model. This weighting approach is also applied by Huber *et al.* [67] who notes that accounting for the full wind variability overpredicts the lateral spreading of pollutants; hence, measurements lie in between the single-wind, and the variable-wind solution.

In this chapter, we argue that fluctuations in wind directions observed in experiments are already partly accounted for by the modeled turbulence in dispersion simulations; and hence, the effective variability that should be

---

The material in this chapter is composed from

"Lieven Vervecken, Johan Camps, and Johan Meyers. Accounting for wind-direction fluctuations in Reynolds-averaged simulation of near-range atmospheric dispersion. *Atmospheric Environment*, 72:142–150, 2013.", and

"Lieven Vervecken, Johan Camps, and Johan Meyers. Effect of wind fluctuations on near-range atmospheric dispersion under different types of thermal stratification. In *Proceedings of the 15th International Conference on Harmonisation within Atmospheric Dispersion Modelling for Regulatory Purposes*, pages 772–777. 2013".

used as a boundary condition to the simulations, needs to be lower than experimentally measured. Variability in wind that is observed on time scales of seconds to say quarter of an hour, as monitored in conventional ten-minute statistics, are in part due to three-dimensional turbulence in the atmospheric boundary layer, characterized by scales that are proportional to the boundary layer depth, while another part of the variability can be attributed to dynamics on larger scales, e.g., related to the existence of internal gravity waves, temperature effects in the troposphere, etc. (cf., e.g., Ref. [145]). In dispersion simulations, with typical domain sizes of kilometer scale, the effect of three-dimensional turbulence is included in the simulation model (i.e. in the turbulence model for RANS). Dynamics of larger scales are not included and need to be accounted for in the boundary conditions.

Therefore, we present a simple approach to estimate from experiments the correct level of variability in wind direction that is required as a boundary condition for dispersion simulations. We demonstrate the approach based on simulations of, and comparison to a selection of the well-known Project Prairie Grass experiments [10]. Since the geometry of the Prairie Grass experiment is very simple (i.e. flat terrain without any obstacles), it is possible to reformulate the RANS equations into a dispersion-simulation model that is based on prescribed analytical profiles for velocity and eddy viscosity as function of height. We use these to solve a three-dimensional advection-diffusion problem in which turbulent pollutant dispersion is modeled based on an eddy-diffusivity approach. For more complex geometries (e.g. buildings, canopy, ...), this approach cannot be followed since the analytical profiles for velocity and eddy viscosity are generally not known. Instead, the full flow equations have to be solved in combination with the estimated level of variability before the advection-diffusion problem can be solved.

This chapter is further organized as follows. First, in Section 3.1, we present a simple approach to estimate the correct level of wind-direction variability required in dispersion simulations, and the dispersion model used for the simulation of the Project Prairie Grass experiments. Subsequently, in Section 3.2 we detail the experiments that are considered in the current work, the numerical set-up of our simulations, and also briefly discuss a set of criteria to compare simulations to experiments. Simulation results are discussed in Section 3.3. Finally, conclusions are presented in Section 3.4.

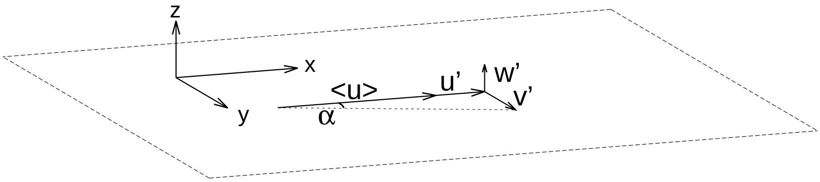

Figure 3.1: Diagram of the wind vector.

3.1 Methodology

In the current section we introduce in §3.1.1 a simple approach to estimate the correct level of wind-direction variability required in dispersion simulations. Next, the dispersion model used for the simulation of the Project Prairie Grass experiments with neutral atmospheric conditions is briefly presented in §3.1.2. In §3.1.3, the dispersion model is extended to account for thermal stratification.

3.1.1 Variability of wind direction

Consider a variable wind vector $\boldsymbol{u} = (u, v, w)$, e.g., observed at a meteorological tower. We denote the time-averaged velocity with $\langle \boldsymbol{u} \rangle = (\langle u \rangle, \langle v \rangle, \langle w \rangle)$, and select the coordinate system such that $\langle v \rangle = \langle w \rangle = 0$, i.e., the x-direction is aligned with the mean-flow direction; further, the z-direction is normal to the ground (cf. Fig. 3.1). Hence, in the horizontal x–y plane, the velocity vector can be decomposed as $u = \langle u \rangle + u'$, and $v = v'$, with u', v' the fluctuating x and y components of the velocity field. The instantaneous wind direction (measured in the horizontal x–y plane) is then characterized by the angle

$$\alpha = \arctan\left(\frac{v'}{\langle u \rangle + u'}\right). \tag{3.1}$$

We now presume that the fluctuating velocity components can be split into two contributions, i.e., a contribution $\boldsymbol{u}'_m$ that can be internally represented in a CFD model (related to conventional three-dimensional boundary-layer turbulence), and a large-scale part $\boldsymbol{u}'_e$ that is not internally represented in the computational model used for near-range dispersion simulations, and is formally defined as $\boldsymbol{u}'_e = \boldsymbol{u}' - \boldsymbol{u}'_m$. This second part needs to be incorporated as an external boundary condition (hence the subscript 'e'). Consequently,

$$u = \langle u \rangle + u'_m + u'_e, \tag{3.2}$$

$$v = v'_m + v'_e. \tag{3.3}$$

If we now presume that $v \ll u$ (such that also $\tan\alpha \ll 1$), and $u' \ll u$, we can approximate the instantaneous angle (Eq. 3.1) with

$$\alpha = \frac{v'_m + v'_e}{\langle u \rangle} \tag{3.4}$$

In practice, this is a reasonable approximation. Under thermally neutral atmospheric conditions, the variation σ_α is usually in the range 7.5° to 12.5° for 15 minute averages [160]. For stable stratification, smaller variations of 2.5° to 7.5° are found, while for unstable stratification the range typically corresponds to 12.5° to 22.5° [160].

Now, taking the mean square of both sides of Eq. (3.4) yields

$$\langle \alpha^2 \rangle = \frac{\langle v'^2_m \rangle + 2\langle v'_m v'_e \rangle + \langle v'^2_e \rangle}{\langle u \rangle^2} \tag{3.5}$$

where $\langle \alpha^2 \rangle$ is by definition equal to the total variance σ^2_α of the wind direction (since by construction, $\langle \alpha \rangle = 0$). Unfortunately, to our knowledge, the covariance $\langle v'_m v'_e \rangle$ is not easy to estimate or model, and we use the rough approximation $\langle v'_m v'_e \rangle \approx 0$. Thus, the total variance of the wind direction is approximated as

$$\sigma^2_\alpha \approx \frac{\langle v'^2_e \rangle}{\langle u \rangle^2} + \frac{\langle v'^2_m \rangle}{\langle u \rangle^2} = \sigma^2_e + \sigma^2_m, \tag{3.6}$$

where σ^2_m is that part of the variance that is internally accounted for in the CFD model, and σ^2_e needs to be accounted for in the boundary conditions.

We will simply estimate σ^2_m based on a single simulation in which we evaluate the turbulent characteristics at the level of the experimental measurement of variable wind direction. Next, we weight the solution assuming a normal distribution for the wind direction characterized by a zero mean and the reduced variance $\sigma^2_e = \sigma^2_\alpha - \sigma^2_m$ (and where σ^2_α is obtained from the experiments).

3.1.2 Neutral boundary layer dispersion model

The geometry of the Prairie Grass experiments set-up is very simple, i.e. the experiments were performed on a wide open prairie in Nebraska, without any obstructions from buildings or vegetation (cf. also Fig. 3.2). For this type of simple geometry and neutral stability, the Reynolds-averaged velocity profile is known to follow a logarithmic distribution [101]. This allows us to much simplify the RANS equations into an advection-diffusion problem for the pollutants.

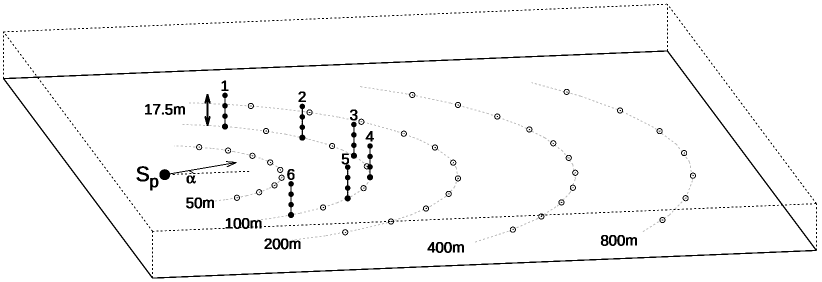

Figure 3.2: Outline of the Prairie Grass open-field experiment, and definition of angle α_m between mean-wind direction and the symmetry line passing between tower 3 and 4.

Thus, we simulate the experiments using a simple advection-diffusion equation, where we presume a conventional logarithmic mean velocity profile (cf., e.g., Ref. [101]) that is given by

$$\langle u \rangle = \frac{u_\tau}{\kappa} \ln \left(\frac{z}{z_0} \right), \tag{3.7}$$

with κ the von Kármán constant, z_0 the roughness length, and with $u_\tau \equiv \sqrt{\tau_w/\rho}$, where τ_w is the wall shear stress. Values for z_0 and u_τ are obtained by fitting this profile to the experimental data (cf. Section 3.2). Given this boundary-layer velocity field, the Reynolds-averaged advection-diffusion equation (cf. Eq. 2.12) is solved for the stationary solution.

For the eddy-viscosity, required in Eq. (2.13), a simple analytical expression is obtained from boundary-layer theory under neutral conditions. First of all, we presume that the computational domain is sufficiently shallow so that Coriolis forces do not play a dominant role, and can be neglected. In that case, the flow is solely driven by a pressure gradient, that follows from the geostrophic balance above the boundary layer (see, e.g., Ref. [133]). The x-momentum balance then corresponds to (cf., e.g., Ref. [101])

$$\frac{\mathrm{d}\langle p \rangle}{\mathrm{d}x} = \frac{\mathrm{d}\tau}{\mathrm{d}z}, \tag{3.8}$$

where the total shear stress τ defined as

$$\tau = \rho\nu \frac{\mathrm{d}\langle u \rangle}{\mathrm{d}z} - \rho \langle u'w' \rangle \approx \rho(\nu + \nu_t) \frac{\mathrm{d}\langle u \rangle}{\mathrm{d}z}, \tag{3.9}$$

with ν the kinematic viscosity of air, and ν_t the eddy viscosity. Since $\mathrm{d}\langle p \rangle / \mathrm{d}x$ is not a function of z, the same holds for $\mathrm{d}\tau/\mathrm{d}z$. Further, the Reynolds number in atmospheric boundary layer flows is very high so that $\nu \ll \nu_t$. Hence, we can integrate both sides of Eq. (3.8) from 0 to the height z, and obtain

$$\frac{\mathrm{d}\langle p\rangle}{\mathrm{d}x} z = \rho \nu_t \frac{\mathrm{d}\langle u\rangle}{\mathrm{d}z} - \tau_w, \tag{3.10}$$

with τ_w the shear stress at the wall. Finally, the pressure gradient in the atmospheric boundary layer is determined by the geostrophic balance above the boundary layer, but can be related to the wall shear using $\mathrm{d}\langle p\rangle/\mathrm{d}x = -\tau_w/\delta$, where $\delta = Au_\tau/f$ (with f the Coriolis parameter, and $A \approx 12$ an empirical constant – cf., e.g., Ref. [133], for an overview). Based on this, and using Eq. (3.7), Eq. (3.10) is reformulated into

$$\nu_t = u_\tau \kappa z \left(1 - \frac{z}{\delta}\right). \tag{3.11}$$

This equation is straightforwardly combined with Eq. (2.13), to model the turbulent diffusion in Eq. (2.12).

Note that solving Eq. (2.12) in combination with Eqs. (2.13), (3.7), and (3.11) is different from solving the full Reynolds-averaged Navier–Stokes equations. However, when these latter equations are appropriately discretized, and the turbulence models are well tuned, the effective velocity profile and turbulent viscosity profiles that are obtained in RANS simulations will effectively correspond to Eqs. (3.7), and (3.11) (see, e.g., Ref. [64], or Ref. [131]). Therefore, conclusions with respect to different approaches to incorporate wind-variability based on the Reynolds-averaged advection–diffusion model that we use in the current study, are also relevant to RANS simulations.

3.1.3 Thermally stratified boundary layer dispersion model

In order to account for thermal stratification, we simply presume a logarithmic mean velocity profile that is extended to a thermally stratified boundary layer by the Monin-Obukhov similarity theory [88]. Accordingly we can write [99]

$$\frac{\mathrm{d}\langle u\rangle}{\mathrm{d}z} = \frac{u_\tau}{\kappa z}\phi_M \tag{3.12}$$

with ϕ_M a stability function. Several analytical expressions for ϕ_M have been suggested [25, 41, 45], but among the more frequently used, are the following [130]

$$\phi_M = \begin{cases} (1 - \gamma_1 \zeta)^{-0.25}, & -2 < \zeta < 0 \text{ (unstable)} \\ 1 + \beta\zeta, & 0 \leq 1 \text{ (stable)} \end{cases} \tag{3.13}$$

where γ_1 and β are model constants and where $\zeta \equiv z/L$ with L the Monin-Obukhov length. In the current work, we assume $\gamma_1 = 16$ and $\beta = 5$ (see, Ref. [51] for a discussion).

Integration of Eq. (3.12) leads to the mean velocity profile (cf., e.g., Ref. [130])

$$\langle u \rangle = \frac{u_\tau}{\kappa} \left[\ln\left(\frac{z}{z_0}\right) - \Psi_M(\zeta) \right] \tag{3.14}$$

with, if $x = (1 - \gamma_1 \zeta)^{0.25}$,

$$\Psi_M = \begin{cases} \ln\left[\left(\frac{1+x^2}{2}\right)\left(\frac{1+x}{2}\right)^2\right] - 2\tan^{-1} x + \pi/2, & -2 < \zeta < 0 \text{ (unstable)} \\ -\beta\zeta, & 0 \leq 1 \text{ (stable).} \end{cases} \tag{3.15}$$

Values for z_0, u_τ and L are again obtained from a least-squares fit of the velocity profiles to experimental data, together with similar fits for the potential temperature [23].

Because thermal stratification does not influence the x-momentum balance, the development in §3.1.2 can be repeated, substituting Eq. (3.14) for the velocity gradient, to obtain an analytical expression for the eddy-viscosity

$$\nu_t = \frac{u_\tau \kappa z (1 - z)/\delta}{\phi_m}. \tag{3.16}$$

Therefore, by using Eqs. (3.14), (3.16) and (2.13) in Eq. (2.12), a solution for the dispersion over an open field in a thermally stratified boundary layer can be found without the need for solving the full RANS equations.

3.2 Project Prairie Grass experiments, and computational set-up

In the current section we briefly discuss the Project Prairie Grass experiments that are used as point of comparison for our simulations in §3.2.1. The computational set-up used to solve the convection diffusion problem is presented in §3.2.2. Finally, in §3.2.3, we review the performance criteria proposed by Chang and Hanna [30], that we will use later on as one of the tools to compare the quality of simulation approaches to the experimental data.

Table 3.1: Overview of measured wind direction, wind variability, release rate, and calculated power law exponent, roughness length and friction velocity for the 15 selected Prairie Grass experiments with neutral stratification.

Experiment	α (°)	σ_α (°)	R (g/s)	power law exponent	z_0 (m)	u_τ (m/s)
5	160	11.1	77.8	0.180	0.00450	0.381
6	180	7.7	89.5	0.187	0.00589	0.469
9	199	9.5	92.0	0.163	0.00336	0.428
11	185	6.9	95.9	0.187	0.00583	0.522
12	175	9.9	99.1	0.178	0.00431	0.521
20	168	8.3	101.2	0.166	0.00378	0.587
33	171	9.2	94.7	0.184	0.00720	0.546
34	140	7.5	97.4	0.172	0.00447	0.604
42	199	6.6	56.4	0.185	0.00752	0.285
45	153	8.2	100.8	0.173	0.00484	0.394
46	134	7.6	99.7	0.184	0.00758	0.405
48	189	8.1	104.1	0.168	0.00424	0.505
49	185	11.1	102.0	0.159	0.00292	0.408
57	185	8.2	101.5	0.175	0.00550	0.492
61	190	10.9	102.1	0.149	0.00196	0.443

3.2.1 Project Prairie Grass

Project Prairie Grass was a field program comprising 68 experiments conducted on flat prairie in Nebraska in the summer of 1956 [10]. The experimental set-up is shown schematically in Fig. 3.2. The program was conducted during July and August of 1956 with an equal number of experiments during the daytime and nighttime. Each time, the non-reactive, non-buoyant gas sulfur dioxide was released at a constant release rate. The time-averaged concentration was registered with 10-minute samples downwind from a source release (S_p) along five arcs (○) and six towers (●). The arcs are located at 50, 100, 200, 400 and 800 meters from the source and the towers are positioned along the arc at 100 meter, spaced at 14 degrees intervals. The source was placed 0.46 m above ground and can be treated as a point source. The concentration was measured at 1.5 m above ground on the arcs and at nine different heights up to 17.5 m on the towers. The measurement uncertainty was estimated as 10%. In addition to the concentration measurements, the micro-meteorological conditions including wind, temperature and humidity profiles were registered as well.

All experiments are included in the analysis except for those with insufficient

Table 3.2: Overview of measured wind direction, wind variability, release rate, and calculated Monin-Obukhov length, roughness length and friction velocity for the 6 selected Prairie Grass experiments with unstable stratification.

Experiment	α (°)	σ_α (°)	R (g/s)	L (m)	z_0 (m)	u_τ (m/s)
8	365	16.3	91.1	-2.74×10^1	0.01131	0.370
29	37	12.7	41.5	4.70×10^1	0.00649	0.262
43	350	13.7	98.9	-1.65×10^1	0.00621	0.381
44	338	13.7	100.7	-2.82×10^1	0.00663	0.442
51	64	12.6	102.4	-3.51×10^1	0.00401	0.458
52	309	16.5	104.0	-7.97	0.00470	0.322

data, with a wind speed lower than 2 ms^{-1} at 2 m altitude, or with $\sigma_\alpha > 17.5$. The latter two exclude experiments with possibly significant vertical stratification in the plume, which is not taken into account by the model, and experiments under very unstable atmospheric stratification which results in a too strong dilution of the concentration for reliable measurements, respectively. Following Touma [142], the experiments with neutral stability are identified by having a least-squares fit of a power law profile that results in an exponent between 0.12 and 0.19. Next, using the meteorological data listed for the neutral experiments, the friction velocity and the site roughness in Eq. (3.7) are determined by a least-squares fit of a logarithmic velocity profile to each of the experimental wind profiles. Experiments with a velocity profile correlating less than 98.5% with such a logarithmic velocity profile or with missing data were further disqualified. In this way 15 experiments were selected in total, i.e., experiments with numbers 5, 6, 9, 11, 12, 20, 33, 34, 42, 45, 46, 48, 49, 57, and 61 in [10]. In total, these 15 experiments provide 1981 concentration measurements. Further details on the experiments with neutral stability can be found in Table 3.1. Identification of the experiments with stable or unstable stability class is based on σ_α [160] instead of the power law exponent. By changing the criterion, the identification was more consistent with other commonly used stability criteria (see, e.g., Ref [87] for a discussion on stability criteria). This results in the selection of 24 experiments providing 1841 measurements, and 6 experiments providing 1066 measurements, for stable and unstable conditions respectively covering combinations of different field positions, and wind condition. Details on these experiments can be found in Table 3.2 and Table 3.3. Note that the atmospheric conditions during experiments 11 and 42 can be considered either neutral or stable depending on the criteria used.

Table 3.3: Overview of measured wind direction, wind variability, release rate, and calculated Monin-Obukhov length, roughness length and friction velocity for the 24 selected Prairie Grass experiments with stable stratification.

Experiment	α (°)	σ_α (°)	R (g/s)	L (m)	z_0 (m)	u_τ (m/s)
11	5	6.9	95.9	-8.43×10^1	0.00799	0.565
17	357	5.5	56.5	8.36×10^1	0.01498	0.275
18	3	5.7	57.6	3.73×10^1	0.01810	0.271
21	355	6.2	50.9	2.58×10^2	0.00731	0.430
22	352	5.6	48.4	3.30×10^2	0.00810	0.530
23	307	7.2	40.9	3.22×10^2	0.00784	0.443
24	321	6.4	41.2	4.20×10^2	0.00805	0.435
28	352	6.0	41.7	3.75×10^1	0.01886	0.219
32	352	5.2	41.4	1.21×10^1	0.03701	0.187
37	4	6.8	40.3	1.69×10^2	0.01362	0.373
38	349	5.6	45.4	1.68×10^2	0.01639	0.363
41	16	5.0	39.9	4.88×10^1	0.01374	0.296
42	29	6.6	56.4	1.53×10^2	0.00487	0.390
53	309	3.6	45.2	1.66×10^1	0.08198	0.248
54	317	5.7	43.4	5.32×10^1	0.00818	0.282
55	334	6.1	45.3	1.70×10^2	0.00622	0.406
58	361	4.1	40.5	1.92×10^1	0.06974	0.244
59	354	4.6	40.2	2.08×10^1	0.03420	0.243
60	17	5.5	38.5	7.48×10^1	0.00682	0.320
65	352	5.4	44.1	7.76×10^1	0.01322	0.364
66	345	6.4	43.1	3.63×10^1	0.02810	0.294
67	6	6.6	45.0	1.31×10^2	0.01578	0.379
68	354	6.2	42.8	3.58×10^1	0.02461	0.243
70	318	6.4	41.8	7.63×10^1	0.01089	0.292

3.2.2 Computational set-up

We solve the advection–diffusion problem (2.12) using the OpenFOAM finite-volume open-source simulation platform. For the computational domain, we position the inlet boundary 250 meter upstream of the source, and the outlet boundary 1 250 meter downwind from the source. Furthermore, the domain extends 200 meter in each crosswind direction as seen from the source, and the height of the domain is set to 500 meter. At the inlet, concentration is set to zero, at other boundaries Neumann boundary conditions are applied. The advection–diffusion equation is discretized on a Cartesian structured mesh consisting of 1 824 000 hexahedra, and employing second-order central schemes. The centers of the near-wall cells are positioned at a non-dimensional wall distance of $z^+ (= z_P u_\tau/\nu) \approx 17 \times 10^3$. The point source is modeled by simply adding a source term to the corresponding cell in the domain. The grid is refined towards the source cell that has a size of 2.1m x 2.3m x 1.0m. We performed a grid refinement study to verify that this cell size is sufficiently small, yielding a solution at the locations of the measurement arcs and towers that is grid independent. This grid independence is confirmed using the Grid Convergence Index (GCI) [110] which results in a GCI of 0.104%. The simulations are assumed to be fully convergenced after the residuals have dropped below 10^{-16}.

For the construction of a solution that is weighted over the different wind directions observed in the experiment, we presume for simplicity that large-scale external fluctuations and the turbulence represented in the RANS turbulence model are not coupled, so that we can construct an average of concentrations over wind directions based on a set of steady-state RANS solutions obtained for different wind angles (cf., e.g., Ref. [104] where a similar approach is used). In the current case, such an approach is very simple. Since the terrain is flat, it is appreciated that the concentration solution expressed in a reference frame that is aligned with the wind direction, and with origin at the source S_p, is invariant to the wind direction. Hence, to obtain the RANS concentration solution at the measurement points, we can simply rotate the numerical solution around the vertical axis through the source, while maintaining the sensor locations. Thus, a series of angles is taken over the range of $[-4\sigma_e; 4\sigma_e]$, and presuming for simplicity a Gaussian distribution of angles for the calculation of the weighted average.

The 'external' wind-angle variability σ_e is estimated from Eq. (3.6), where σ_α is obtained from the Prairie Grass experiments. In case of a neutral boundary layer, σ_m is obtained from the turbulence closure, i.e. assuming isotropic turbulence we find (cf., e.g., Ref. [108])

$$\langle u \rangle^2 \sigma_m^2 = \langle v_m'^2 \rangle \approx \frac{2}{3} \frac{u_\tau^2}{\sqrt{C_\mu}}, \tag{3.17}$$

with $C_\mu = 0.09$. When the boundary layer is thermally stratified, σ_m can be obtained by applying the level 2 model of Mellor and Yamada [86] to the surface layer of the ABL, resulting in

$$\langle u \rangle^2 \sigma_m^2 = \langle v^2 \rangle \approx \gamma_1 \left(\frac{u_\tau}{\phi_M S_M} \right)^2 \tag{3.18}$$

with S_M given by

$$S_M = \left(\frac{\phi_M^{-4}}{B_1 (1 - R_f)} \right)^{\frac{1}{3}} \tag{3.19}$$

and with $\gamma_1 \approx 0.22$ and $B_1 \approx 16.6$, two empirical constants [86]. In case of very strong stable stratification, the level 2 model of Mellor and Yamada [86] might result in $\sigma_m^2 \geq \sigma_\alpha^2$. In this case, no additional boundary condition for σ_e^2 is imposed.

3.2.3 Performance criteria

Since we have a large number of measurement positions in combination with many different cases, it is useful to employ a set of global performance criteria that allow to synthesize the quality of a modeling approach into a limited set of quality measures (next to the more conventional presentation of concentration profiles that will also be used in §3.3). To that end, we use a set of performance criteria proposed by Chang and Hanna [30], i.e., the fractional bias (FB), the geometric mean bias (MG), the normalized mean square error (NMSE), the geometric variance (VG), and the fraction of predictions within a factor of two of observations (FAC2). These criteria are based on differences of mean concentrations observed in the experiments ($c^*_{E,i,j}$) and predicted concentrations in simulations ($c^*_{S,i,j}$), obtained at different measurement points i, and for different experiments/simulations j ($i = 1 \cdots n_j$, $j = 1 \cdots m$, and define $N = \sum_j n_j$), and are defined as [30]

$$\mathrm{FB} = \frac{\sum_{i,j} \left(c^*_{E,i,j} - c^*_{S,i,j} \right)}{\sum_{i,j} \left(c^*_{E,i,j} + c^*_{S,i,j} \right) /2}, \tag{3.20}$$

$$\mathrm{MG} = \left(\prod_{i,j} \frac{c^*_{E,i,j}}{c^*_{S,i,j}} \right)^{1/N}, \tag{3.21}$$

$$\mathrm{NMSE} = N \frac{\sum_{i,j} \left(c^*_{E,i,j} - c^*_{S,i,j} \right)^2}{\left(\sum_{i,j} c^*_{E,i,j} \right) \left(\sum_{i,j} c^*_{S,i,j} \right)}, \tag{3.22}$$

$$\mathrm{VG} = \exp\left(\sum_{i,j}\left(\ln\left[\frac{c^*_{E,i,j}}{c^*_{S,i,j}}\right]\right)^2\right), \tag{3.23}$$

$$\mathrm{FAC2} = \text{fraction of data } (i,j) \text{ that satisfy:} \quad 0.5 \leq \frac{c^*_{S,i,j}}{c^*_{E,i,j}} \leq 2.0. \tag{3.24}$$

From these definitions it is readily seen that a perfect match between model and observations would lead to MG, VG, and FAC2 = 1.0; and FB and NMSE = 0.0. For air-quality modeling, Chang and Hanna [30] propose a set of model acceptance criteria that are given by: $-0.3 < \mathrm{FB} < 0.3$, $0.7 < \mathrm{MG} < 1.3$, $\mathrm{NMSE} < 4$, $\mathrm{VG} < 1.6$, and $\mathrm{FAC2} > 0.5$. Although not a part of the performance criteria of Chang and Hanna [30], we will also look at FAC10, defined similar to FAC2 as

$$\mathrm{FAC10} = \text{fraction of data } (i,j) \text{ that satisfy:} \quad 0.1 \leq \frac{c^*_{S,i,j}}{c^*_{E,i,j}} \leq 10.0. \tag{3.25}$$

A perfect match between model and observations would yield FAC10 = 1. Finally, various other quality measures exist, among which the hit-rate has been studied much recently (cf., e.g., Ref. [119]). However, for sake of brevity, we limit ourselves to the 6 measures defined above.

Remark that in the measures defined above, all measurement points are taken into account i.e. without imposing a concentration threshold, following a so-called paired-in-space approach [30].

3.3 Results and discussion

In the current section, we validate the proposed approach to include variable wind direction in RANS simulation, using the estimated ‘external’ wind-angle variability σ_e versus the Prairie Grass experiments (‘σ_e–RANS’). For comparison, we also add results obtained using three other models: (1) RANS simulations using the mean-wind direction only (‘mean-wind RANS’), (2) RANS simulations using the total wind variability σ_α (as, e.g., Ref. [104, 132]) (‘σ_α–RANS’), and (3) a classical Gaussian model using the Briggs rural dispersion parameters [134].

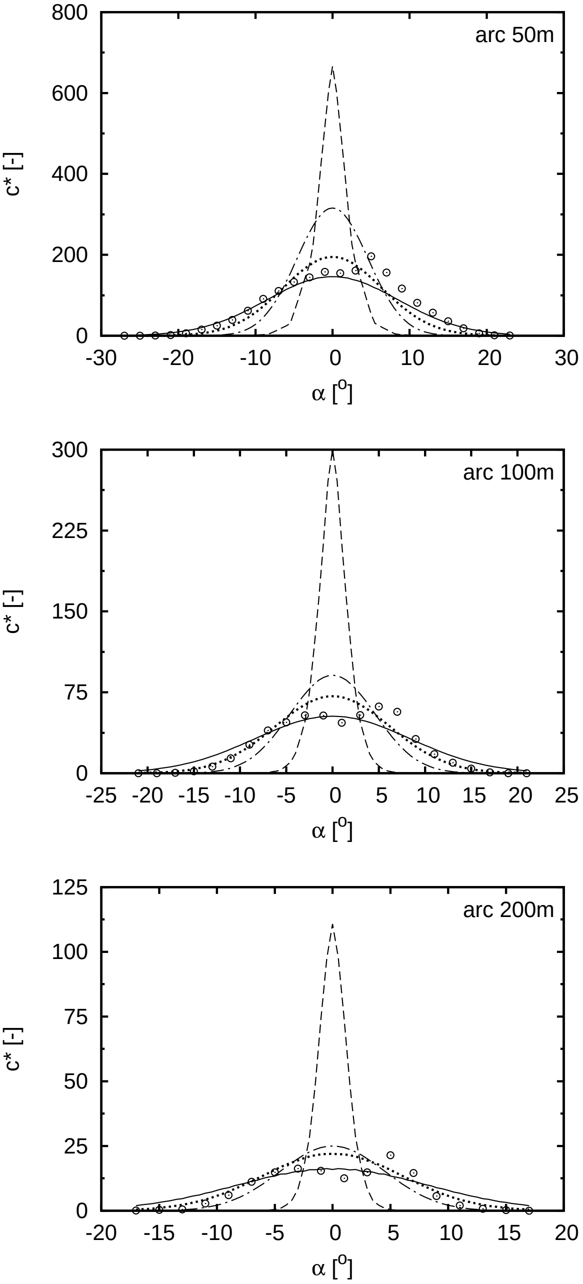
arc 50m
c* [-]
0
200
400
600
800
-30
-20
-10
0
10
20
30
α [o]
arc 100m
c* [-]
0
75
150
225
300
-25
-20
-15
-10
-5
0
5
10
15
20
25
α [o]
arc 200m
c* [-]
0
25
50
75
100
125
-20
-15
-10
-5
0
5
10
15
20
α [o]

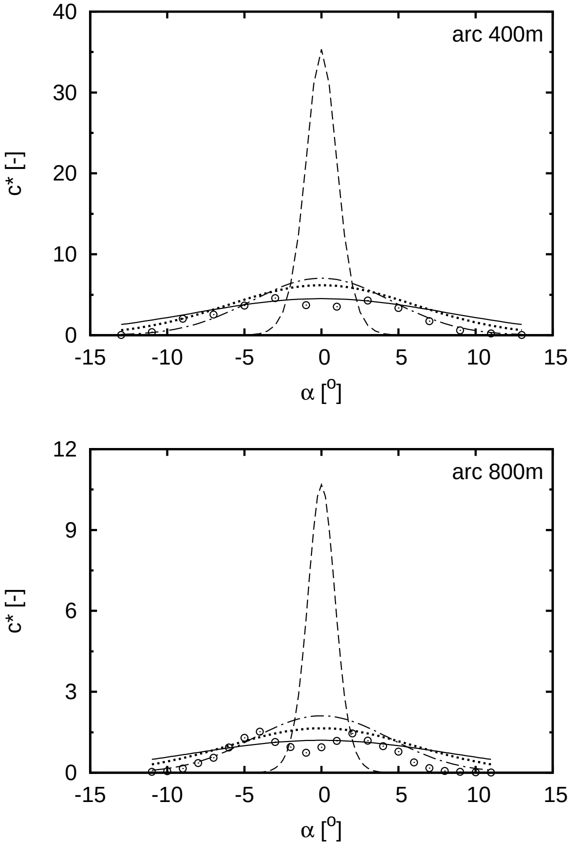

Figure 3.3: Profiles of non-dimensional concentration c^* $(= \langle c \rangle UL^2/r)$ for Prairie Grass experiment 45 along the five observation arcs of the experiment (cf. Fig. 3.2), 'mean-wind RANS' simulation (−−), Gaussian dispersion model (− · −·), 'σ_α–RANS' simulation (—), 'σ_e–RANS' simulation $(\cdots)$, and non-dimensional 10-min averaged concentrations from experiments $(\odot)$.

3.3.1 Typical simulation result: Prairie Grass experiment no. 45

As typical example we selected experiment 45, having measurements available for all five arcs and three of the six towers, i.e. Tower 1, 2, and 3 – cf. Fig. 3.2 (because of different wind directions, most other experiments have less tower data). The mean wind direction during this experiment was $\alpha_m = 19°$ (i.e. almost straight in the direction of Tower 2, that was located at an angle of 21°), and wind was fluctuating with a standard deviation $\sigma_\alpha = 8.2°$, measured at 2 m above the ground. The mean stream-wise velocity at this height was equal to 5.75 m/s and friction velocity is computed to be 0.394 m/s. Using Eqs. (3.6) and (3.17), this results in a reduced standard deviation σ_e of 5.95°.

In Fig. 3.3, non-dimensional concentration (c^*) profiles are shown along the arcs as obtained in the experiment, and from the four simulation approaches considered. First of all, it is observed that the 'mean-wind RANS' simulation strongly overpredicts the centerline concentrations (at angle $\alpha = 0°$), and significantly underestimates the lateral plume spread at all five arcs. When looking at the concentration at the towers for this case in Fig. 3.4, we observe that due to this insufficient plume spread, the concentration at towers 1 and 3 is far below the experimental observations (i.e. the lines collide with the ordinate, and are not visible on the plot) while the concentration at tower 2 (roughly lying in the direction of the mean wind for the current case) is overpredicted by more than a factor of two. Looking at the results of the Gaussian model in Figs. 3.3 and 3.4, we find that they more closely match the observations. Nevertheless, this model also fails in capturing the plume spread properly: at observation arcs near the pollutant source, the concentration decreases too quickly with increasing angle, and concentration levels at $\alpha = 0°$ are too high. Again, this lack of lateral spread causes improper predictions at the towers with a strong underprediction of the concentration at towers 1 and 3 and an overprediction at tower 2.

The 'σ_α–RANS' (using the total observed variability) closely matches centerline concentrations observed in the experiments, and yields the largest plume spread of all four models. Due to this large plume spread, the concentrations at the tails of the observation arcs are overpredicted (Fig. 3.3), even at short distances from the source. This is also observed in the predicted tower profiles (Fig. 3.4) where 'σ_α–RANS' simulations overpredict concentrations at tower 1 and tower 3.

Looking at the 'σ_e–RANS' simulations in Fig. 3.3, we find that plume spread is reduced compared to σ_α results, lowering and therefore improving the prediction of the concentrations in the tails of the observation arcs. The

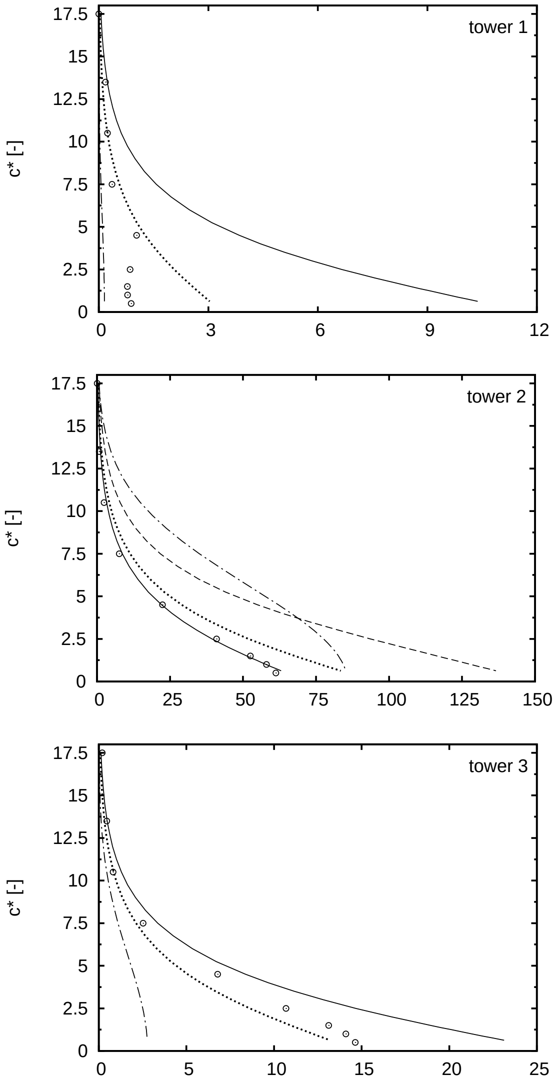

Figure 3.4: Profiles of non-dimensional concentration c^* ($= \langle c \rangle UL^2/r$) for Prairie Grass experiment 45 observed at Tower 1, 2, and 3 of the experiment (cf. Fig. 3.2), 'mean-wind RANS' simulation (−−), Gaussian dispersion model (− · −·), 'σ_α–RANS' simulation (—), 'σ_e–RANS' simulation ($\cdots$), and non-dimensional 10-min averaged concentrations from experiments (⊙).

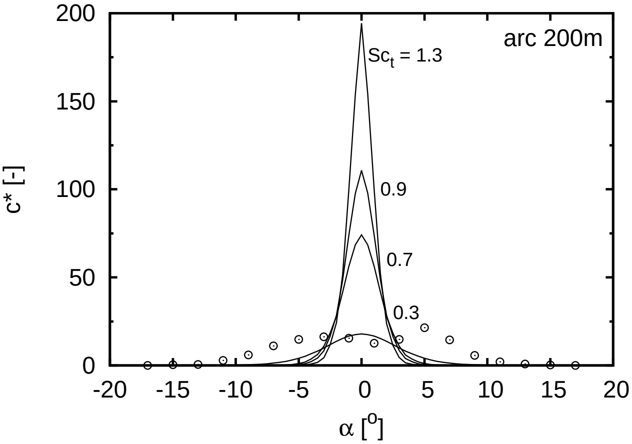

Figure 3.5: Profiles of non-dimensional concentration c^* ($= \langle c \rangle UL^2/r$) for Prairie Grass experiment 45 observed at the 200m arc in the field set-up (cf. Fig. 3.2) for the 'mean-wind RANS' simulation as function of Sc_t, and non-dimensional 10-min averaged concentrations from experiments ($\odot$).

centerline concentrations are slightly raised compared to those from the 'σ_α–RANS' simulations, but remain well-acceptable. In addition, because of the improved plume spread predictions, the tower profiles in Fig. 3.4 improve significantly.

In Fig. 3.5, the effect of changing Sc_t of the 'mean-wind RANS' simulation is shown – this is an approach that is sometimes followed to improve concentration predictions (cf., e.g., Ref. [17]). We observe that changing Sc_t strongly affects the peak concentration at ground level, and a relatively good agreement between peak concentrations and experiments is found for $Sc_t = 0.3$. However, the horizontal spreading is hardly affected and remains unsatisfactory. Instead, we find that concentrations at higher altitudes (not shown here) are strongly overpredicted.

Finally, for more complex geometries (e.g. buildings, canopy, ...) the analytical profiles for velocity and eddy viscosity are generally not known. Instead, the full flow equations have to be solved in combination with the estimated level of variability before the advection-diffusion problem can be solved. By way of illustration, this is applied to the Doel Nuclear Power Station to evaluate pollutant concentration due to a steady release from the Doel 3 chimney (see §5.2.1 for a detailed discussion of the site). More precisely, the steady-state concentration field and the resulting gamma dose rate is computed as a weighted average of seven wind directions. The atmospheric conditions are taken the same as Gueibe *et al.* [56]. The result is shown as the 'CFD Doel' model in Fig. 1.4. Note that also for the 'CFD Openfield' model, σ_e is accounted for as a boundary condition.

3.3.2 Analysis of the experiments with neutral stability

In order to provide a more significant comparison of different models that is not just based on a number of concentration profiles for a few selected cases, we now turn to a comprehensive analysis of the full data set obtained by simulating the 15 Prairie Grass experiments with neutral stratification (cf. §3.2.1).

In Fig. 3.6, a scatter plot is provided for each of the four models, that displays the value of the model predictions versus the corresponding experimental observations for all 15 experiments, and all observation points. In these graphs, points plotted using a solid circle represent the arc centerline concentrations, i.e. the concentrations along the wind direction through the point of release, while the crosses represent all other measurements. The solid triangles on abscissa indicate predicted concentrations falling below the range of the graph. First of all, it is observed (Fig. 3.6a) that the 'mean-wind RANS' simulations systematically overestimate all centerline concentrations with at least a factor of two and several with more than a factor of ten. The Gaussian model (Fig. 3.6b) performs slightly better with respect to this, reproducing all but one centerline concentration within a factor of ten from the measurements. Both variable-wind models (Fig. 3.6c,d) are better able to predict the centerline concentrations, and for most cases simulated concentrations fall within a factor of two of experimental observations. Note that at ground level (important for potential health impact), 'σ_e–RANS' yields slightly higher concentrations overall than 'σ_α–RANS'. The difference is however not very large, and well within the scatter observed between predicted ground-level concentrations at different points. Moreover, 'σ_e–RANS' results are a bit more conservative, with less under-prediction of experimentally observed peak concentrations.

When taking the off-centerline measurements into account in Fig. 3.6, the 'mean-wind RANS' simulations as well as the Gaussian model underpredict the majority of the concentrations, and many of them by several orders of magnitude. Much less scatter is observed with the variable-wind RANS simulations (using either σ_α or σ_e). These models manage to predict most of the concentrations within a factor of ten of the measurements. At lower concentrations however, 'σ_α–RANS' simulations (Fig. 3.6c) overpredict the majority of the concentrations. In that range the 'σ_e–RANS' approach clearly exhibits less bias in its predictions.

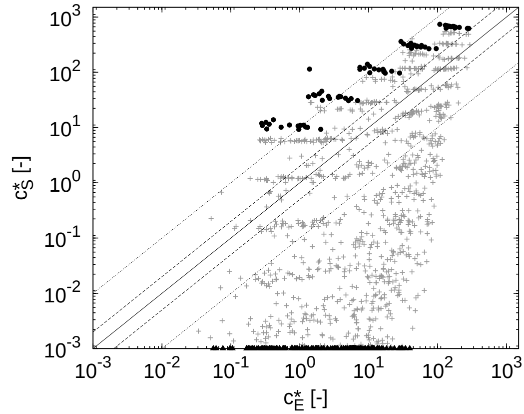
c_S^* [-]
10^{-3}
10^{-2}
10^{-1}
10^{0}
10^{1}
10^{2}
10^{3}
c_E^* [-]

(a)

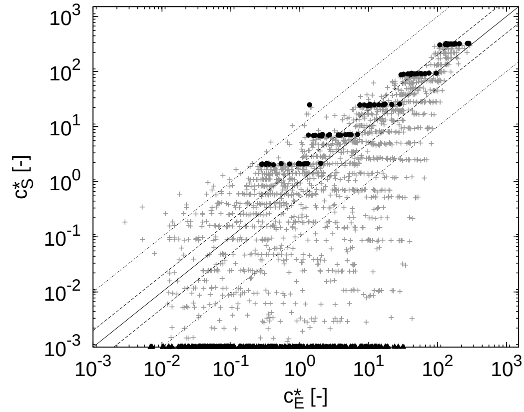
c_S^* [-]
10^{-3}
10^{-2}
10^{-1}
10^{0}
10^{1}
10^{2}
10^{3}
c_E^* [-]

(b)

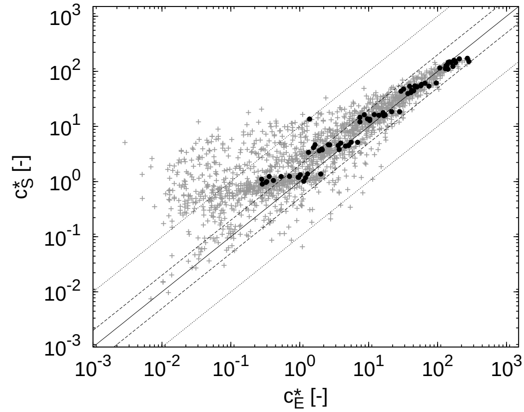
c_S^* [-]
10^{-3}
10^{-2}
10^{-1}
10^{0}
10^{1}
10^{2}
10^{3}
c_E^* [-]

(c)

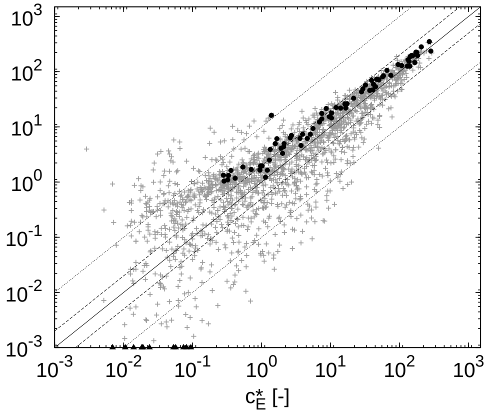

(d)

Figure 3.6: Scatter plot of the simulated versus experimentally observed concentrations (c_S^* versus c_E^* where $c^* = \langle c \rangle UL^2/r$) at observation arcs and towers for the 15 Prairie Grass experiments considered in the current study. Symbols: (●): peak concentrations; (▲): simulation results with $c_S^* \leq 10^{-8}$; (+): all other points. Lines: (—): $c_S^* = c_E^*$; (– –): $c_S^* = 2^{\pm 1} c_E^*$; ($\cdots$): $c_S^* = 10^{\pm 1} c_E^*$. (a) 'mean-wind RANS' simulations, (b) Gaussian model, (c) 'σ_α–RANS' simulations, and (d) 'σ_e–RANS' simulations.

To further evaluate the different modeling approaches, their respective performance criteria following Hanna *et al.* [61] are given in Table 3.4 (cf. §3.2.3 for definitions). Measures that meet the acceptance criterion are indicated in bold. The different values in the table are now briefly discussed. The FB and MG measures are both indicators of mean relative bias and therefore indicate systematic errors in the model predictions. All four models meet the FB criterion although the 'variable-wind' CFD models (either using σ_α or σ_e) show a significantly smaller bias compared to the two other models. All FB values are negative, indicating that all models have on average the tendency to overpredict the concentration. Looking at MG in Table 3.4, it is observed that only the 'σ_e–RANS' simulations manage to meet the acceptance criterion. In contrast to FB that is predominantly influenced by the higher concentrations, MG is evenly influenced by all concentrations.

The NMSE and the VG criteria are both measures of the mean relative scatter and reflect both systematic and random errors [61]. While NMSE is predominantly influenced by the higher concentrations, MG is evenly influenced by all concentrations. Although both 'variable-wind' RANS models and the Gaussian model meet the NMSE criterion, only the 'σ_e–RANS' simulations

Table 3.4: Comparison of statistical performance measures of four models applied to 15 Prairie Grass experiments (cf. §3.2.3 for definitions). Performance measures that fall within the acceptance limits set by Hanna *et al.* [61] are highlighted in bold.

	Gaussian model	mean-wind RANS simulation	σ_α–RANS simulation	σ_e–RANS simulation
FB	**-0.133**	**-0.144**	**-0.044**	**-0.049**
MG	13.880	26.790	0.461	**0.824**
NMSE	**1.98**	5.844	**0.376**	**0.405**
VG	1.01×10^3	4.957×10^4	1.821	**1.038**
FAC2	0.337	0.1206	**0.569**	**0.512**
FAC10	0.698	0.4032	0.879	0.901

meet the VG criterion. The ‘mean-wind’ RANS model meets neither criteria.

Finally, both ‘variable-wind’ CFD models succeed in having more than 50% of the concentrations within a factor of two of the observations (FAC2). In addition, both have approximately 90% of the predictions fall within a factor of ten of the observations (FAC10). The two other models perform significantly less well with about 34% and 70%, respectively, for the Gaussian model and about 12% and 40%, respectively, for the single-wind CFD model.

Based on the results in Table 3.4, we conclude that the ‘σ_e–RANS’ model is the only one that meets all model acceptance criteria set by Chang and Hanna [30]. The model particularly succeeds in better reproducing low concentrations without significant bias. Although ‘σ_α–RANS’ performs well for the linear measures FB and NMSE, the logarithmic measures MG and VG show that the model has a systematic bias at low concentrations. This also applies to the Gaussian model which, in addition, fails to predict 50% of the concentrations within a factor of two of the observations. The mean-wind RANS performs worst, and only meets the FB criterion.

3.3.3 Analysis of the cases with stratified atmospheric conditions

An analysis of full data set of the cases with stable and unstable stability is presented next. A scatter plot that displays the value of the model predictions versus the corresponding experimental observations in case of stable stratification for the four models studied is provided in Fig. 3.7. First of all, it is again observed that the 'mean-wind RANS' simulations (Fig. 3.7a) systematically overestimate the centerline concentrations, often by more than a factor of two although non by more than a factor of ten. The Gaussian model (Fig. 3.7b) reproduces all centerline concentrations within a factor of ten from the observations although both multiple over- and underestimations by more than a factor of two are found. The 'σ_α–RANS' simulations (Fig. 3.7c) systematically underestimate the centerline concentrations of which several by more than a factor of two. In case of the 'σ_e–RANS' simulations (Fig. 3.7d) however, the centerline concentrations are well reproduced with only a few predictions off by more than a factor of two.

When taking the off-centerline measurements into account, the 'mean-wind RANS' model underestimates the majority of the low concentrations measured, and many of them by several orders of magnitude. The 'σ_α–RANS' approach on the other hand, shows a clear bias towards overestimating these concentrations. The Gaussian model and the 'σ_e–RANS' approach falls between the two other models, showing a very similar scattering pattern.

To quantitatively evaluate the modeling approach, an evaluation of the performance criteria following Chang and Hanna [30] is given in Table 3.5 for the centerline concentrations and all measurements, respectively. With respect to the centerline concentrations, the 'σ_e–RANS' approach performs markedly better than the three other models, meeting all performance measures regardless the thermal stratification. The 'σ_α–RANS' approach shows a systematic bias towards underestimating the centerline concentrations while the 'mean-wind RANS' is overly conservative. The Gaussian model performs relatively well, failing only the MG criterion in case of unstable stratification. When taking the off-centerline measurements into account, the 'mean-wind RANS' approach again performs the worst, mainly due to the large number of strongly underestimated concentrations, e.g. with MG and VG virtually infinite as a result. In case of unstable stratification, the Gaussian model meets only the NMSE criterion but, in case of stable stratification, also the FB falls within the acceptance limits. The 'σ_e–RANS' and 'σ_α–RANS' performance measures are comparable but the 'σ_e–RANS' approach is closer to the optimal value. Finally note that under strong stable stratification, the external variability σ_e (cf. Eq. 3.6) becomes negligible with respect to modeled σ_m i.e. 'σ_e–RANS' converges towards 'mean-wind RANS'. Under strong unstable stratification on the other hand, the modeled variability σ_m (cf. Eq. 3.6) becomes negligible with respect to σ_e and 'σ_e–RANS' converges towards 'σ_α–RANS'.

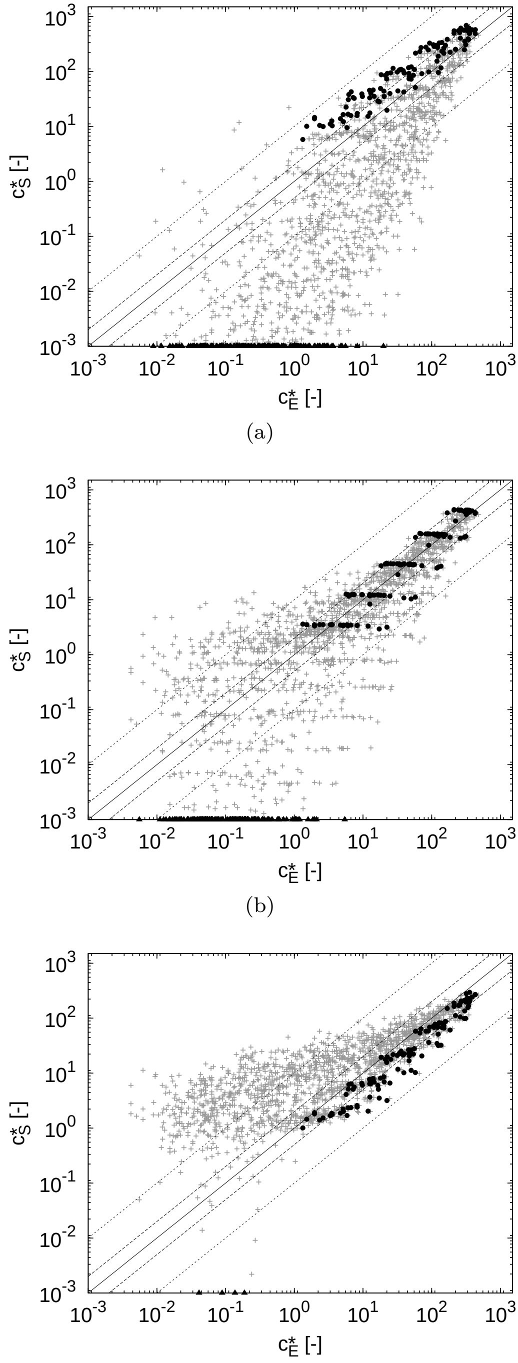

(a)

(b)

(c)

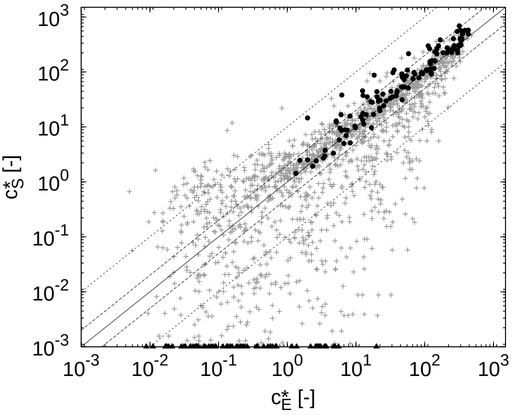

(d)

Figure 3.7: Scatter plot of the simulated versus experimentally observed concentrations (c_S^* versus c_E^* where $c^* = \langle c \rangle UL^2/r$) at observation arcs and towers for the 24 Prairie Grass experiments with stable stratification. Symbols: (●): peak concentrations; (▲): simulation results with $c_S^* \leq 10^{-8}$; (+): all other points. Lines: (—): $c_S^* = c_E^*$; (− −): $c_S^* = 2^{\pm 1} c_E^*$; ($\cdots$): $c_S^* = 10^{\pm 1} c_E^*$. (a) 'mean-wind RANS' simulations, (b) Gaussian model, (c) 'σ_α–RANS' simulations, and (d) 'σ_e–RANS' simulations.

3.4 Conclusions

In this chapter, we introduced a simple approach to estimate, based on experiments, the correct level of variability in wind direction that is required for Reynolds-averaged simulations of pollutant dispersion in the atmosphere. In these simulations, fluctuations in wind directions are already partly accounted for by the modeled turbulence; and hence, the effective variability that should be used as a boundary condition to the simulations, needs to be lower than experimentally measured. Based on this rationale, and the turbulence level in the simulation, it is now possible to estimate the required 'external' variability.

To assess the approach, we performed a series of numerical simulations covering 45 of the Prairie Grass experiments [10], i.e. 24 characterized by stable conditions, 15 characterized by neutral conditions, and 6 characterized by unstable conditions. Four different models were compared, i.e., (1) a Gaussian model, and RANS simulations, either using (2) only the mean wind direction ('mean-wind' RANS), (3) using the full wind-direction variability as observed in the experiment ('σ_α–RANS'), or (4) using a reduced level of variability ('σ_e–RANS'). We found that including wind variability significantly

Table 3.5: Comparison of statistical performance measures (cf. §3.2.3 for definitions) of four models applied to the Prairie Grass experiments under unstable (6 experiments, 1066 measurements) and stable (24 experiments, 1841 measurements) thermal stratification. Performance measures that fall within the acceptance limits set by Hanna *et al.* [61] are highlighted in bold.

Centerline measurements		FB	MG	NMSE	VG	FAC2	FAC10
unstable	Gaussian model	**-0.119**	0.606	**0.583**	**1.286**	**0.667**	0.993
	mean-wind RANS	-1.295	0.104	6.483	168.7	0.000	0.500
	σ_α–RANS	0.356	**0.889**	**1.148**	**1.014**	**0.767**	0.967
	σ_e–RANS	**0.293**	**0.835**	**0.968**	**1.033**	**0.767**	0.967
stable	Gaussian model	**-0.163**	**0.986**	**0.308**	**1.000**	**0.761**	1.000
	mean-wind RANS	-0.569	0.444	**0.786**	1.931	0.436	1.000
	σ_α–RANS	0.518	1.904	**0.691**	**1.514**	**0.615**	1.000
	σ_e–RANS	**-0.264**	**0.757**	**0.349**	**1.080**	**0.855**	1.000
All measurements							
unstable	Gaussian model	0.401	35.24	**2.563**	Inf	0.285	0.639
	mean-wind RANS	**0.043**	Inf	11.56	Inf	0.069	0.216
	σ_α–RANS	**0.101**	0.464	**1.210**	1.802	**0.526**	0.873
	σ_e–RANS	**0.093**	0.491	**1.090**	1.658	**0.526**	0.878
stable	Gaussian model	**0.032**	3.020	**0.662**	3.396	0.481	0.768
	mean-wind RANS	**0.117**	Inf	**1.626**	Inf	0.205	0.447
	σ_α–RANS	**0.142**	0.339	**0.913**	3.213	0.442	0.750
	σ_e–RANS	**0.112**	Inf	**0.742**	Inf	0.483	0.738

improves predictions over 'mean-wind' RANS models, and the Gaussian model. However, when using the full range of variability measured in experiments ('σ_α–RANS') lateral plume spreading is overpredicted. Reducing the variability by removing what is already represented in the RANS turbulence model, leads to a significant improvement of predictions.

To quantify this, we employed the model performance criteria of Chang and Hanna [30], and found that the 'σ_e–RANS' simulations are the only ones that meet all acceptance levels in case of neutral stratification. In case of stable and unstable stratification, we found that the model is well capable of reproducing the centerline concentrations, meeting the model performance criteria regardless the stratification. When taking the off-centerline measurements into account, the model reproduces the high concentrations without a significant bias or scatter and improves the prediction of the lower concentrations compared to the 'mean-wind RANS' and 'σ_α–RANS' simulations.

Chapter 4

Accounting for wind field variability

In the current chapter, we study the time-evolution of the turbulent dispersion of radioactive gases in the atmospheric boundary layer and the resulting radiological dose at ground level. To this end, the LES model is coupled with the beta and gamma dose rate models (cf. Sections 2.3 and 2.4). This allows to perform time-dependent simulations which can provide keen insight into the variability of the dose rate due to the variability of the wind field. The computational cost of this approach can be significant (cf. §4.1.2). However, the strength of this approach is that the variability can be accounted for in the dispersion simulation without the need for highly temporal meteorological wind field data which would be required for, for example, Gaussian puff models and particle models [106]. Using this coupled model, a series of time-dependent simulations of a steady release of ^{41}Ar and ^{133}Xe for 4 different release heights into an open field are performed. The variability of the dose rate from beta and gamma radiation at ground level is studied with a particular focus on the differences between both types of radiation.

The material in this chapter is composed from

"Lieven Vervecken, Johan Camps, and Johan Meyers. Dynamic external dose assessment by LES modeling of radioactive pollutant dispersion over an open field. *Abstract book of the Fourth European IRPA Congress*, Abstract No. 4-3-4. 2014", and

"Lieven Vervecken, Johan Camps, and Johan Meyers. Dynamic dose assessment by Large Eddy Simulation of the near-range atmospheric dispersion. *Journal of Radiological Protection*, 35(1):165–178, 2015.".

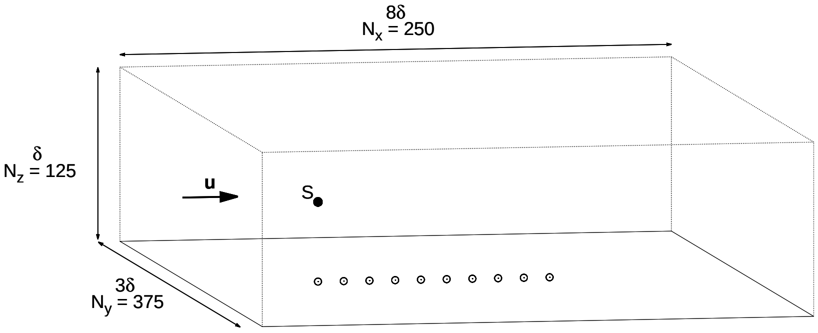

Figure 4.1: Outline of the simulated domain. Symbols: (•) Pollutant source; (∘): monitoring point.

This chapter is further organized as follows. First, Section 4.1 details the numerical set-up of our simulations. The results of simulations are discussed in Section 4.2. Finally, conclusions are presented in Section 4.3.

4.1 Case set-up

First, the set of cases studied in this work are discussed in §4.1.1. The computational set-up used to solve the dispersion problem and to perform the dose assessment is elaborated in §4.1.2.

4.1.1 Case description

The geometry of the cases studied is very simple as shown in Fig. 4.1, i.e. an open field without any obstructions from buildings or vegetation. The simulation domain chosen is of size $8\delta \times 3\delta \times \delta$ where δ is the boundary layer thickness. The pollutant source is positioned $2/3\delta$ downstream from the inlet boundary, and in the middle of the domain in crosswind direction. Four different pollutant release heights are considered in this study, i.e. 0.06δ, 0.10δ, 0.14δ and 0.18δ, which correspond to 45 m, 75 m, 105 m and 135 m for a boundary layer with a thickness of 750 m. Fluence rates are monitored at ground level ($2 \times 10^{-3}\delta$ or 1.5 m for $\delta = 750$m) at multiple distances from the point of release along stream-wise direction as illustrated in Fig. 4.1.

Two noble gases are selected as the subject of our study i.e. ^{41}Ar and ^{133}Xe. These gases are inert and do not deposit. Both are frequently emitted in routine

Table 4.1: Simulation characteristics.

Parameter	Value
Domain size	$8\delta \times 3\delta \times \delta$
Number of grid cells	$250 \times 375 \times 125 \sim 11.7$ million cells
Roughness length	$1.333 \times 10^{-5}\delta$ (short grassland)
Boundary layer thickness	750 m
Initial conditions	log-profile modified with random velocity fluctuations
Warm up period	stabilization of the total kinetic energy
Dose assessment frequency	every two time steps

operation of various nuclear facilities [66, 111] and especially ^{133}Xe might be emitted in large quantities in nuclear accidents [42]. A high energy gamma of $E_\gamma = 1\,293.64$ keV is emitted when ^{41}Ar decays to ^{41}K by beta minus decay with a decay constant of 105.36×10^{-6} s^{-1} [14]. Conversely, a low energy gamma of $E_\gamma = 81.0$ keV is emitted during the beta minus decay of ^{133}Xe to ^{133}Cs. The decay constant of this process is 1.53×10^{-6} s^{-1} [13].

4.1.2 Computational set-up

The dose assessment problem is simulated using the OpenFOAM finite-volume open-source simulation platform. The main characteristics of the simulation are shown in Table 4.1. The transport equations are discretized on a uniformly spaced, hexahedral mesh using second-order schemes. The second-order Crank–Nicholson scheme is applied for time discretization. Coupling between velocity and pressure is accomplished through the projection scheme (see, e.g., Ref. [93]). A pressure gradient is imposed along the x-direction as the driving force of the flow. The pollutant source is modelled as a point source by simply adding a source term to the corresponding cell in the domain.

Periodic boundary conditions are set in the horizontal directions for all variables, therefore simulating a domain of infinite depth and width. For all variables except the velocity, Neumann boundary conditions are applied at the other boundaries. To suppress recycling of the pollutant to the inlet, an additional sink term $-\alpha C$ is added to the concentration equation (cf. Eq. 2.23) with $\alpha = 0.5$ for $7\delta < x < 8\delta$ and $\alpha = 0$ otherwise. For the velocity, a stress boundary condition is imposed at the bottom of the domain to simulate the effect of the wall layer (see, e.g., Ref. [21]):

$$\tau_{i,3}^{wall}(x,y) = -\left[\frac{\kappa}{\ln(dz/2z_0)}\right]^2 (\hat{\hat{u}}_1^2 + \hat{\hat{u}}_2^2)^{1/2} \left[\hat{\hat{u}}_i(x,y,dz/2)\right] \tag{4.1}$$

where dz is the height of the first grid cell, z_0 is the roughness length, u_1 and u_2 are the horizontal velocity components (index 3 indicates the vertical component). In addition, the vertical velocity is set to zero. At the top of the domain, a symmetry condition is imposed.

The gamma fluence rate integral Eq. (2.26) is simply evaluated as the sum of the contribution of each cell individually:

$$\phi^*_{\boldsymbol{x_0}} = \frac{\lambda^*}{4\pi L} \sum_i \frac{B(\mu, r_i)}{r_i^2} e^{-\mu r_i} V_i c_i^* \tag{4.2}$$

where r_i is now the distance from $\boldsymbol{x_0}$ to the cell-centre of cell i and V_i is the volume of cell i. Hence, each cell in the domain is treated as a radioactive point source. However, this approach becomes inaccurate for grid points close to the source. Therefore, the cells with a centre within a radius $V_r^{1/3}$ from the receptor are not included in Eq. (4.2), where V_r refers to the volume of the cell in which the receptor is located. Instead, the average concentration over these cells is computed and this is used to integrate Eq. (2.26) analytically over a spherical volume equal to the total volume of all cells included in the average. Note that this filtering operation is an approximation (see Ref. [73] for a discussion). Since the small time step required for stability of the dispersion simulation is not crucial for an accurate dose assessment, the integration is only performed every two time steps.

The simulations were carried out on 48 processors distributed over four nodes, installed with dual hexa-core Intel Xeon X5650 processors and interconnected through DDR infiniband. On this system, the warm up period to develop the steady flow field takes 13 days. Afterwards, the flow field simulation, the dispersion simulation and the dose assessment run simultaneously at a rate of 125 seconds real time per simulated second. Because post-processing is performed on the fly, the required storage space is limited to 1.9 Gb. Further, instead of reporting dose rates, we bound ourselves to a discussion of the local concentration and the gamma fluence rate to quantify the dose from beta and gamma radiation, respectively, to eliminate the effect of the receptor characteristics on the result. But recall that a conversion can be readily achieved using Eq. (2.25) and Eq. (2.27).

4.2 Results and discussion

The results of the cases studied are presented in this section. First, in §4.2.1, the results of a typical simulation are presented i.e. the dispersion of ^{41}Ar from 0.1δ altitude. Subsequently, a comparison is made between the full set

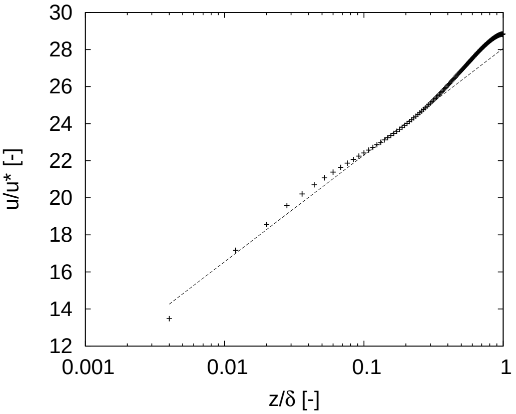

Figure 4.2: Planar and time-averaged vertical velocity profile $\langle u_1 \rangle / u_\tau$ (+) and theoretical profile $\langle u \rangle / u_\tau = (1/\kappa)\ln(z/z_0)$ with $\kappa = 0.4$ and $z_0 = 1.333 \times 10^{-5}\delta$ (−−).

of simulations in §4.2.2. Finally, in §4.2.3, the relevance of time-dependent fluence rate analyses for accident scenarios are discussed.

4.2.1 Typical simulation result: ^{41}Ar dispersion

The dispersion of ^{41}Ar from 0.1δ altitude is selected as a typical example to discuss the simulation results. In Fig. 4.2, the plane- and time-averaged vertical profile of the stream-wise velocity component (u_1) is shown. It is observed that this profile follows the theoretical logarithmic profile of the log-layer fairly well in the lower part of the domain. Further up ($z/\delta > 0.2$), the profile departs from the logarithmic distribution as expected (see, e.g., Ref. [21]). It is found that increasing the vertical grid resolution reduces the small discrepancy between the actual and the theoretical profile in the lower part of the log-layer. The sudden drop in velocity at the cell closest to the wall, however, also results from the discretization but is independent of the grid resolution and can therefore not readily be corrected for [156]. Because the velocity profile behaviour is consistent with other sources, it is argued that the boundary layer flow is captured satisfactory by the present model.

An instantaneous, three-dimensional isosurface of the concentration $c^* = 10^{-5}$ is shown in Fig. 4.3. The turbulent nature of the boundary layer clearly results in a non-uniform plume with a spread increasing with the distance from the point of release. When looking at the concentration in the vertical cross section

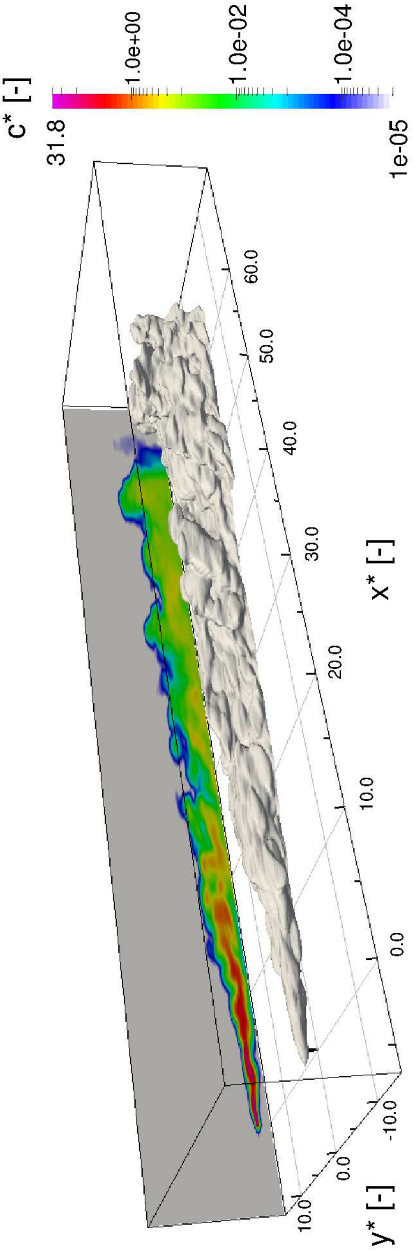

Figure 4.3: Instantaneous ^{41}Ar concentration c^* $(= cUL^2/R)$, released from 0.1δ altitude. In gray, isosurface for $c^* = 10^{-5}$; Back plane, concentration in the stream-wise, vertical cross section through the point of release.

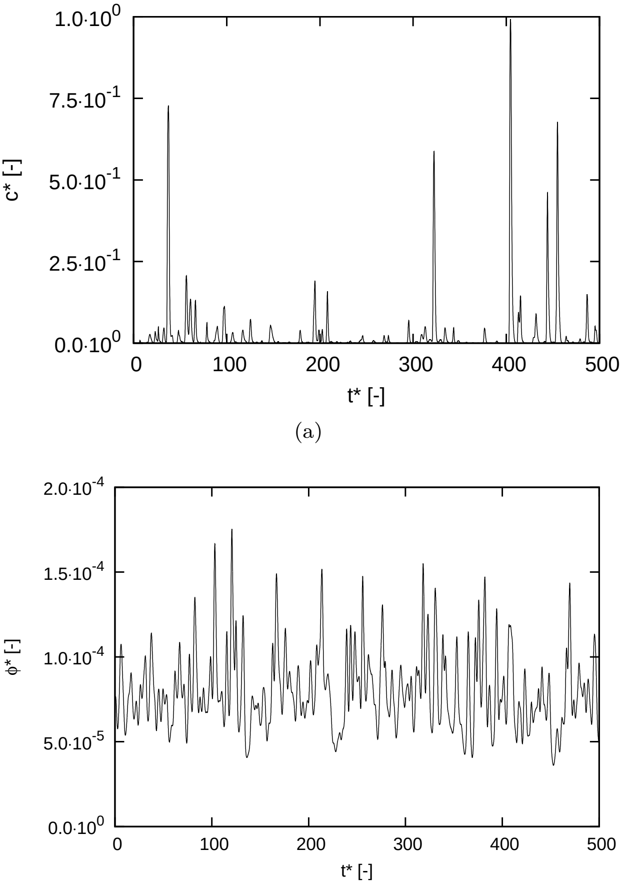

(a)

(b)

Figure 4.4: Observed non-dimensional concentration c^* $(= cUL^2/R)$ (a), and gamma fluence rate ϕ^* $(= \phi L^2/R)$ (b) at $x^* = 10$ $(= x/L)$ at ground level due to the emission of ^{41}Ar from 0.1δ altitude.

through the point of release, plotted on the back plane of Fig. 4.3 (the plane is offset for the sake of visualization), the largest concentration is found in the direct proximity of the pollutant source and strongly decreases with downwind distance. Halfway along the domain, the peak concentration has dropped two orders of magnitude with respect to the maximum concentration, found close to the pollutant source. Correspondingly, the more uniform colouring at larger distance from the pollutant source implies smaller concentration gradients compared to close to the source.

In Fig. 4.4, a part of the simulated time evolution of the non-dimensional concentration c^* and gamma fluence rate ϕ^* are shown, observed at distance $x^* = 10$ downwind from the pollutant source, as a function of the non-dimensional time t^*. It is observed that even with a constant pollutant emission rate, strong fluctuations in time are found. However, a clear difference between the concentration and the gamma fluence rate, i.e. the beta and the gamma radiation, is apparent. The concentration (Fig. 4.4a), and consequently the dose rate from beta radiation, is nearly zero except for large peaks which appear at irregular time intervals. The gamma fluence rate on the contrary (Fig. 4.4b) is very noisy, showing a large number of peaks and troughs. The peaks, however, are significantly larger in magnitude with respect to the mean than the troughs. This is explained as follows. Because of the inverse proportionality with the square of the distance, concentration fluctuations in the vicinity of the observation point affect the fluence rate the strongest. A peak occurs when the plume immerses the observation point and, conversely, a trough occurs when the pollutant concentration in the vicinity of the observation point is low. Nevertheless, despite the fact that the concentration field is time-dependent, the total amount of pollutant in the proximity of an observation point is relatively constant in time due to the constant release rate. Thus, since the fluence rate is influenced by the whole domain (cf. Eq. 2.26), a minimal fluence rate is always present. This minimum rate limits the depth of the troughs.

The wide spread of the instantaneous concentration signal compared to the gamma fluence rate becomes even more clear when inspecting the corresponding probability density functions (pdfs). These are provided in Fig. 4.5a for the concentration, the gamma fluence rate from the decay of ^{41}Ar, and the gamma fluence rate from the decay of ^{133}Xe. For sake of visualization, the gamma fluence rates are rescaled with $U\lambda^{-1}L^{-1}$. The pdf of the concentration stretches from values below 10^{-6} up to 1 with a maximum probability within 5×10^{-4} and 5×10^{-2}. This illustrates that the peaks observed in Fig. 4.4a correspond to an increase in local dose rate of several orders of magnitude. The pdfs of the gamma fluence rate of ^{41}Ar and ^{133}Xe on the other hand are a lot narrower. By computing a moving average of the instantaneous fluence rates with an averaging time of $\Delta^* = 125$, we obtain the pdfs in Fig. 4.5b. To illustrate, in case of a release height of 75 m and a wind speed of 22.5 kmh^{-1} at this altitude, this corresponds to a physical time span of 25 minutes. It is clear that this operation significantly reduces the width of all three pdfs. Nevertheless, the concentration still varies over two orders of magnitude. The gamma fluence rate signal is limited to a very narrow band.

By taking a closer look at the corresponding probability density function (pdf) of the instantaneous gamma fluence rate due to the emission of ^{41}Ar in Fig. 4.6a, it is observed that the data is positively skewed with a mode equal to a

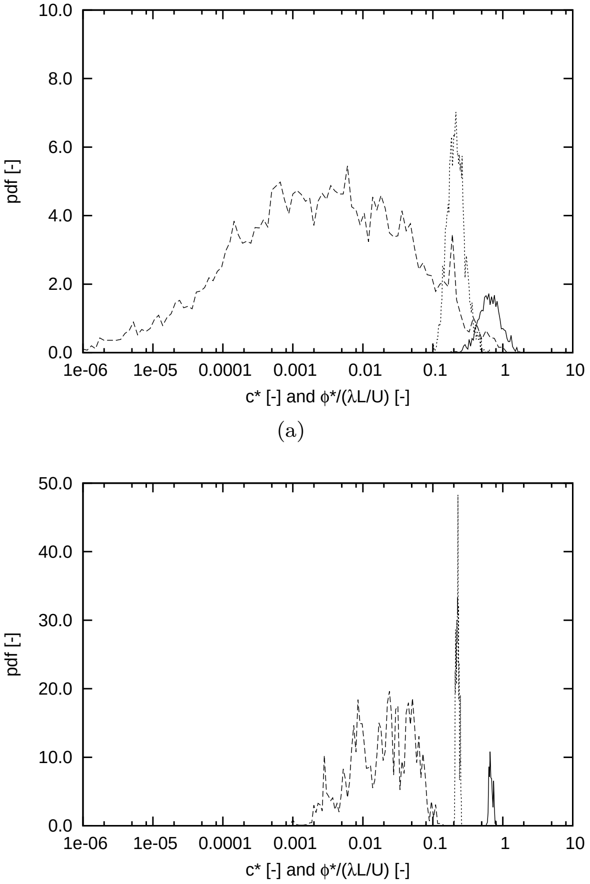

(a)

(b)

Figure 4.5: Probability density function of the concentration c^* ($= cUL^2/R$) (−−) and the gamma fluence rates ϕ^* ($= \phi L^2/R$) of ^{41}Ar ($\cdots$), and ^{133}Xe (–). (a) instantaneous, (b) time-averaged with $\Delta t^* = 125$.

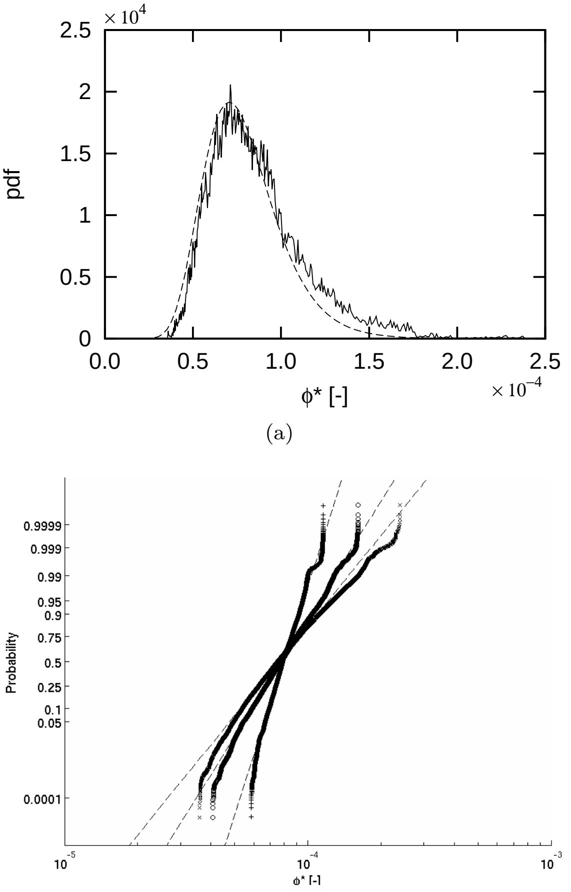

(a)

(b)

Figure 4.6: Probability plot of the observed non-dimensional gamma fluence rate ϕ^* $(= \phi L^2/R)$ at $x^* = 10$ $(= x/L)$ due to the emission of ^{41}Ar from 0.1δ altitude. (a) instantaneous, Lines: (–): Pdf; (——) best-fit log-normal distribution; (b) instantaneous (×), time-averaged with $\Delta t^* = 25$ (○) and time-averaged with $\Delta t^* = 125$ (+); (——) best-fit log-normal distribution.

fluence rate of 7.2×10^{-5} and a mean equal to 8.0×10^{-5}. For the sake of comparison, the pdf of the best-fit log-normal distribution $\ln \mathcal{N}(0.265, 0.284)$ is also added to this graph. Note that other presumed pdfs such as, e.g. the beta distribution, might also be relevant to use. While the left tails are very similar, the right tail of the true pdf is significantly heavier compared to the log-normal distribution. By computing a moving average of the instantaneous fluence rate, the effect of deriving the gamma fluence rate from time-integrated measurement is examined. To this end, $\Delta t^* = 25$ and $\Delta t^* = 125$ are chosen as averaging times. This corresponds, e.g., to 5 and 25 minutes, respectively, for a boundary layer with $\delta = 750$ m and $U = 22.5$ km/h at a height of 75 m. A probability plot of the instantaneous and the time-averaged observations is shown in Fig. 4.6b. The axes of this graph are chosen such that a log-normal distribution results in a straight line. For the sake of reference, the best-fit log-normal distributions for each of the observations are also shown in this graph. It is observed that near the mean value, the probability curves of the observations and the log-normal distribution match closely. But unlike the log-normal distribution, the ranges in fluence rates are clearly finite with distinct minima and maxima. It is readily understood that increasing the averaging time, reduces the spread on the observations by increasing the minimum and decreasing the maximum. Regardless of the averaging time, steeper slopes of the curves and lower probabilities are found at lower fluence rates. This points to lighter left tails compared to the log-normal distribution, while the more moderate slopes and lower probability at higher fluence rates imply heavier right tails.

Finally, in Fig. 4.7, the time-averaged concentration, and gamma fluence rate at ground level are shown. In order to illustrate the spread on the instantaneous observations, the 1^{st} and 99^{th} percentiles are also shown in this figure. It is observed that the time-averaged concentration (Fig. 4.7a) is essentially zero up to $x^* = 5$. From this point on, the concentration increases up to $x^* = 25$ after which it stabilizes. The time-averaged fluence rate is fairly constant along the stream-wise direction for the range plotted with a value between 7.0×10^{-5} and 8.3×10^{-5} (Fig. 4.7b). A clear dependence of the variation on the distance from the stack is observed for both the concentration and the gamma fluence rate. In Fig. 4.7a, the 1^{st} percentile of the concentration observations is found to increase monotonically. The 99^{th} percentile initially increases strongly with increasing distance and shows a wide peak at $x^* \approx 10 \ldots 20$ followed by a steady decrease. For the gamma fluence rate observations (Fig. 4.7b), the 1^{st} percentile is found to decrease monotonically although the rate of decrease diminishes significantly after $x^* = 10$. The 99^{th} percentile initially also increases strongly with increasing distance and peaks at $x^* \approx 13$. Downstream of this point, again a steady decrease is observed.

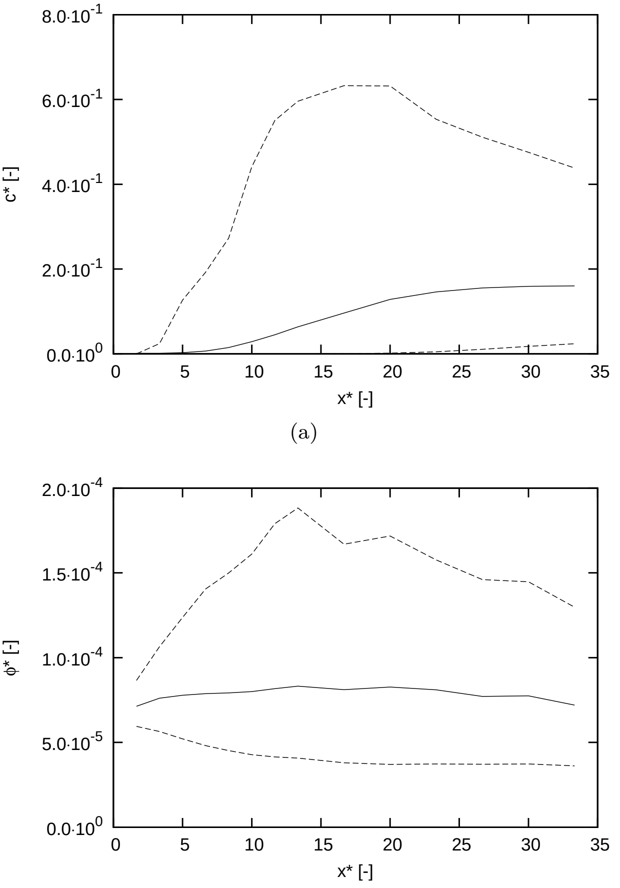

(a)

(b)

Figure 4.7: Time-averaged non-dimensional concentration c^* $(= cUL^2/R)$ (a) and non-dimensional gamma fluence rate ϕ^* $(= \phi L^2/R)$ (b) at ground level due to ^{41}Ar emission from 0.1δ altitude (–) and 1$^{\text{st}}$–99$^{\text{th}}$ percentiles (−−) along the stream-wise direction.

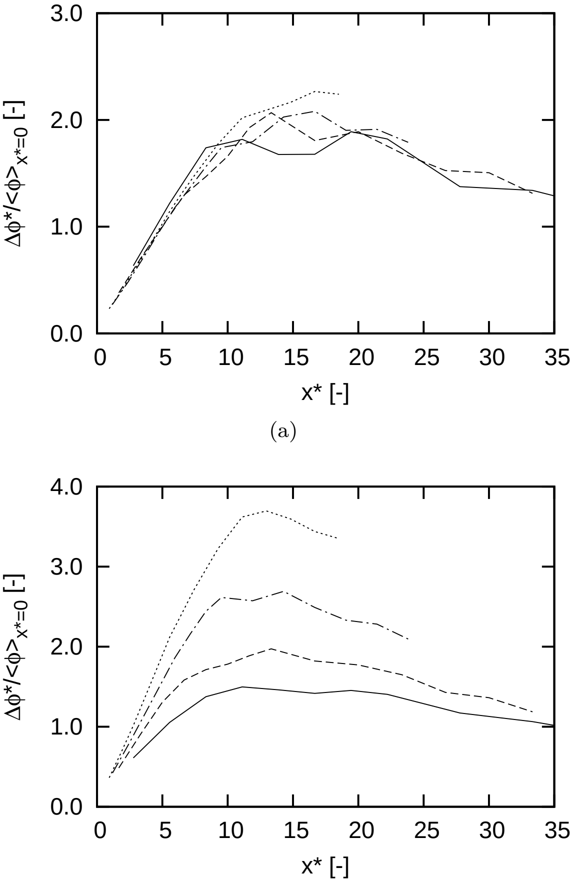

(a)

(b)

Figure 4.8: Interval width between the 1st and 99th gamma fluence rate percentiles as a function of the non-dimensional distance x^*, scaled by the time-averaged non-dimensional gamma fluence at $x^* = 0$ for (a) the release of Ar-41, and (b) the release of Xe-133. Lines: pollutant release height of 0.06δ (——); 0.10δ (— —); 0.14δ (— · —); 0.18δ (· · ·).

4.2.2 Comparison of the full set of simulations

The fluence rate due to the release of two noble gases released in an open field from four different altitudes is studied in this work. Hence, in total eight simulations are performed.

In order to compare the variability in gamma fluence rate observed in these simulations, the evolution of the interval widths between the 1$^{\text{st}}$ and 99$^{\text{th}}$ gamma fluence rate percentiles as a function of x^* are considered. These are shown in Fig. 4.8 for the emission of ^{41}Ar (a) and ^{133}Xe (b). For the sake of comparison, the interval widths are rescaled by the time-averaged non-dimensional gamma fluence observed at $x^* = 0$. Right below the point of emission, the interval width equals approximately 20% of the mean fluence rate observed at $x^* = 0$ for all of the cases. It is found that in all cases the width first increases, reaching a maximum at $x^* \approx 13 \ldots 17$, and decreases afterwards but at a lower rate. This may indicate that the location of the maximum spread on the measurements is invariable when expressed in terms of the emission height.

The occurrence of the maximum of the interval width is related to two competing effects. On the one hand, concentration gradients falling within the sphere of influence of the receptor, result in a variation of the fluence rate. With increasing downstream distance, a larger part of the plume falls within this sphere of influence, due to the increase in plume spread. Thus, more variation in fluence rate is observed. On the other hand, the pollutant diffusion weakens the concentration gradients with increasing downstream distance. As the plume becomes better mixed, the variation in fluence rate decreases. The competition between the increase and decrease in the variation in fluence rate with increasing downstream distance due to the first and the second effect, respectively, results in the peak observed.

In case of the high energy gamma emitted by ^{41}Ar, the maximum width is approximately twice the mean fluence rate observed at $x^* = 0$, regardless of the emission height. For low-energy gammas however, there is a clear dependence on release height as illustrated in Fig. 4.8b. For the ^{133}Xe emission from 0.06δ altitude, the maximum is approximately 1.3 while this increases up to 3.8 for the emission from 0.18δ altitude. This difference is directly attributable to the energy dependence of the linear attenuation coefficient and the buildup factor. Since high energy gammas undergo less attenuation in air compared to low energy gammas, the spatial dependence becomes more important for the latter. This effect is amplified by the energy dependence of the buildup factor.

Table 4.2: Practical example of a pollutant release from a height of 75 m at a rate of 1 MBq/s for a boundary layer with $\delta = 750$ m and $U = 22.5$ km/h at release height.

	Distance from source [m]	Mean fluence rate $[1/\text{m}^2\text{s}]$	1^{st}-to-99^{th}-percentile interval width [% of mean fluence rate]					
			30 sec	1 min	2 min	5 min	10 min	25 min
^{41}Ar	375	468	78	64	46	30	20	11
	750	482	129	99	73	47	36	21
	1500	498	153	133	104	68	54	31
	2250	466	132	119	98	70	53	34
^{133}Xe	375	1432	102	80	56	35	25	17
	750	1462	146	121	90	57	38	26
	1500	1412	159	139	109	68	49	32
	2250	1276	137	127	102	70	50	35

Finally, a practical illustration of the model applied to the dispersion of ^{41}Ar and ^{133}Xe can be found in Table 4.2. For a boundary layer with $\delta = 750$ m and $U = 22.5$ km/h at a height of 75 m, the table shows the mean fluence rate at 375 m, 750 m, 1 500 m and 2 250 m downstream from the source, measured at 1.5 m above ground level. The 1$^{\text{st}}$-to-99$^{\text{th}}$-percentile interval width are also added to the table, expressed as a fraction of the mean fluence rate, for an averaging time of 30 seconds, and 1, 2, 5, 10 and 25 minutes, respectively. The pollutant is released from 75 m altitude at a rate of 1 MBq/s and the roughness length is set to 0.01 m.

The maximum mean fluence rate is for both isotopes found between 750 m and 1 500 m from the point of release, though all values are very close together. It is observed that for an averaging time of 30 seconds, the spread of the measurements remains very large with values of the same order of magnitude as the mean fluence rate. By increasing the averaging time to 25 minutes, the spread is reduced by a factor 7. For instance at 375 m, the resulting spread for 25 minute averages is 11% and 17% of the mean fluence rate for ^{41}Ar and ^{133}Xe, compared to 78% and 102% for 30 second averages.

4.2.3 Discussion

The variability of time-averaged fluence rates when averaged over different time windows has relevance for accident scenarios. In case of an accident, e.g. during which an individual located outside is to take shelter, the dose received by the individual is the critical parameter. Thus, the local dose rate has to be integrated over time and along the trajectory of the individual. The fence monitoring systems in nuclear installations usually output time-integrated dose rate data every 10 to 20 minutes. These measurements are a good indication of the average dose rate during an emission, i.e. the typical spread on the mean remains within 10% (cf. Table 4.2 and discussion above). Thus, these measurements are, e.g., useful for estimating the source term of an unknown release. When considering the exposure of an individual during an accident however, the exposure time might be significantly shorter than the output time of the monitoring systems. It is therefore important to take the time scales of exposure, and the dominant turbulent time scales into account. The latter are primarily responsible for the variability of the fluence rate, meaning that the fluence rate is approximately constant over these periods of time. A full analysis of a detailed scenario is beyond the scope of the current thesis, but in the following, a simple order of magnitude estimation is presented to demonstrate that 10 minute average dose rates may be inaccurate for dose assessments during evacuation scenarios.

Consider an individual, located within the exclusion area, normally demarcated by a fence at distance of 300 m to 800 m around the nuclear installation [55], who must take shelter inside a building. Presuming a distance of 100 m to the nearest building, it takes the average individual about 40 s to take shelter. This is significantly shorter than the characteristic time scale of large turbulent structures in the atmospheric boundary layer. These consist of long streak-like structures with a typical length of 2 to 4 km. With a convection velocity of 10 m/s this leads to time scales in the order of 3 to 6 minutes. Since the mean variation of the plume is driven by this time scale, the instantaneous dose rate during the 40 s exposure will be nearly constant and therefore close to the average dose rate. Thus, the dose received by the individual during the exposure can deviate up to a factor of four from the mean dose, measured by the fence monitoring systems (cf. Fig. 4.8b). In general, this is true when the time required to cover the distance is short relative to the turbulent time scales. Consequently, fence monitoring data should be handled with caution when it is used to estimate the resulting dose from a short-term exposure.

In addition, it is clear that the instantaneous concentration can vary several orders of magnitude with respect to the mean, while 98% of the instantaneous gamma fluence rate observations fall approximately within a factor of two from the mean value (cf. Fig. 4.7). Even when using relatively long averaging times, the spread in concentration measurements remains large (cf. Fig. 4.5). This is particular relevant in situations of short exposure, for example during an evacuation, since these results indicate that the gamma dose measurements from nearby sensors cannot be used to accurately estimate the dose from beta radiation.

4.3 Conclusion

In the current study, a time-dependent dispersion model for the near-range dispersion of radioactive gases in a thermally neutral atmospheric boundary layer is presented. To this end, a CFD model using LES turbulence modeling is coupled with a gamma dose rate model based on the point-kernel method with buildup factors. The variability of the gamma fluence rate at ground level was assessed by performing a set of time-dependent simulations of a constant release of a radioactive gas into an open field. Four different release heights were considered in this study as well as two different isotopes, i.e. ^{41}Ar emitting a high energy gamma and ^{133}Xe emitting a low energy gamma.

The simulations demonstrated that even with the very simple set-up of the open field, a large variation in dose rate from beta radiation is observed, causing peaks in the dose rate of several orders of magnitude. Furthermore, also a strongly fluctuating gamma fluence rate with a clear lower and upper bound was observed at ground level. At a distance of approximately fifteen times the release height, the variability for both concentration and gamma fluence rate was found to be the highest, regardless of the release height or the gamma energy. Note that this observation is only valid for the current simple release geometry and neutral atmospheric stratification. For high energy gammas of ^{41}Ar, the spread on the observations is not affected by the release height while this is the case for low energy gammas of ^{133}Xe. For both cases, this spread can be reduced effectively by performing time-averaging. However, it is illustrated that neglecting this variability can result in errors up to a factor of four on the dose estimation from gamma radiation when long-term measurements are used to estimate the resulting dose from short-term exposures. In addition, the results indicate that the gamma dose measurements from nearby sensors cannot be used to accurately estimate the dose from beta radiation. This information can be particularly useful in uncertainty quantification studies and for the optimization of measurement strategies.

Chapter 5

Stable reduced-order models for pollutant dispersion

The goal of model order reduction (MOR) is to reduce the degrees of freedom (DOF) of a large size model to a very small size while maintaining the key behaviour of the model [11]. Therefore, by constructing a reduced order model (ROM) from a dispersion model based on CFD, the time-dependent pollutant dispersion can be simulated at a much reduced computational time. Extensive discussions on MOR methods are presented by Baur *et al.* [11], Lucia *et al.* [82] and Antoulas *et al.* [6]. In the following, we focus on MOR methods dedicated for sparse, linear time-invariant systems. The DOF for CFD applications is is typically in the order of 10^6 and higher. This is far beyond the practical limit for Truncated Balanced Realization and Hankel Norm Approximation methods, two frequently used MOR methods for linear, time-invariant systems [121]. Instead, Krylov-subspace projection-based MOR methods have shown to be a viable option for such systems [11, 34, 121]. Many algorithms exist for construction of the Krylov subspaces (see, e.g., Ref. [48] or Ref. [100]) but two frequently encountered algorithms are the Arnoldi method and the Lanczos method. Nour-Omid *et al.* [92] compared both methods for the solution of convection-diffusion problems in a Finite Element Method framework. They concluded that the Arnoldi is the method of choice for convection dominated problems. Other examples of the application of the Arnoldi method are presented by Woodbury *et al.* [155] with the simulation

---

The material in this chapter is published in
"Lieven Vervecken, Johan Camps, and Johan Meyers. Stable reduced-order models for pollutant dispersion in the built environment. *Building and Environment*, 92:360–367, 2015."

of the contaminant transport in an aquifer, Zhang and Woodbury [161] with a study on the contaminant transport in porous media, Willcox *et al.* [153] with the development of a ROM for turbomachinery and Wang *et al.* [151] who developed a ROM for the three-dimensional thermal analysis of microfluidic systems. The degrees of freedom in these applications were all limited to $10^3 - 10^5$, which is considerably lower than required for three-dimensional pollution-dispersion studies as considered in the current work.

We apply the Arnoldi method to the simulation of pollutant transport in a built environment. We show that the resulting ROM is guaranteed stable and suitable for faster than real-time atmospheric dispersion assessments. In addition, the algorithm for the construction of the ROM is formulated independently from the choice of CFD solver, such that it is applicable to both open-source and commercial CFD software packages. The effectiveness of the ROM is demonstrated based on a simulation of a time-dependent pollutant release at the Doel Nuclear Power Station, comparing the ROM results to the high-resolution CFD.

This chapter is further organized as follows. First, in Section 5.1, we present the model order reduction methodology and the pollutant dispersion model. Next, in Section 5.2 we detail the simulation cases considered in the current work and the numerical set-up of our simulations. Simulation results are discussed in Section 5.3. Finally, conclusions are presented in Section 5.4.

5.1 Methodology

In the current section we briefly introduce the continuous and discrete formulation of the pollutant dispersion model in §5.1.1. Next, the construction of the ROM is presented in §5.1.2.

5.1.1 Pollutant dispersion model

Consider the three-dimensional dispersion of a non-buoyant, non-reactive gas in a steady, thermally neutral boundary layer, for a constant wind direction, and known site geometry. In this situation, the three-dimensional velocity field $\langle \boldsymbol{u} \rangle(\boldsymbol{x})$ can be obtained from a standard CFD model, e.g., either based on RANS simulations or LESs (for practical details, cf. §5.2.2). The dispersion is then further modeled through Eq. (2.12).

Spatial discretization of Eq. (2.12), e.g., using a finite-volume approach, results in a large coupled system of ordinary differential equations. This system can be written as

$$\frac{\mathrm{d}\tilde{c}}{\mathrm{d}t} = A\tilde{c} + bs \tag{5.1}$$

where $\tilde{c}(t) \in \mathbb{R}^n$ is the solution vector containing the concentration of every cell in the domain, $b \in \mathbb{R}^n$ is the source vector containing the contribution of every cell to the pollutant source and $s(t)$ is the source magnitude input. In addition, the sparse matrix $A \in \mathbb{R}^{n\times n}$ is the discrete representation of the advection and the diffusion operator, including the spatial boundary conditions. When set up properly, this matrix is negative-definite. Note that in practice, this matrix is not explicitly available, but indirectly coded in the CFD software used to solve Eq. (2.12).

Often, the interest is not in obtaining the pollutant concentration over the whole domain, but e.g. in the concentration or the health impact at a limited number of locations [117, 149]. Therefore, an output vector y can be defined as

$$y = C\tilde{c} \tag{5.2}$$

where $C \in \mathbb{R}^{m\times n}$, the output matrix, contains the contribution of every cell to the requested m outputs.

5.1.2 Reduced-order model

The purpose of MOR is to obtain a model of significantly reduced order ($r \ll n$) which, in a certain way, behaves similar to the original full size model [82]. In this view, let $V \in \mathbb{R}^{n\times r}$ be a matrix whose columns form an orthonormal basis of a r-dimensional subspace. Projection of the solution vector c onto this basis can be identified by the approximation $\tilde{c} \approx Vc_r$ where c_r is the reduced-order solution vector. Substitution of this approximation in the system of Eq. (5.1) followed by a Petrov–Galerkin projection using any full-rank matrix $W \in \mathbb{R}^{n\times r}$ results in the reduced order system (see, e.g., Ref. [11] or Ref. [48])

$$W^TV\frac{\mathrm{d}c_r}{\mathrm{d}t} = W^TAVc_r + W^Tbs \tag{5.3}$$

where $A_r = W^TAV \in \mathbb{R}^{r\times r}$ is in general a full matrix, i.e. the sparsity of A is usually lost through the projection, and $B_r = W^Tb \in \mathbb{R}^{r\times 1}$. This equation can be fully solved in the reduced-order space with dimension r. Once $c_r(t)$ is obtained, the fine-scale solution can be reconstructed using $\tilde{c} \approx Vc_r$. As a result, the output vector can be approximated as

$$y \approx CVc_r \tag{5.4}$$

where $C_r = CV \in \mathbb{R}^{m\times r}$.

Algorithm 1 One-sided Arnoldi algorithm to construct a basis of $\mathcal{K}_r(A^{-1}, A^{-1}b)$.

```
1. Initialize:
    (a) Solve for $\tilde{v}_1^{\dagger}$: $A\tilde{v}_1 = b$
    (b) Set: $v_1 = \frac{\tilde{v}_1}{\|\tilde{v}_1\|}$
2. For $i = 2 \dots r$ do:
    (a) Solve for $\tilde{v}_i^{\dagger}$: A $\tilde{v}_i = v_{i-1}$
    (b) Orthogonalize $\tilde{v}_i$: for $j = 1 \dots i-1$
        $h = \tilde{v}_i v_j$
        $\tilde{v}_i = \tilde{v}_i - h v_j$
    (c) Normalize: $v_i = \frac{\tilde{v}_i}{\|\tilde{v}_i\|}$
3. Set $V = [v_1 v_2 \dots v_r]$
4. Construct $A_r = V^T A V$
```

† This step can be performed using the CFD package by imposing b or v_{i-1} as source vector in Eq. (5.1) and solving for the steady state solution.

In this work, we construct the projection matrix V as a basis of the r-th order Krylov subspace in order to provide the moment matching property [102]. The Krylov subspace of order r is defined by

$$\mathcal{K}_r(\tilde{A}, \tilde{b}) = span\{\tilde{b}, \tilde{A}\tilde{b}, \tilde{A}^2\tilde{b}, \dots, \tilde{A}^{r-1}\tilde{b}\} \tag{5.5}$$

where $\tilde{A}$ is a constant matrix and $\tilde{b}$ is referred to as the starting vector. In order to match the lower part of the frequency domain, we set $\tilde{A} = A^{-1}$ and $\tilde{b} = A^{-1}b$ [116]. In this way, the slow dynamics of the system, i.e. in the order of the main convection time scales, are matched well.

The one-sided Arnoldi method is employed to construct V the basis. By opting for a one-sided method, which implies that $W = V$ and $W^T V = I$ in Eq. (5.3), the first r moments of the original and the reduced system transfer functions match [102]. The modified Gram-Schmidt implementation of this method is elaborated in Algorithm 1 for a single-input system [81]. The algorithm generates a vector v_i which results from the recursive orthogonalization of the vector $A^{-1}v_{i-1}$ with respect to the previously generated orthonormal vectors. In order to avoid computing the inverse of the matrix A, the linear system $A\tilde{v}_i = v_{i-1}$ is solved to obtain $\tilde{v}_i$. In this way, only r linear systems need to be solved instead of n systems required to compute the inverse. This algorithm

Algorithm 2 One-sided Arnoldi algorithm to construct a basis of $\mathcal{K}_r(A^{-1}, A^{-1}b)$.

```
1. Initialize:
    (a) Solve for $\tilde{v}_1^\dagger$: $A\tilde{v}_1 = b$
    (b) Set: $v_1 = \frac{\tilde{v}_1}{\|\tilde{v}_1\|}$ and $x_1 = \frac{b}{\|\tilde{v}_1\|}$
2. For $i = 2 \ldots r$ do:
    (a) Solve for $\tilde{v}_i^\dagger$: $A\tilde{v}_i = v_{i-1}$
    (b) Set: $\tilde{x}_i = v_{i-1}$
    (c) Orhogonalize $\tilde{v}_i$, and adapt $\tilde{x}_i$: for $j = 1 \ldots i-1$
        $h = \tilde{v}_i v_j$
        $\tilde{v}_i = \tilde{v}_i - h v_j$
        $\tilde{x}_i = \tilde{x}_i - h x_j$
    (d) Normalize: $v_i = \frac{\tilde{v}_i}{\|\tilde{v}_i\|}$ and $x_i = \frac{\tilde{x}_i}{\|\tilde{v}_i\|}$
3. Set: $V = [v_1 \; v_2 \; \ldots \; v_r]$ and $X = [x_1 \; x_2 \; \ldots \; x_r]$
4. Construct: $A_r (= V^T A V) = V^T X$
```

† This step is performed using the CFD package by imposing b or v_{i-1} as source vector in Eq. (5.1) and solving for the steady state solution.

can be readily extended towards multiple input systems (see, e.g., Ref. [48] or Ref. [116]).

The A-matrix in Eq. (5.1) is often not, or only partly, accessible within the CFD package. This can be due to restricted access to the source code, or due to the solution methodology employed by the software package. The latter is for instance the case in OpenFOAM where non-orthogonality in the mesh is accounted for by adding additional source terms to the right-hand side of Eq. (5.1) instead of increasing the bandwidth of the solution matrix. Thus, if A is not explicitly available, it becomes impossible to directly perform step 4 in Algorithm 1. In order to deal with this, we reformulate the one-sided Arnoldi algorithm in terms of an unknown matrix (A). This results in the introduction of $X \in \mathbb{R}^{n \times r}$ which accounts for the unknown contribution of A to the reduced matrix A_r before the Galerkin projection. The revised algorithm is elaborated in Algorithm 2. The basis V produced by this algorithm and the corresponding reduced matrix A_r are identical to those produced by the classical Arnoldi algorithm. The equivalence the of basis V is readily seen, since the introduction of X in Algorithm 2 does not affect the construction of

V. Thus, Algorithm 2 reduces to Algorithm 1 for the construction of V. The proof that, for any order r, $X^{(r)} = AV^{(r)}$ can be constructed by induction. Here, we use superscript (r) to denote the order of the constructed model. In Algorithm 2, these superscripts are omitted for sake of brevity.

Base case: when $r = 1$, $V^1 = A^{-1}b/\|\tilde{v}_1\|$ and $X^1 = b/\|\tilde{v}_1\|$ by construction. Hence, $AV^1 = X^1$.

Induction hypothesis: Assume that $AV^{(r-1)} = X^{(r-1)}$ holds for some positive integer r.

Inductive step: We now show that using Algorithm 2, $AV^{(r)} = X^{(r)}$. We have

$$AV^{(r)} = \begin{bmatrix} AV^{(r-1)} & Av_r \end{bmatrix} \tag{5.6}$$

$$= \begin{bmatrix} X^{(r-1)} & Av_r \end{bmatrix} \quad \text{(by induction hypothesis)} \tag{5.7}$$

We further need to show that $Av_r = x_r$. Therefore, we start from writing the orthogonalization of $\tilde{v}_r$ to v_r in Algorithm 2 as

$$v_r = \alpha\tilde{v}_r - [h_1\ h_2\ \ldots\ h_{r-1}]V^{(r-1)} \tag{5.8}$$

Left-multiplying with matrix A gives

$$Av_r = A\left(\alpha\tilde{v}_r - [h_1\ h_2\ \ldots\ h_{r-1}]V^{(r-1)}\right) \tag{5.9}$$

$$= \alpha A\tilde{v}_r - [h_1\ h_2\ \ldots\ h_{r-1}]AV^{(r-1)} \tag{5.10}$$

$$= \alpha\tilde{x}_r - [h_1\ h_2\ \ldots\ h_{r-1}]X^{(r-1)} \tag{5.11}$$

$$= x_r \quad \text{(by construction)} \tag{5.12}$$

where we use $A\tilde{v}_i = \tilde{x}_i$, as defined in Algorithm 2. Thus $AV^{(r)} = X^{(r)}$ for any order r. Note that solving $A\tilde{v}_i = v_{i-1}$ for $\tilde{v}_i$ in Algorithm 2 does not require the knowledge of A. This can be achieved by using the CFD package as a black box while imposing v_{i-1} as source vector in Eq. (5.1) and solving for the steady state solution.

Alternatively, a two-sided method, where $W \neq V$, can be used which matches $2r$ moments (see, e.g., Ref. [115] or Ref. [103]). Clearly, a ROM constructed from a two-sided method has the potential of resulting in a better approximation with respect to a one-sided method because of the higher number of matching moments. However, we observed that a two-sided method was not likely to result in a stable ROM, and the use of additional stabilization methods would be essential (see, e.g., Ref. [69] or Ref. [3]). In contrast to this, by taking $W = V$ the definiteness of the original A matrix was preserved in all cases studied, i.e. the projection of the stable system always resulted in a stable reduced-order model. This is also found by Silveira *et al.* [125] and Willcox *et al.* [153]. Nevertheless, if necessary, the stabilization methods can also be applied in combination with the one-sided method.

5.2 Case set-up

First, we detail the site considered in the current work in §5.2.1. Next, the computational set-up used to solve the dispersion problem for both the CFD model and to set up the ROM are elaborated in §5.2.2.

5.2.1 Case description

A time-dependent pollutant release at the Doel nuclear power station, emitted from the chimney of Doel 3, is the subject of the present study. The geometry of the case studied is shown in Fig. 5.1. Pollutant iso-contours of a simulation result at four different time instances are also shown in the figure (cf. below for further details). The nuclear power station includes four cylindrical reactor buildings, two hyperbolic cooling towers with a height of 176 m, and a number of cuboid auxiliary buildings. A uniform roughness length $z_0 = 0.01\text{m}$, corresponding to short grassland, is set for free ground surface. Two different wind directions are considered in this study, i.e. wind coming from the southwest, which is the prevailing wind direction for this location, and wind coming from the west. For both situations, the friction velocity is set to 0.25 ms^{-1}. This corresponds to a wind speed of 20 km h^{-1} at 74 m altitude, the height of the chimney of Doel 3.

The coordinate system is chosen such that the coordinate of the source corresponds to $(0, 0, 74\text{m})$ and that the x-axis is in the streamwise direction. The release of the pollutant is simulated as a Gaussian function in time

$$S_p(t) = a \exp\left(\frac{(t - t_s)^2}{2\tau_i^2}\right) \tag{5.13}$$

where we set the time of peak emission rate $t_s = 5\tau_i$ and $a = (\tau_i\sqrt{2\pi})^{-1}$ to attain $S_p(0) \simeq 0$ and $\int_0^\infty S_p(t')dt' = 1$. In this work, we choose the time constant $\tau_i = L/U$ based on a length scale and the wind speed at this height according to the logarithmic velocity profile. Three length scales are considered, i.e. the chimney height, the cooling tower height and the domain height. The

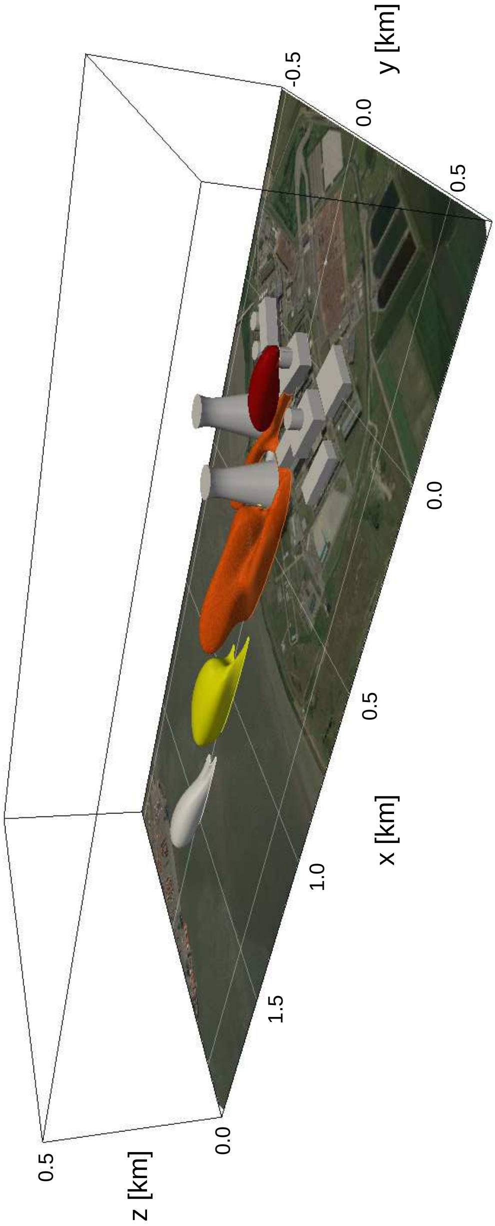

Figure 5.1: Computational domain. In color, isosurface for the instantaneous concentration $c^* = 2.5 \times 10^{-3}$ ($= cUL^2/R$) for case τ_1 at time $t^* = 5$ (red); $t^* = 15$ (orange); $t^* = 25$ (yellow); $t^* = 35$ (white).

Table 5.1: Overview of the length scale, wind speed, dimensional time constant and non-dimensional time constant of the three cases simulated.

	L [m]	U [m/s]	τ_i [s]	τ^* [-]
case τ_1	74	5.568	13.290	1.000
case τ_2	176	6.110	28.806	2.168
case τ_3	500	6.762	73.939	5.564

corresponding wind speed and time scales are summarized in Table 5.1. These different scales allow us to evaluate the performance of the ROM for a range of relevant emission scales.

In order to assess the quality of the ROM with respect to the CFD model, two performance measures are used, i.e., the fractional bias (FB) and the normalized mean square error (NMSE) [30, 148]:

$$\text{FB} = 2\frac{\sum\left(c^*_{ROM} - c^*_{CFD}\right)}{\sum\left(c^*_{ROM} + c^*_{CFD}\right)}, \tag{5.14}$$

$$\text{NMSE} = n\frac{\sum\left(c^*_{ROM} - c^*_{CFD}\right)^2}{\sum c^*_{ROM}\sum c^*_{CFD}}. \tag{5.15}$$

It is readily seen that a perfect ROM would yield in FB and NMSE $= 0$. All cells in the whole domain are taken into account for the evaluation of these measures following a paired in space-and-time approach.

Finally, the concentration reported in the current study is normalized as $c^* = cUL^2/R$ where R is the total amount of pollutant released, L is the height of the chimney and U is the mean wind speed at height L according to the logarithmic velocity profile. Furthermore, distance and time are normalized as $x^* = xL^{-1}$ and $t^* = (t - t_s)UL^{-1}$, respectively.

5.2.2 Computational set-up

The transport equations (2.12) are spatially discretized using second-order schemes on a hexahedral mesh consisting of 8.0 M cells and 10.0 M cells for wind coming from the southwest and the west, respectively. The domain dimensions and the grid resolution are based on the recomendations of the COST 732 and AIJ guidelines [47, 138]. Simulation of the full-size convection-diffusion model is performed using the OpenFOAM finite-volume open-source simulation platform. In a first step the steady velocity field, and the eddy viscosity are solved. To that end, the Reynolds-averaged Navier–Stokes (RANS) equations are solved with OpenFOAM. Closure is provided by the standard $k - \epsilon$ model [79] in which the model coefficients are chosen in accordance with Richards and Hoxey [108], and also the boundary conditions for the velocity field simulation are set in accordance with Richards and Hoxey [108]. The boundary conditions for the convection-diffusion equation are set to zero at the inlet and Neumann boundary conditions are applied at the other boundaries.

For the implementation of the Arnoldi algorithm and the simulation of the ROM, we use the Petsc library [7, 8, 9]. The order of the ROM is set to 100, but for evaluation of accuracy, we also evaluate reduced-order models with degrees of freedom ranging from 10 up to 150. For the CFD model as well as for the ROM, a second-order Crank-Nicholson scheme is applied for time discretization with a time step $\Delta t^* = 10^{-3}$. The simulations of the full-size model were carried out on 40 processors distributed over two nodes, installed with Intel Xeon E5-2680 v2 processors and interconnected through DDR infiniband. The preconditioned bi-conjugate gradient solver using diagonal incomplete-LU preconditioning is used as linear system solver with a tolerance set to 10^{-16}. The simulations of the ROM were carried out on the same machine using only one processor core.

5.3 Results and discussion

The results of the cases studied are presented in this section by comparing the results of the full CFD model with the ROM. First, in §5.3.1, the results of the simulation of case τ_1 with wind coming from the southwest are presented in detail. In addition, it is illustrated that similar results are obtained with wind coming from the west, and for cases τ_2 and τ_3. Subsequently, in §5.3.2, the obtained reduction in time and computational cost is discussed.

5.3.1 Simulation results

The dispersion case τ_1 with wind coming from the southwest is used to discuss the general simulation results. We focus the discussion on the concentration at ground level (1 m height) since this is usually of interest in health impact studies (see, e.g., Ref. [30], Ref. [31] and Ref. [149]). The contours of the non-dimensional concentration at ground level are shown in Fig. 5.2 at $t^* = 5$, 10, 15 and 20 for both the CFD model and the ROM. It is observed that the solution of both models is nearly identical. At $t^* = 5$, all pollutants are emitted and the plume is advected towards the cooling tower where it splits into two parts. A small part of the plume passes in between the two cooling towers but the major part of the plume passes the cooling tower from the outer side. The maximum concentration at ground level increases to $c^* = 0.0243$ at $t^* = 10$ which is found by both models. Afterwards, the concentration steadily decreases with time as a result of turbulent mixing. This illustrates that, notwithstanding the splitting of the plume, the ROM is well capable of reconstructing both the shape and the magnitude of the pollutant concentration.

Fig. 5.3 shows the evolution of the non-dimensional concentration at $t^* = 10$ for cases τ_1, τ_2 and τ_3 from the point of release along the stream-wise direction (Fig. 5.3a, Fig. 5.3c) and along span-wise direction at $x^* = 7.5$ (Fig. 5.3b, Fig. 5.3d) for wind coming from the southwest and the west, respectively. In these graphs, the lines represent the CFD model while the symbols represent the ROM. The interruptions in the curves between $x^* = 0 \ldots 1$ and $x^* = 3.5 \ldots 5.5$ in Fig. 5.3a, and $x^* = 0 \ldots 2.5$ in Fig. 5.3c are due to the presence of buildings and a cooling tower.

Three distinct concentration profiles are found in stream-wise direction for wind coming from the southwest (Fig. 5.3a). While the stream-wise concentration for case τ_1 shows multiple peaks, the concentration for case τ_3 is rather smooth. Regardless these differences, the ROM is clearly well capable of reproducing these profiles. In span-wise direction (Fig. 5.3b), a nearly identical span-wise spread of the concentration is found for all three cases but the shape and the magnitude of the profiles are again different. The maximal concentration is found near the centerline although a second peak is found near $x^* \approx 1$ for case τ_1. Note that around $y^* = -2.5 \ldots -0.5$, the concentration is also slightly increased due to the part of the plume passing in between the two cooling towers. Again, the profiles predicted by the ROM are indistinguishable from these of the CFD model. The difference between the concentration profiles predicted by the ROM and the CFD model is also negligible for the cases with wind coming from the west. In stream-wise direction (Fig. 5.3c), the profiles are approximately bell-curved with a maximum at $x^* \approx 8$ for all three cases. Looking at span-wise direction (Fig. 5.3d), the concentration profiles are strongly asymmetric but the shape is similar for each of the cases.

In Fig. 5.4, the effect of changing the order of the ROM on the simulated time evolution of the non-dimensional concentration is shown, observed at ground level at $x^* = 10$ downwind from the pollutant source ($y^* = 0$), as a function of the non-dimensional time t^* for case τ_1 with wind coming from the southwest. Four different orders are considered, i.e. 25, 50, 75 and 100. It is observed that a ROM of order 25 shows large concentration fluctuations prior to the concentration peak at $t^* = 10 \ldots 15$. In addition, a significantly deviating concentration peak is found. Clearly, a ROM order of 25 is insufficient to reconstruct the concentration profile properly. Increasing the order of the ROM

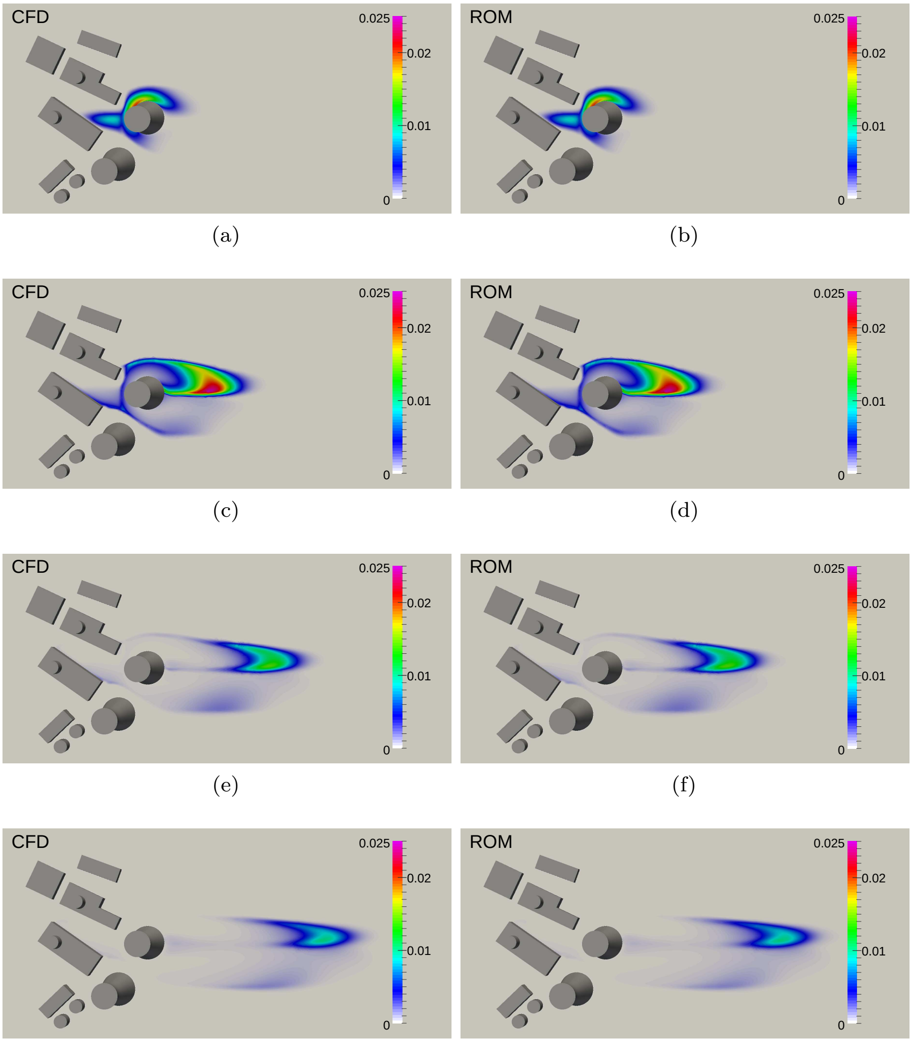

(a) (b)

(c) (d)

(e) (f)

(g) (h)

Figure 5.2: Contours of the non-dimensional concentration c^* $(= cUL^2/R)$ observed at ground level (1 m) for case τ_1; (a, b) $t^* = 5$ $(= (t - t_s)U/L)$, (c, d) $t^* = 10$, (e, f) $t^* = 15$, (g, h) $t^* = 20$.

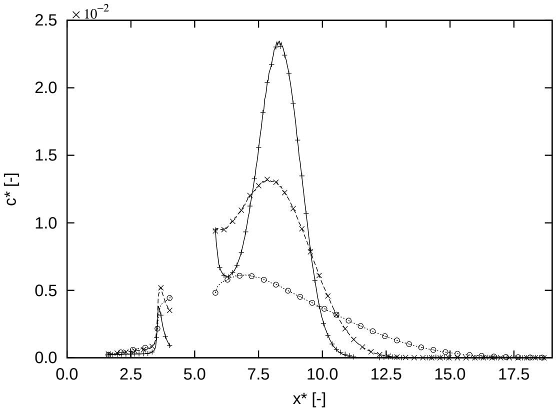
× 10⁻²
2.5
2.0
1.5
1.0
0.5
0.0
c* [-]
0.0
2.5
5.0
7.5
10.0
12.5
15.0
17.5
x* [-]

(a)

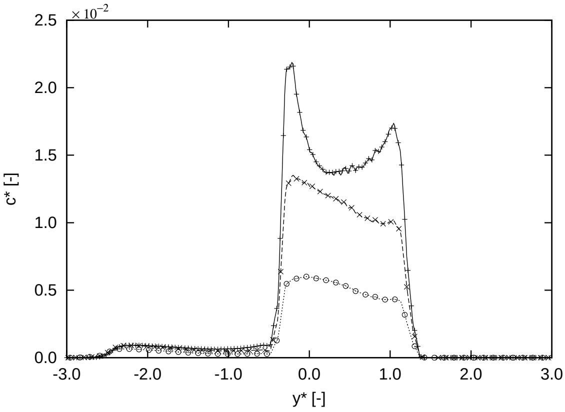
× 10⁻²
2.5
2.0
1.5
1.0
0.5
0.0
c* [-]
-3.0
-2.0
-1.0
0.0
1.0
2.0
3.0
y* [-]

(b)

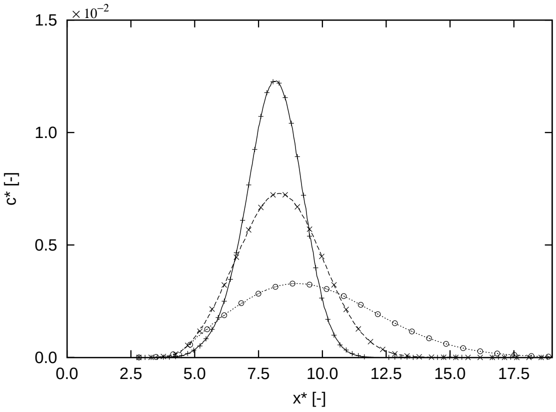
× 10⁻²
1.5
1.0
0.5
0.0
c* [-]
0.0
2.5
5.0
7.5
10.0
12.5
15.0
17.5
x* [-]

(c)

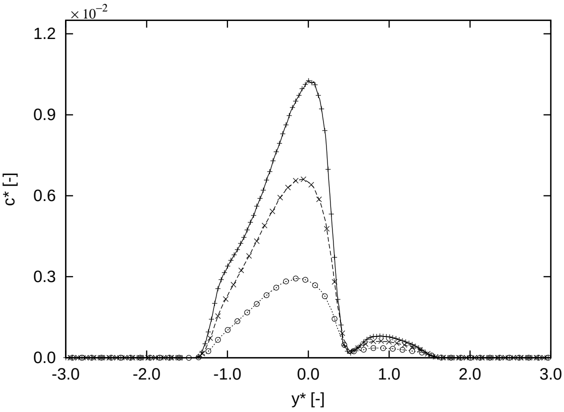

(d)

Figure 5.3: Profiles of the observed non-dimensional concentration c^* ($= cUL^2/R$) observed at ground level (1 m) at $t^* = 10$ ($= (t - t_s)U/L$). For wind coming from the southwest: (a) c^* along stream-wise direction at $y^* = 0$ ($= y/L$), (b) c^* along span-wise direction at $x^* = 7.5$ ($= x/L$). For wind coming from the west: (c) c^* along stream-wise direction at $y^* = 0$ ($= y/L$), (d) c^* along span-wise direction at $x^* = 7.5$ ($= x/L$). Symbols: (+): c^*_{ROM} case τ_1; (×): c^*_{ROM} case τ_2; ($\odot$): c^*_{ROM} case τ_3. Lines: (—): c^*_{CFD} case τ_1; (−−) c^*_{CFD} case τ_2; ($\cdots$) c^*_{CFD} case τ_3.

up to 75 steadily decreases both the concentration fluctuations prior to, and the deviation of, the concentration peak. At an order of 100, no concentration fluctuations are found and the concentration peak shows very little change with the profile of order 75. For this case, a ROM of order 100 is therefore sufficient for reproducing the concentration profile accurately.

In Fig. 5.5, the evolution of the absolute value of FB and the NMSE are shown as function of the order r of the ROM for case τ_1 with wind coming from the southwest at $t^* = 5$, $t^* = 15$ and $t^* = 25$. First of all, it is observed that increasing the order of the ROM improves its accuracy. It is observed that the FB roughly decreases with a reduction rate of one order of magnitude for every addition of 30 to 40 modes. The NMSE decreases more smoothly than FB. For time $t^* = 5$, the decrease of the NMSE is more than exponential up to $r \approx 120$ after which it stagnates. For $t^* = 15$ and $t^* = 25$ a nearly perfect exponential decrease is found at a reduction rate of one order of magnitude for every addition of approximately 20 modes.

Finally, the application of the ROM to the dispersion of radioactive gases is illustrated in Fig. 5.6. This graph shows the time evolution of the gamma

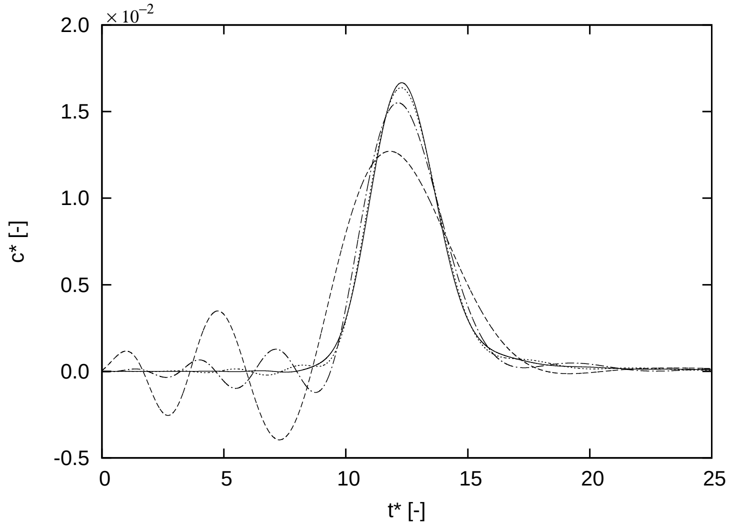

Figure 5.4: Profiles of the observed non-dimensional concentration c^* ($= cUL^2/R$) observed at ground level (1 m) at $x^* = 10$ ($= x/L$) and $y^* = 0$ ($= y/L$) as function of time t^* ($= (t - t_s)U/L$). Lines: (−−): $r = 25$; (− · −): $r = 50$; (· · ·): $r = 75$; (—): $r = 100$.

fluence rate and the total gamma fluence received for a release of ^{133}Xe, assuming the emission profile of case τ_1. At $x^* = 10$ downwind from the pollutant source ($y^* = 0$) at ground level (Fig. 5.6a), the dose rate increases monotonically up to $t^* \approx 17$ and monotonically decreases afterwards. This profile is significantly different from the observation at $x^* = 3$ and $y^* = 4$, shown in Fig. 5.6b. The influence of the buildings, including building shielding, results in a strongly distorted profile with multiple peaks.

5.3.2 Discussion

CFD is known to be prohibitively expensive with regards to its use for real-time purposes. This is also observed in the current study. Despite the use of 40 CPUs, it still takes 97 s to simulate one second of real time using the CFD model. This is reduced by more than a factor of 2500 to only 38.6 ms per second of real time when the dispersion is simulated using the ROM. In other words, the model runs 25 times faster than real-time. In §5.3.1, it is demonstrated that this is without a significant loss in accuracy. When the computational cost is taken into account, i.e. only 1 core is used to for the

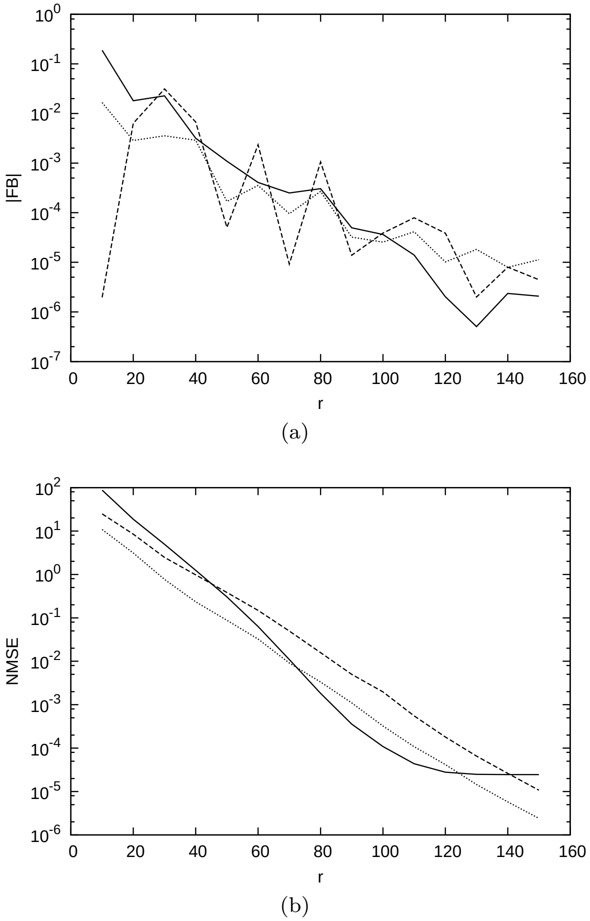

(a)

(b)

Figure 5.5: Performance measures for τ_1 at three time instances. (a) Absolute value of FB, (b) NMSE. Lines: (—): $t^* = 5$; (−−): $t^* = 15$; $(\cdots)$: $t^* = 25$.

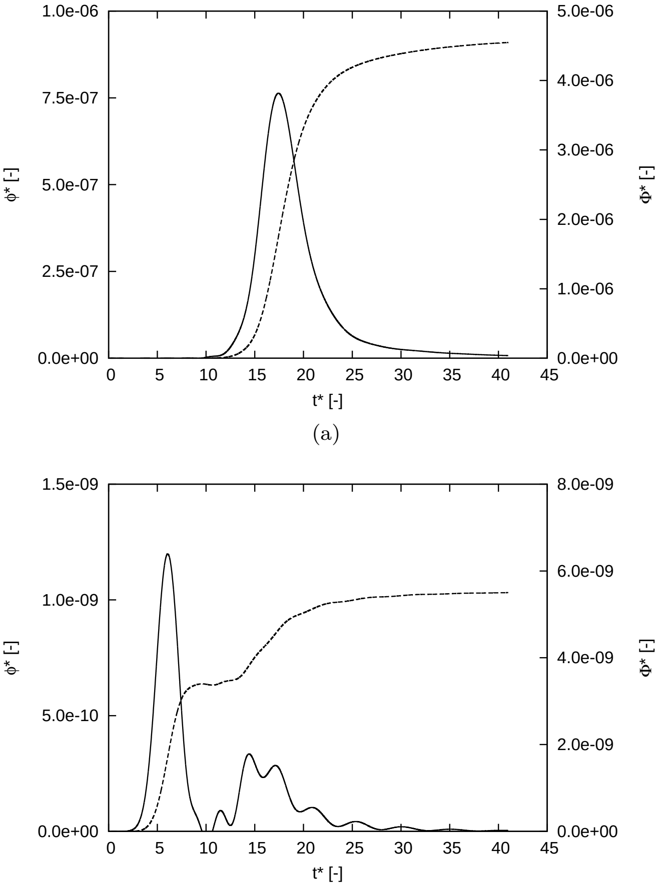

(a)

(b)

Figure 5.6: Profiles of the observed non-dimensional gamma fluence rate ϕ^* ($= \phi L^2/R$) and gamma fluence $\Phi^* = \int_0^{t^*} \phi^*(t')dt'$ as function of time t^* ($= (t - t_s)U/L$) observed at ground level (1 m) at (a) $x^* = 10$ ($= x/L$) and $y^* = 0$ ($= y/L$); (b) $x^* = 3$ and $y^* = 4$. Lines: (–): ϕ^*; (−−): Φ^*.

ROM, the reduction is more than a factor of 10^5. Furthermore, subsequently performing the dose assessment has a negligible effect on the simulation time of the ROM. It is therefore clear that the ROM enables for fast dose assessment after the emission of a radioactive gas.

The construction of the ROM introduces a one-time initialization cost. The bulk of the computational cost is in solving the linear equation $A\tilde{v}_i = v_{i-1}$ using the CFD solver. For each of the r vectors, this is done iteratively using false time-stepping as under-relaxation and requires approximately 720 s. A memory space of $2r \times n$ is required to store both V and X but this can be freed again after the construction of the ROM. Once set up, the ROM only requires a negligible memory space of r^2, r and $m \times r$ for A_r, B_r and C_r, respectively.

For performing repeated simulations such as in an on-line monitoring context, the advantage of the ROM over the CFD model is clear. However, also for one simulation only the use of the ROM can be interesting. The initialization of one mode of the ROM requires approximately 720 s. The simulation of 1 second of real time requires 97 seconds with the CFD model. Therefore, the time required for the initialization of a ROM with 100 modes equals the simulation of approximately 740 seconds of real time with CFD. Thus, once longer run times are required, it may become interesting to first construct the ROM, and then use it instead for the simulation.

5.4 Conclusion

In the current study, a reduced order modeling method is introduced which allows to simulate the dispersion of a pollutant in a built environment faster than real-time. To this end, a Krylov-subspace projection-based model reduction method using the Arnoldi algorithm is applied for a CFD model. The method results in a stable ROM, and the algorithm is formulated in such a way that it can be used with any choice of CFD solver. We simulate the pollutant dispersion using an Eulerian approach where the concentration is formulated as a transient three-dimensional advection-diffusion problem on a steady velocity background.

To assess the approach, three cases of a time-dependent pollutant emission are simulated using both the CFD and the ROM. The Doel Nuclear Power Station was selected as the subject of the study. The simulations show that for all of the cases, the ROM is well capable of reconstructing both the shape and the magnitude of the pollutant concentration without significant loss in accuracy. In addition, it is illustrated that increasing the order of the ROM, further increases the accuracy, i.e. the ROM converges towards the CFD model. After initialization, the application of this method resulted in the reduction of the computational time by a factor of 2500, running 25 times faster than real-time, including a possible dose assessment. Furthermore, when the computational cost is looked at, the reduction was more than a factor of 10^5. It is therefore clear that the ROM enables for fast dose assessment after the emission of a radioactive gas.

In the current chapter, a ROM is constructed for the forward modeling of the dispersion of a non-buoyant, non-reactive gas in a steady, thermally neutral boundary layer. However, the approach can also be applied in an inverse modeling context for direct source term estimation from measurements. This is further elaborated in chapter 6.

Chapter 6

Fast source reconstruction from near-range measurements

In the event of the release of a chemical, biological or radiological pollutant into the atmosphere, a fast and accurate estimation of the pollutant dispersion is vital for the initial emergency assessment [112, 126]. In case the source location and size are known, atmospheric dispersion models can predict the impact of the pollutant on the surroundings (cf. Chapter 3, 4, and 5). Because of their predictive nature, these models are often referred to as forward models [112]. In most cases however, the source is not known a priory and the emergency response is triggered after the detection of a pollutant by monitoring systems. Therefore, the fast reconstruction of the pollutant source using measurements is essential for a proper emergency response [112, 123, 126].

Much attention has been devoted to address the inverse modeling challenge, i.e. the reconstruction of the pollutant source based on measurements. The problems reported in the literature range from single point sources [72, 123] to multiple point sources [44, 124, 126, 150, 159], and from steady state releases [2, 112, 126] to transient releases [161, 2, 57]. In general, the inverse modeling

---

The material in this chapter is submitted for publication in
“Lieven Vervecken, Johan Camps, and Johan Meyers. Multi-source reconstruction of near-range atmospheric dispersion using a one-shot optimisation approach. *Boundary-Layer Meteorology*, submitted for publication.”

methods can be categorized into probabilistic and optimization methods [162, 146]. The former focus on reconstructing probabilities of the source parameters. These techniques are often based on Bayesian inference [33, 72, 150, 159] and Markov chain Monte Carlo sampling [33, 57], although other methods such as the minimum relative entropy method used by Ma *et al.* [84] are also found. However, due to the need for prior information and expensive computational requirements, probabilistic methods are less applicable in emergency situations [126]. With the optimization approach, the source parameters are chosen such that a predefined objective, e.g. the error between simulation and measurements, is minimized [2, 74, 83, 126].

Each of these methods usually requires many iterations, i.e. the forward and/or backward model needs to be solved multiple times [112]. As a result, applying these methods to a full size three-dimensional dispersion model using CFD is computationally too expensive for practical applications such as fast source estimation [91, 84]. For such applications, the near-range dispersion remains therefore often modeled using Gaussian-based plume models or other simplified models (see, e.g. Ref. [83, 84, 113]). This unavoidably results in a loss of accuracy.

In the current chapter, we propose a fast and accurate method for the reconstruction of transient, multi-source emissions based on CFD modeling and near-range measurements. The problem is formulated as a least squares problem, comparing the time-dependent measurements to model prediction. Since this type of problems tends to be ill-conditioned [44, 126], regularization is added to improve the solvability. The optimization is constrained by the forward dispersion model which is given by the transient three-dimensional advection-diffusion problem on a steady three-dimensional velocity background. First-order optimality conditions are derived from the Lagrangian for this problem. By limiting the possible sources to a finite number of possibilities, a Krylov-subspace projection-based model reduction method using the Arnoldi algorithm (cf. Chapter 5) can be applied to each of the derived conditions. As a result, the degrees of freedom (DOF) of the problem are reduced to such extent that the optimal solution can be solved in one shot from the optimality conditions. We test the methodology using three case studies. Because concentration measurements corresponding to multiple emissions are scarce, we generate a series of virtual measurements at the Doel Nuclear Power Station using the full CFD model. By adding synthetic noise to the measurements, the robustness of the method is examined.

This chapter is further organized as follows. First, in section 6.1, the optimization problem is defined and the optimality condition is derived. Next, in section 6.2, we present the model order reduction methodology employed to reduce the size of the optimization problem. We detail the three source

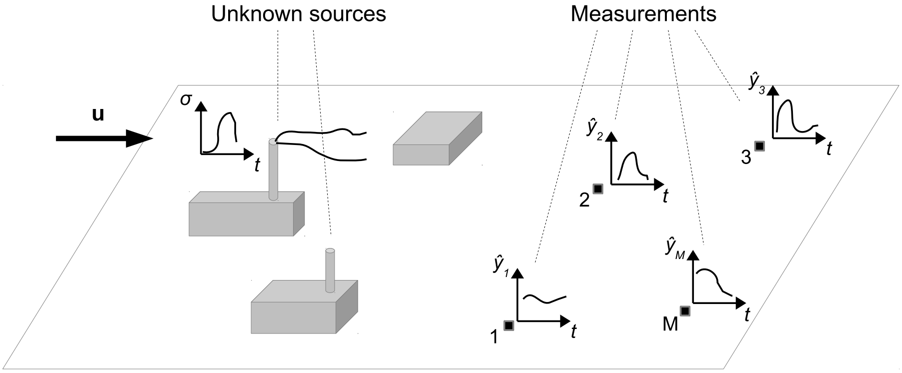

Figure 6.1: Graphical representation of a typical source reconstruction problem.

reconstruction cases considered in the current work and the numerical set-up of our simulations in section 6.3. The simulation results are discussed in section 6.4, followed by the conclusions in section 6.5.

6.1 Methodology

Given a series of measurements $\hat{\boldsymbol{y}}(t) = [\hat{y}_1(t)\ \hat{y}_2(t)\ \dots\ \hat{y}_M(t)]$ in time at M different locations $\boldsymbol{x}_i$, the aim is to determine the spatial and temporal distribution of the pollutant source $\sigma(\boldsymbol{x}, t)$ that most closely reproduces the measurements (cf. Fig. 6.1 for a graphical representation). The measurements can either be the local concentrations or a derived quantity such as radiological dose rates. We formulate the source identification problem as a regularized, least squares problem. To that end, the cost functional $\mathcal{J}$ is defined as

$$\mathcal{J}(c, \sigma, \boldsymbol{y}) = \frac{1}{2} \sum_{i=1}^{M} \int_0^T (y_i - \hat{y}_i)^2 \, d\Omega dt + \frac{\beta}{2} \int_0^T \int_\Omega \sigma^2 d\Omega dt + \frac{\gamma}{2} \int_0^T \int_\Omega \left(\frac{\partial \sigma}{\partial t} \right)^2 d\Omega dt, \quad (6.1)$$

where $\boldsymbol{y}(t) = [y_1(t)\ y_2(t)\ \dots\ y_M(t)]$ are the reconstructed measurements, Ω is the physical domain, and T is the measurement time horizon. The first term represents the L_2-norm of the error between measurements and reconstructed measurements given the estimated source. Regularization is added to the cost functional in the second and the third term. They penalize the non-compactness of σ, and the magnitude of the rate of change of σ in order to obtain a well-posed problem (see, e.g., Ref. [2] for a discussion). In the current work, the regularization strength is controlled by parameters $\beta = 5 \cdot 10^{-12}$ and $\gamma = 100\beta$ (see Section 6.4 for the motivation of this choice).

The optimization problem is subject to the forward relation between the sources and the measurements. Consider the three-dimensional dispersion of a non-buoyant, non-reactive gas in a steady, thermally neutral boundary layer. For a given wind direction and known site geometry, the three-dimensional mean velocity field $\langle \boldsymbol{u} \rangle(\boldsymbol{x})$ and the turbulent viscosity ν_t can be obtained from a standard CFD model, e.g., either using RANS turbulence modeling or LES turbulence modeling. The dispersion is then modeled using a time-dependent three-dimensional advection-diffusion problem (cf. Eq. 2.12). The minimization problem under consideration is therefore a PDE-constrained, convex optimization problem that corresponds to

$$\min_{(c,\sigma,\boldsymbol{y})} \mathcal{J}(c,\sigma,\boldsymbol{y}) \tag{6.2}$$

subject to

$$\left\{ \begin{array}{rll} \dfrac{\partial c}{\partial t} + \nabla \cdot \langle \boldsymbol{u} \rangle c - \nabla \cdot \dfrac{\nu_t}{Sc_t} \nabla c & = \sigma & \text{in } \Omega \times (0,T] \\ y_i & = f_i(c) & \text{in } (0,T] \text{ for } i = 1 \ldots M \end{array} \right. \tag{6.3}$$

where the function f_i relates the pollutant concentration in the domain to the measurements at measurement point i. In the current study, we presume that $c(0) = 0$ and that function f_i is linearly depending on c such that $f_i(c) = \int_\Omega \psi_i(\boldsymbol{x}) c(\boldsymbol{x}) d\Omega$ where ψ_i characterizes the spatial sampling properties of the measurement equipment near the measurement point $\boldsymbol{x}_i$. For instance, for a point measurement, $\psi_i(\boldsymbol{x}) = \delta(\boldsymbol{x} - \boldsymbol{x}_i)$. However, e.g., for radioactive dose measurements, it can be a more complicated function (see §2.4.2).

We introduce the Lagrange multipliers $\varsigma(\boldsymbol{x}, t)$ and $\varphi_i(t)$ to construct the Lagrangian for this problem as

$$\mathcal{L}(c, \sigma, \boldsymbol{y}, \varsigma, \boldsymbol{\varphi}) = \frac{1}{2}\int_0^T \sum_{i=1}^{M} (y_i - \hat{y}_i)^2 \, dt + \frac{\beta}{2}\int_0^T \int_\Omega \sigma^2 d\Omega dt +$$

$$\frac{\gamma}{2}\int_0^T \int_\Omega \left(\frac{\partial \sigma}{\partial t}\right)^2 d\Omega dt + \int_0^T \int_\Omega \left(\frac{\partial c}{\partial t} + \nabla \cdot \langle \boldsymbol{u} \rangle c - \nabla \cdot \frac{v_t}{Sc_t}\nabla c - \sigma\right) \varsigma d\Omega dt +$$

$$\sum_{i=1}^{M} \int_0^T \left(-y_i + f_i\right) \varphi_i dt, \quad (6.4)$$

where $\boldsymbol{\varphi} = [\varphi_1 \; \varphi_2 \; \dots \; \varphi_M]$. Since the critical point of Eq. (6.4) corresponds to the solution of Eq. (6.2), the first-order optimality conditions for Eq. (6.2) are obtained by imposing that the variation of the Lagrangian with respect to each of its variables is equal to zero. Optimality is therefore reached when (see Appendix A for the full derivation)

$$\frac{\partial c}{\partial t} + \nabla \cdot \langle \boldsymbol{u} \rangle c - \nabla \cdot \frac{v_t}{Sc_t}\nabla c = \sigma, \quad (6.5a)$$

$$-\frac{\partial \varsigma}{\partial t} - \nabla \cdot \langle \boldsymbol{u} \rangle \varsigma - \nabla \cdot \frac{v_t}{Sc_t}\nabla \varsigma = \sum_{i=1}^{M} \psi_i(\hat{y}_i - f_i), \quad (6.5b)$$

$$\beta\sigma + \gamma\frac{\partial^2 \sigma}{\partial t^2} - \varsigma = 0, \quad (6.5c)$$

with initial conditions

$$c(0) = 0, \qquad \frac{\partial \sigma}{\partial t}(0) = 0, \quad (6.6)$$

final conditions

$$\varsigma(T) = 0, \qquad \frac{\partial \sigma}{\partial t}(T) = 0, \quad (6.7)$$

and boundary conditions

$$c(\partial\Omega_{inlet}) = 0, \qquad \varsigma(\partial\Omega_{outlet}) = 0. \quad (6.8)$$

At the other boundaries, Neumann boundary conditions apply to c and ς.

Spatial discretization of Eqs. (6.5a-c), e.g. using a finite-volume approach, on a grid of n cells, and temporal discretization into nt intervals, e.g. using the implicit Euler method for the first order time derivative and the central difference approximation for the second derivative, results in a large linear system of the form

$$I_n \frac{\tilde{c}^k - \tilde{c}^{k-1}}{\Delta t} + A\tilde{c}^k + I_n \tilde{\sigma}^k = 0, \tag{6.9a}$$

$$I_n \frac{\tilde{\varsigma}^k - \tilde{\varsigma}^{k+1}}{\Delta t} + A^* \tilde{\varsigma}^k + \sum_{i=1}^{M} \Psi_i(\Psi_i^T \tilde{c}^k) = \sum_{i=1}^{M} \Psi_i \hat{y}_i^k, \tag{6.9b}$$

$$\beta I_n \tilde{\sigma}^k + \gamma I_n \frac{\tilde{\sigma}^{k-1} - 2\tilde{\sigma}^k + \tilde{\sigma}^{k+1}}{\Delta t} - I_n \tilde{\varsigma}^k = 0, \tag{6.9c}$$

where $k = 1 \dots T$, $\tilde{c}(t)$, $\tilde{\varsigma}(t)$, and $\tilde{\sigma}(t) \in \mathbb{R}^n$ are the solution vectors containing the concentration, the adjoint concentration, and the pollutant emission rate of every cell in the domain, respectively. The matrix I_n is a $n \times n$ identity matrix, the matrix $A \in \mathbb{R}^{n \times n}$ is the discrete representation of the advection and the diffusion operator, including the spatial boundary conditions for the forward equation (Eq. 6.5a), the matrix $A^* \in \mathbb{R}^{n \times n}$ is similarly defined for the backward equation (Eq. 6.5b), the vector $\Psi_i \in \mathbb{R}^n$ is the spatial discretization of ψ_i, and $\Psi_i^T \tilde{c}$ is the discrete representation of $f_i(c)$. Unfortunately, the combination of the initial condition for c and the final condition for ς impedes solving Eq. (6.9) through classical time- marching. Instead, the solution can only be obtained by solving the coupled system

$$\begin{bmatrix} D^{ic} & R^{ic} & 0 & \cdots & & \cdots & 0 \\ L & D & R & \ddots & & & \vdots \\ 0 & L & D & R & & & \\ \vdots & \ddots & \ddots & \ddots & \ddots & \ddots & \vdots \\ & & & L & D & R & 0 \\ \vdots & & & \ddots & L & D & R \\ 0 & \cdots & & \cdots & 0 & L^{ic} & D^{ic} \end{bmatrix} \begin{bmatrix} v^0 \\ \vdots \\ v^k \\ \vdots \\ v^{nt} \end{bmatrix} = \begin{bmatrix} b^0 \\ \vdots \\ b^k \\ \vdots \\ b^{nt} \end{bmatrix}, \tag{6.10}$$

where k is the time step index, $v^k = [\tilde{c}^k \; \tilde{\varsigma}^k \; \tilde{\sigma}^k]^T \in \mathbb{R}^{3n}$, and $b^k = [0 \; \sum_{i=1}^{M} \Psi_i \hat{y}_i^k \; 0]^T \in \mathbb{R}^{3n}$. Further, superscript ic indicates a modified matrix accounting for the initial conditions. Finally, D, L, and $R \in \mathbb{R}^{3n \times 3n}$ are defined as

$$D = \begin{bmatrix} A + \frac{I_n}{\Delta t} & 0 & I_n \\ \sum_{i=1}^{M} \Psi_i \Psi_i^T & A^* + \frac{I_n}{\Delta t} & 0 \\ 0 & -I_n & \left(\beta - \frac{2\gamma}{\Delta t^2}\right) I_n \end{bmatrix}, \tag{6.11}$$

$$L = \begin{bmatrix} -\frac{I_n}{\Delta t} & 0 & 0 \\ 0 & 0 & 0 \\ 0 & 0 & \frac{\gamma}{\Delta t^2} I_n \end{bmatrix}, \tag{6.12}$$

$$R = \begin{bmatrix} 0 & 0 & 0 \\ 0 & -\frac{I_n}{\Delta t} & 0 \\ 0 & 0 & \frac{\gamma}{\Delta t^2} I_n \end{bmatrix}. \tag{6.13}$$

Considering a typical mesh size of 10^7 cells and nt in the order of 10^3, the DOF of the system of Eq. (6.10) is approximately 3×10^{10}. It is clear that the system is computationally too expensive to solve in real time for practical applications.

6.2 Reduced order system

In order to be applicable to practical problems, the DOF of the system in Eq. (6.10) must be reduced considerably in size. This can be achieved by reducing the order of each submatrix D, L, and R. In Chapter 5 it is illustrated that for a linear advection-diffusion problem effective MOR can be achieved by projection of the original system onto a Krylov subspace. However, this requires a priori knowledge of the spatial distribution of the source term. While this is the case for the adjoint equation, where the measurement locations serve as source locations (cf. Eq. 6.9b), the source locations are not known for the forward equation (cf. Eq. 6.9a) as this is essentially the nature of a source reconstruction problem.

Thus far, no prior assumptions regarding the spatial or time distribution of the source are made although in practice the number of possible source locations is often limited to a finite number of possibilities. Among others, these could be the exhausts from chimneys, valves, piping, and tanks. By constraining the source locations $\boldsymbol{x}_j$ to a limited number of locations S, the source can be decomposed into the sum of S products of a spatial ($b_j(\boldsymbol{x})$) and a temporal ($\sigma_j(t)$) component, i.e.

$$\sigma(\boldsymbol{x}, t) = \sum_{j}^{S} b_j(\boldsymbol{x}) \sigma_j(t), \tag{6.14}$$

where $b_j(\boldsymbol{x})$ can either represent a point source in which case $b_j = \delta(\boldsymbol{x} - \boldsymbol{x}_j)$ or a spatially more complex source (e.g. a multi-dimensional Gaussian function). Further $\int_\Omega b_j(\boldsymbol{x}) d\Omega = 1$. Moreover, for sake of simplicity, we presume in the current manuscript that $\int_\Omega b_j(\boldsymbol{x}) b_i(\boldsymbol{x}) d\Omega = 0$, i.e. that sources are spatially disjoint. In fact, it is straightforward to omit this condition, but this leads to more complex matrix notations below, and for most practical cases this presumption is justified.

Each source $b_j\sigma_j$ results in a concentration field $c_j(\boldsymbol{x}, t)$ and since the problem is linear the total pollutant concentration can therefore be reconstructed as $c(\boldsymbol{x}, t) = \sum_j^S c_j(\boldsymbol{x}, t)$. Furthermore, from Eq. (6.5b) it is readily seen that the adjoint of the concentration field can be decomposed as $\varsigma(\boldsymbol{x}, t) = \sum_i^M \varsigma_i(\boldsymbol{x}, t)$ by considering each measurement location separately. Therefore, the system of Eqs. (6.5a-c) can be reformulated as (no Einstein summation over indices i and j)

$$\frac{\partial c_j}{\partial t} + \nabla \cdot \langle \boldsymbol{u} \rangle c_j - \nabla \cdot \frac{v_t}{Sc_t} \nabla c_j = b_j \sigma_j \qquad \text{for } j = 1 \ldots S, \tag{6.15a}$$

$$-\frac{\partial \varsigma_i}{\partial t} - \nabla \cdot \langle \boldsymbol{u} \rangle \varsigma_i - \nabla \cdot \frac{v_t}{Sc_t} \nabla \varsigma_i = \psi_i \left(\hat{y}_i - \int_\Omega \psi_i \sum_{j=1}^{S} c_j d\Omega \right) \qquad \text{for } i = 1 \ldots M, \tag{6.15b}$$

$$\beta \|b_j\|^2 \sigma_j + \gamma \|b_j\|^2 \frac{\partial^2 \sigma_j}{\partial t^2} = \sum_{i=1}^{M} \int_\Omega b_j(\boldsymbol{x}) \varsigma_i(\boldsymbol{x}, t) d\Omega \qquad \text{for } j = 1 \ldots S, \tag{6.15c}$$

and where $\|b_j\|^2 = \int_\Omega b_j(\boldsymbol{x}) b_j(\boldsymbol{x}) d\Omega$. The set of S equations in Eq. (6.15c) simply follows from the fact that we have selected a finite-dimensional spatial representation for $\sigma(\boldsymbol{x}, t)$, i.e. using Eq. (6.14). Thus, Eq. (6.15c) is obtained from a Galerkin projection of Eq. (6.5c) using $b_j(\boldsymbol{x})$ ($j = 1 \ldots S$) as test functions, and $\int_\Omega b_j(\boldsymbol{x}) b_i(\boldsymbol{x}) d\Omega = 0$.

Spatial discretization of Eqs. (6.15a) and (6.15b) results in $M + S$ coupled systems of order n, each of the form

$$\frac{\mathrm{d}\tilde{\alpha}_i}{\mathrm{d}t} + A_i \tilde{\alpha}_i + B_i s = 0, \tag{6.16}$$

where α_i is either c_j or ς_i, the matrix A_i (or A_i^* in case of a backward equation) is the discrete representation of the advection and the diffusion operator, including the spatial boundary conditions, and the vector B_i contains the contribution of every cell to the source. Hence, B_i is the spatial discretization of b_i in case of the forward equations, and $B_i^* = \Psi_i$ in case of the backward equations. We further note that source input $s(t) = \sigma_j(t)$ $(j = 1 \dots S)$ in case of the forward equations, and $s(t) = -\hat{y}_i + \int_\Omega \psi_i \sum_{j=1}^S c_j d\Omega$ $(i = 1 \dots M)$ in case of backward equations.

It is now possible to reduce the order of the system of Eq. (6.16) to r $(\ll n)$ by projection of the original system onto a Krylov subspace of order r. A system of strongly reduced order is obtained in this way which behaves similar to the original system. To this end, the discrete solution vector $\tilde{\alpha}_i$ is approximated by $\tilde{\alpha}_i \approx V_i \bar{\alpha}_i$, where projection matrix $V_i \in \mathbb{R}^{n \times r}$ is an orthogonal basis of a Krylov subspace and $\bar{\alpha}_i$ is the corresponding reduced-order solution vector. Substitution of this approximation in Eq. (6.16) followed by the Galerkin projection results in the ROM (cf. Chapter 5). For instance for the forward equation, the ROM is given by

$$\frac{\mathrm{d}\bar{c}_j}{\mathrm{d}t} + V_j^T A_j V_j \bar{c}_j + V_j^T B_j \sigma_j = 0, \qquad \text{for } j = 1 \dots S \tag{6.17}$$

where $A_{r,j} = V_j^T A_j V_j$ and $B_{r,j} = V_j^T B_j$ for $j = 1 \dots S$. We construct the projection matrix V_i using the one-sided Arnoldi algorithm in order to ensure stability of the ROM. Note that because the Arnoldi algorithm uses B_i or B_i^* as input for the construction of V_i, the algorithm must be repeated for each of the $M + S$ systems. However, once set up, the ROMs can be applied to any source reconstruction problem for the given wind direction.

After temporal discretization, the discretized system of equations of reduced order is written as

$$I_r \frac{\bar{c}_j^k - \bar{c}_j^{k-1}}{\Delta t} + A_{r,j} \bar{c}_j^k + B_{r,j} \sigma_j^k = 0 \qquad \text{for } j = 1 \dots S, \tag{6.18a}$$

$$I_r \frac{\bar{\varsigma}_i^k - \bar{\varsigma}_i^{k+1}}{\Delta t} + A_{r,i}^* \bar{\varsigma}_i^k + B_{r,i}^* \sum_{j=1}^{S} C_j \bar{c}_j^k = B_{r,i}^* \hat{y}_i^k \quad \text{for } i = 1 \dots M, \tag{6.18b}$$

$$\beta B_j^T B_j \sigma_j^k + \gamma B_j^T B_j \frac{\sigma_j^{k-1} - 2\sigma_j^k + \sigma_j^{k+1}}{\Delta t} + \sum_{i=1}^{M} C_{i,j}^* \bar{\varsigma}_i^k = 0 \qquad \text{for } j = 1 \dots S, \tag{6.18c}$$

where $A_{r,j}$ and $B_{r,j}$ are given above, and $A_{r,i}^* = V_i^T A_i^* V_i$, $B_{r,i}^* = V_i^T B_i^*$, $C_j = \Psi_j^T V_j$ and $C_{i,j}^* = B_j^T V_i$ (for $i = 1 \dots M$ and $j = 1 \dots S$). In matrix notation, the system can be written in the same form as Eq. (6.10), but with

$$v^k = \left[\begin{array}{c|c|c} \bar{c}_1^k \cdots \bar{c}_S^k & \bar{\varsigma}_1^k \cdots \bar{\varsigma}_M^k & \sigma_1^k \cdots \sigma_S^k \end{array}\right]^T \quad \in \mathbb{R}^{((r+1)S+rM)}, \tag{6.19}$$

$$b^k = \left[\begin{array}{c|c|c} 0 \cdots 0 & B_{r,1}^* \hat{y}_1^k \cdots B_{r,M}^* \hat{y}_M^k & 0 \cdots 0 \end{array}\right]^T \quad \in \mathbb{R}^{((r+1)S+rM)}, \tag{6.20}$$

and where D, L, and $R \in \mathbb{R}^{((r+1)S+rM)\times((r+1)S+rM)}$ are given by

$$D = \left[\begin{array}{ccc|ccc|ccc}
A_{r,1} + \frac{I_r}{\Delta t} & & 0 & & & & B_{r,1} & & 0 \\
& \ddots & & & 0 & & & \ddots & \\
0 & & A_{r,S} + \frac{I_r}{\Delta t} & & & & 0 & & B_{r,S} \\
\hline
B_{r,1}^* C_1 & \cdots & B_{r,1}^* C_S & A_{r,1}^* + \frac{I_r}{\Delta t} & & 0 & & & \\
\vdots & \ddots & \vdots & & \ddots & & & 0 & \\
B_{r,M}^* C_1 & \cdots & B_{r,M}^* C_S & 0 & & A_{r,M}^* + \frac{I_r}{\Delta t} & & & \\
\hline
& & & C_{1,1}^* & \cdots & C_{M,1}^* & \left(\beta - \frac{2\gamma}{\Delta t^2}\right) B_1^T B_1 & & 0 \\
& 0 & & \vdots & \ddots & \vdots & & \ddots & \\
& & & C_{1,S}^* & \cdots & C_{M,S}^* & 0 & & \left(\beta - \frac{2\gamma}{\Delta t^2}\right) B_S^T B_S
\end{array}\right], \tag{6.21}$$

$$L = \left[\begin{array}{ccc|ccc|ccc}
-\frac{I_r}{\Delta t} & 0 & & & \cdots & & & & 0 \\
0 & \ddots & & & & & & & \\
& & -\frac{I_r}{\Delta t} & & & & & & \\
\hline
& & & 0 & & & & & \\
\vdots & & & & \ddots & & & & \vdots \\
& & & & & 0 & & & \\
\hline
& & & & & & \frac{\gamma B_1^T B_1}{\Delta t^2} & & \\
& & & & & & & \ddots & 0 \\
0 & & & & \cdots & & & 0 & \frac{\gamma B_S^T B_S}{\Delta t^2}
\end{array}\right], \tag{6.22}$$

$$R = \left[\begin{array}{ccc|ccc|ccc}
0 & & & & \cdots & & & & 0 \\
& \ddots & & & & & & & \\
& & 0 & & & & & & \\
\hline
& & & -\frac{I_r}{\Delta t} & & & & & \\
\vdots & & & & \ddots & & & & \vdots \\
& & & & & -\frac{I_r}{\Delta t} & & & \\
\hline
& & & & & & \frac{\gamma B_1^T B_1}{\Delta t^2} & & \\
& & & & & & & \ddots & 0 \\
0 & & & & \cdots & & & 0 & \frac{\gamma B_S^T B_S}{\Delta t^2}
\end{array}\right]. \tag{6.23}$$

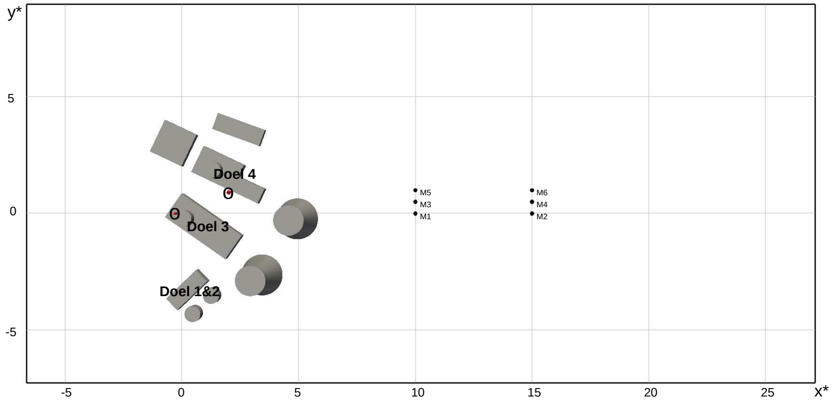

Figure 6.2: Computational domain with source locations (◦) and measurement locations (•).

As shown in Chapter 5, r around 100 yields good results for 3D atmospheric dispersion problems. Further considering nt in the order of 10^3, and $S = M = 5$, the DOF of the time-discretized system is now in the order 10^6. Hence, by application of the model reduction, the DOF of the system of first order optimality is reduced to a solvable size.

6.3 Case set-up

In this section, we first detail the site considered in the current work and the locations of the monitoring points in §6.3.1. Next, in §6.3.2, the computational set-up that is used to construct the ROMs and to solve the optimization problem, is elaborated.

6.3.1 Case description

A time-dependent pollutant release at the Doel Nuclear Power Station from two different locations is the subject of the present case study. The geometry of the case is identical to that of Chapter 5 and is shown in Fig. 6.2. It includes four cylindrical reactor buildings, two hyperbolic cooling towers of 176 m high and a number of cuboid auxiliary buildings. A uniform roughness length $z_0 = 0.01$ m corresponding with short grassland is set for the ground. The wind is set to come from the southwest which is the prevailing wind direction for this location.

The friction velocity is set to 0.25 ms^{-1} which corresponds to a wind speed of 20 kmh^{-1} ($= U$) at 74 m altitude ($= L$) according to the logarithmic velocity profile. This altitude corresponds to the height of the chimney of Doel 3.

In order to verify our methodology, we perform a source reconstruction using virtual measurements ($\hat{y}_i(t)$ for $i = 1 \dots M$). The virtual measurements are constructed by sampling the local pollutant concentration at the six locations downstream from the pollutant sources (cf. Fig. 6.2) during a forward simulation of the pollutant dispersion with the full CFD model. Thus $\psi_i(\boldsymbol{x}) = \delta(\boldsymbol{x} - \boldsymbol{x}_i)$. Two hypothetical source locations are considered, i.e. the chimney of Doel 3 and a fictive leaking tank next to Doel 4. The release of the pollutant from both Doel 3 (σ_1) and the leaking tank (σ_2) are modeled as a Gaussian function in time

$$\sigma_i(t) = \theta_i \exp\left(0.5\left(\frac{t - 5\tau_i}{\tau_i}\right)^2\right) \qquad \text{for } i = 1, 2, \tag{6.24}$$

where we set $\tau_1 = U/L$ and $\tau_2 = 1.5U/L$. The parameter θ_i is chosen such that $\int_0^\infty \sigma_i(t')dt' = 1$. Three cases are considered, i.e. a single release from Doel 3, a single release from the leak, and a simultaneous release from the chimney and the leak. In order to test the robustness of the methodology, a set of noisy measurements is derived from the noise-free measurements by rescaling the sample values by a random number chosen from the interval $[1 - \alpha, 1 + \alpha]$. In this work, we use $\alpha = 0.2$.

Once a set of measurements is generated, the source reconstruction methodology can be tested. To this end, the generated measurements are used to set up b^k in Eq. (6.20) for each time step ($k = 1 \dots nt$). The reconstructed source profiles are subsequently obtained by solving Eq. (6.10) in its reduced form, i.e. using Eq. (6.19)-(6.23). Finally, the measurements are reconstructed as $y_j = \Psi_j^T \sum_i^S V_i \bar{c}_i$ for each measurement locations ($j = 1 \dots M$).

In order to assess the quality of the reconstructed source with respect to the true source ($\hat{\sigma}$), two performance measures are used, i.e., the fractional bias (FB) and the normalized mean square error (NMSE) [30]:

$$\mathrm{FB} = 2\frac{\sum_i^S \sum_k^{nt} \left(\sigma_i^k - \hat{\sigma}_i^k\right)}{\sum_i^S \sum_k^{nt} \left(\sigma_i^k + \hat{\sigma}_i^k\right)}, \tag{6.25}$$

$$\mathrm{NMSE} = ST\frac{\sum_i^S \sum_k^{nt} \left(\sigma_i^k - \hat{\sigma}_i^k\right)^2}{\left(\sum_i^S \sum_k^{nt} \sigma_i^k\right)\left(\sum_i^S \sum_k^{nt} \hat{\sigma}_i^k\right)}. \tag{6.26}$$

It is readily seen that a perfect reconstruction would yield FB and NMSE = 0. In addition, both performance measures are also applied to the reconstructed measurements with respect to the “true” measurements.

6.3.2 Computational set-up

For a given set of wind conditions, matrices D, L and R (cf. Eq. 6.21 – 6.23) can be set up a priori. First, the steady velocity field and the eddy viscosity are solved by performing a RANS simulation. The $k-\epsilon$ model in which the model coefficients are chosen in accordance with Richards and Hoxey [108] is applied to provide turbulence closure. Also the boundary conditions for the velocity field simulation are set in accordance with Richards and Hoxey [108]. The transport equations are spatially discretized using second-order schemes on a fully hexahedral mesh consisting of 8.0 M cells. The mesh is gradually refined towards the buildings, following the COST 732 and AIJ guidelines [47, 138]. The simulation is performed using the OpenFOAM finite-volume open-source simulation platform on 40 processors distributed over two nodes, installed with Intel Xeon E5-2680 v2 processors and interconnected through DDR infiniband. Convergence is assumed after the residuals have dropped below 10^{-7}.

Next, the ROMs are constructed for the each of the forward and adjoint equations of Eqs. (6.15a) and (6.15b). Because we consider two different source locations ($S = 2$) and six measurement points ($M = 6$), eight different ROMs are therefore set up. For every forward equation in Eq. (6.15a), the projection matrix V_i (cf. Eq. 6.17) is constructed using Algorithm 2 in Chapter 5 from a sequence of steady state solutions to the advection-diffusion equation with different source terms given by the algorithm. To that end, OpenFOAM is used, with the same mesh as the RANS simulation discussed above, and using the background velocity field obtained from the RANS. Following Chapter 5, we use 100 modes per ROM, so that 100 steady-state advection-diffusion simulations are required per ROM. For the further implementation of the algorithm we use the Petsc library [7, 8, 9].

The ROMs for the adjoint equations (cf. Eq. 6.15b) are constructed using the same methodology as the forward equations. The steady state adjoint equation in OpenFOAM is simply obtained by changing the sign of the velocity flux in the advection term of the forward equation. Subsequently, the steady-state solutions for the different source terms are obtained using false time-stepping. This source terms are again determined by Algorithm 2 in Chapter 5.

Once D L and R are set up, the reconstruction can be applied to any set of time-dependent measurements obtained at the locations considered and under the given wind conditions. In order to solve the system of Eq. (6.10), a parallel direct solver based on dense LU factorization provided by the Petsc library is used with one processor for every 2×10^5 DOF. In total 2250 time steps are simulated for the source reconstruction. With a time step of $\Delta t^* = 0.02$, this corresponds to $t^* = 45$ or approximately 10 min real-time when considering a wind speed of 20 kmh^{-1} at 74 m altitude. With six measurement locations and one source included in the simulation, the DOF of the system of Eq. (6.10) equals 1.59×10^6. Using default tools provided by Petsc library, it takes 582 seconds on seven processors to obtain a solution. In case two sources are considered, DOF of the system of Eq. (6.10) increases to 1.82×10^6 which takes 720 seconds to solve on nine processors. Hence, the required simulation time is in the order of the simulated physical time span with room for further numerical optimization.

6.4 Results

In this section, the results of the cases studied are presented by comparing the reconstructed sources and related measurement predictions with the virtual measurements. First, in §6.4.1, the results of the single emission are discussed in detail. Subsequently, in §6.4.2, the results of the source reconstruction with multiple sources are presented.

6.4.1 Single source

The pollutant emission from the Doel 3 chimney is used to discuss the general simulation results. The concentration measurements at the six locations indicated in Fig. 6.2 are used to reconstruct the time-dependent pollutant source. For each of the measurement locations, a ROM is constructed for use in Eq. (6.18b). The chimney is the only possible source considered for the construction of the ROM in Eq. (6.18a). Thus, in total seven ROMs are included in the system. Before looking in detail at the quality of the reconstructed source, we first look at the non-dimensional concentration at measurement locations M1 and M2 as function of the non-dimensional time t^*, shown in Fig. 6.3a. In this graph, solid circles represent the noise-free artificial measurements, i.e. the true concentration profile, while the crosses represent the measurements with additional noise. It is observed that the reconstructed profiles are almost perfectly overlapping and closely match the noise-free measurements. The peak concentration is slightly underestimated but the difference is negligible. In addition, from the small difference between the reconstructed profiles using noise-free and noisy measurements it is seen

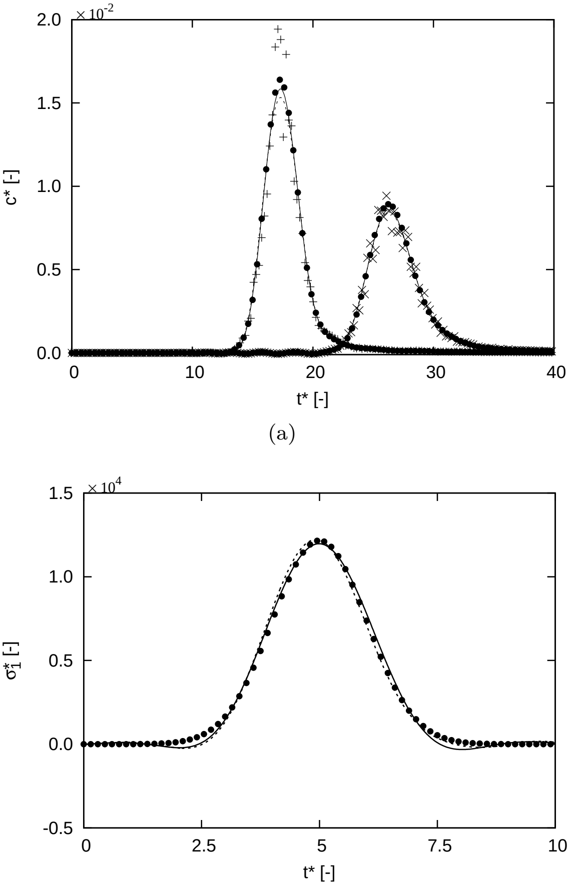

(a)

(b)

Figure 6.3: Profiles of the the non-dimensional concentration $c^*(= cUL^2/R)$ (a), and the non-dimensional source $\sigma_i^*(= \sigma_i L^3/R)$ (b) for an emission from Doel 3. Symbols: (●): Noise-free measurement; (+): Noisy measurement ($\alpha = 0.2$) at M1; (×): Noisy measurement ($\alpha = 0.2$) at M2. Lines: (—): Reconstructed profile using noise-free measurements; (−−): Reconstructed profile using noisy measurements.

that the noise on the measurements has a negligible effect on the source reconstruction.

The corresponding time evolution of the non-dimensional reconstructed source σ_1^* is shown as a function of the non-dimensional time t^* in Fig. 6.3b. A close match is found between the reconstructed profiles, using either noise-free or noisy measurements, and the Gaussian profile imposed for producing the artificial measurements. At the time of peak emission rate $t^* = 5$, the difference between the reconstructed profiles and the imposed profile is less than 1.6%. Towards the tails of the profile, $t^* \approx 2.5$ and $t^* \approx 7.5$, the difference increases slightly but it remains well within the acceptable limits. The total amount of pollutant emitted, i.e. the time integral of the emission rate, is underestimated by 0.74% and 1.57% when using noise-free and noisy measurements, respectively. Clearly, the method is well capable of reconstructing emission profile of a single source.

The results of Fig. 6.3 are obtained using regularization parameters $\beta = 5{\cdot}10^{-12}$ and $\gamma = 5{\cdot}10^{-10}$. These parameters can often be selected from the corner in the L-curve which results from plotting the norm of the solution against the norm of the residual on a log-log scale [63, 71]. Unfortunately, very low values for the regularization parameters negatively influence the solvability of the system in Eq. (6.10). As a result, the current case does not yield the typical L-shape due to the limited lower range of the parameters for which a solution could be obtained. Therefore, we employ an alternative approach to chose β and γ by investigating the effect of their value on the quality of the FB and NMSE. Remind that FB measures the mean bias, i.e. the error on the total amount of pollutant emitted and measured, while NMSE measures more the scatter of the error (cf. §6.3.1). The evolution of the absolute value of FB as function of β and γ is shown in Fig. 6.4a for the noisy measurements with $\alpha = 0.2$, and in Fig. 6.4b for the corresponding reconstructed source. In these graphs, the white circle indicates the values for β and γ employed in the present work. It is observed that the FB decreases monotonously with decreasing β and γ for both the measurements and the source. Although very close in value, the mean biases are not exactly identical due to the random noise added to the virtual measurements. In general, it can therefore be stated that increasing either β and γ, i.e. adding more regularization to the cost functional, increases the absolute value of the FB for both the source and the measurement. Hence, a small amount of regularization is favorable in order to keep the FB close to zero.

However, a small mean bias does not give any information regarding the existence of oscillations. For this, the evolution of the NMSE of the source in Fig. 6.5b can be used. It can be deduced that a too small amount of regularization induces oscillatory behaviour in the source due to the insufficient

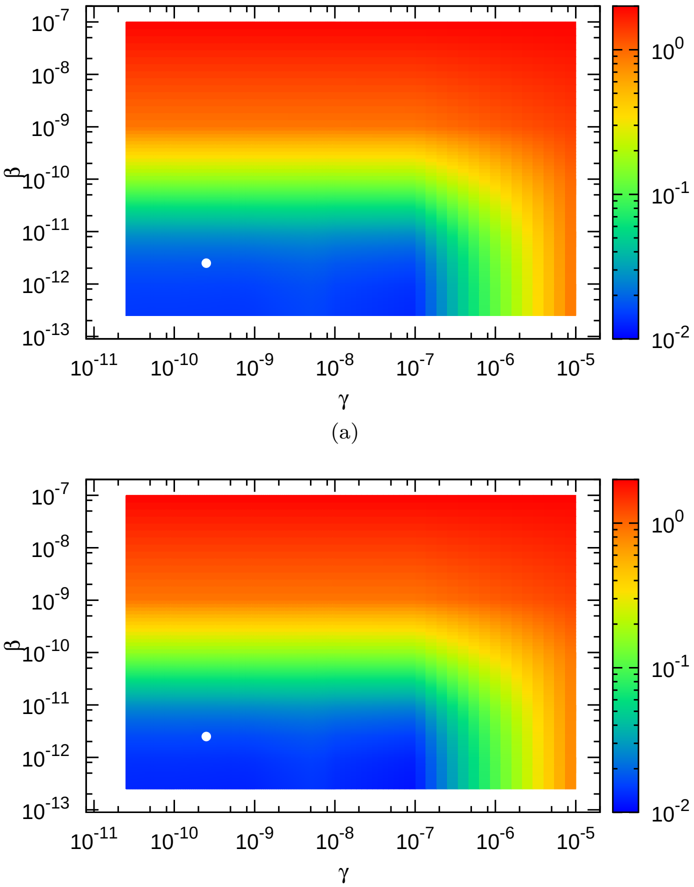

(a)

(b)

Figure 6.4: Contours of the absolute value of FB for the emission from Doel 3 as function of regularization parameters β and γ. (a) Noisy measurements ($\alpha = 0.2$); (b) Source; White circle indicates the values that were used in the present case.

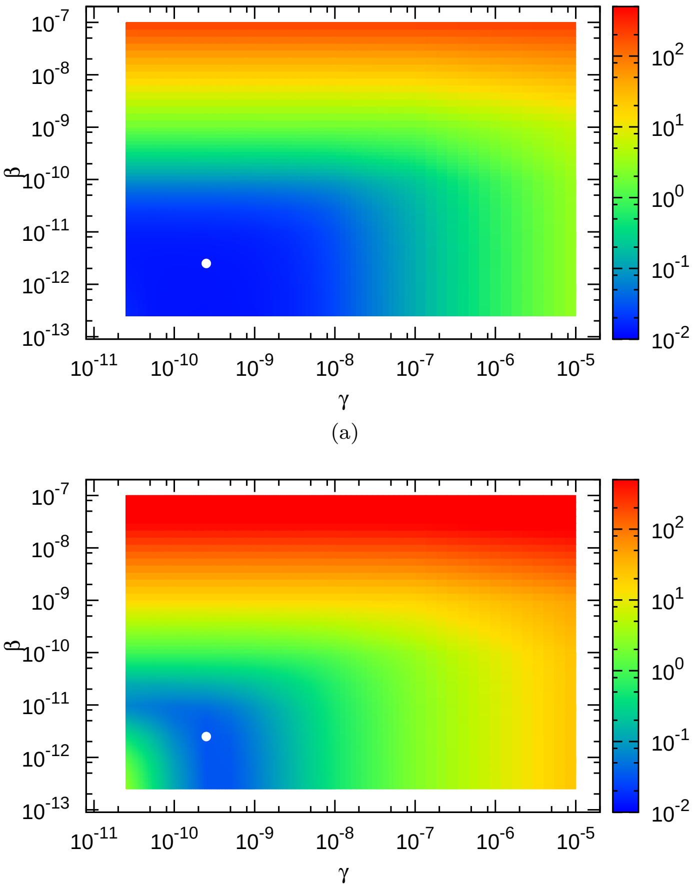

(a)

(b)

Figure 6.5: Contours of the NMSE for the emission from Doel 3 as function of regularization parameters β and γ. (a) Noisy measurements ($\alpha = 0.2$); (b) Source; White circle indicates the values that were used in the present case.

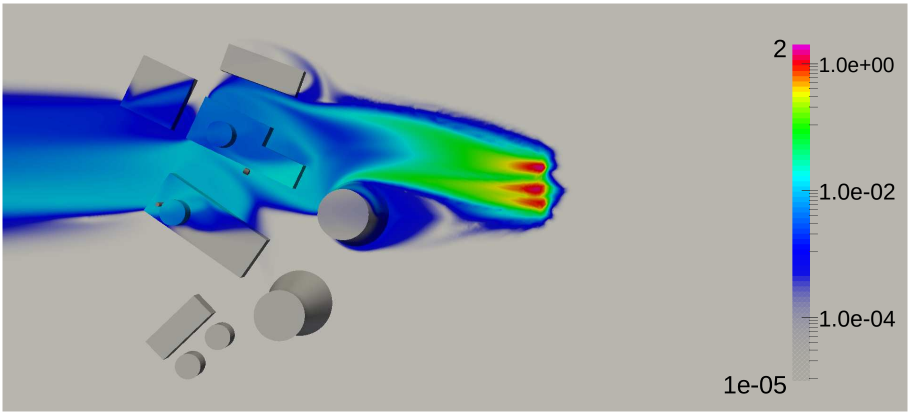

(a)

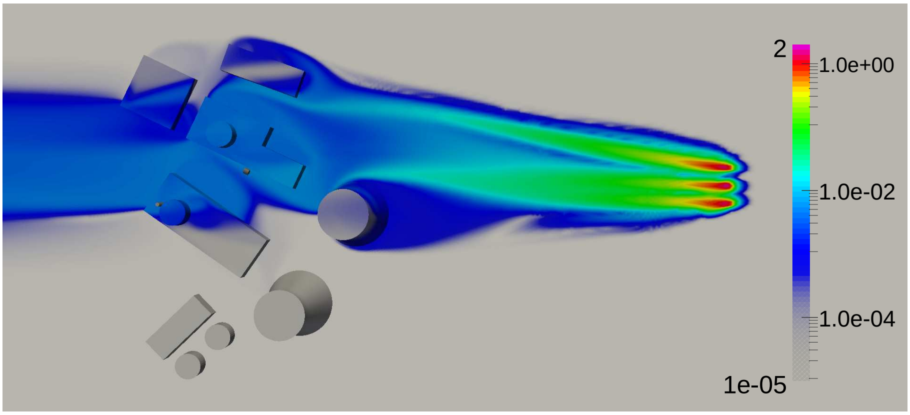

(b)

Figure 6.6: Contour of the sum of the steady adjoint field ($\sum_i \varsigma_i$) at the ground and the building surface for (a) measurement locations M1, M3, M5, and (b) measurement locations M2, M4, M6.

damping of unphysical negative emission rates. At $\beta \approx 5 \cdot 10^{-12}$ and $\gamma \approx 5 \cdot 10^{-10}$, the NMSE is minimal. For larger values of the regularization parameters, the NMSE increases due to the increase in FB. An increasing NMSE is also observed for decreasing values of β despite the decrease in FB. This is only possible with the occurrence of oscillations. The minimal value for the NMSE of the source motivates our choice for the use of $\beta \approx 5 \cdot 10^{-12}$ and $\gamma \approx 5 \cdot 10^{-10}$ in this work.

Finally, it is worth noting that the steady-state adjoint field ς_i of a measurement location M_i can be interpreted as the sensitivity of the particular measurement location to a source in the domain. A source at a location with a large value for ς_i is therefore more easy to measure at location M_i. The contour plots of the sum of the steady-state adjoint fields at the ground and the building surface for the first row of the concentration measurement locations considered is show in Fig. 6.6a, and for the second row in Fig. 6.6b. Obviously, sources upstream but close the measurement location are the most easily detected. In addition, it is found that an emission from Doel 3 is more easily measured at M1, M3 and M5. At M2, M4 and M6, an emission from Doel 4 will be more easily detected. Note that for wind coming from the southwest, the six measurement locations considered in this work are not sensitive to an emission from Doel 1 or Doel 2.

6.4.2 Multiple sources

In order to study the capabilities of the methodology with respect to multiple possible sources, we first apply the methodology to a Gaussian-shaped release from the leaking tank while considering both the chimney of Doel 3 and the tank next to Doel 4 as possible sources. Next, a simultaneous release from Doel 3 and the leaking tank is studied. We further also show that the method produces unphysical results in case the true source location is not included in the reduced-order model, emphasizing the importance of including all possible sources in the set $1 \dots S$ of the forward ROMs.

We now first turn to the case of the Gaussian-shaped release from the leaking tank next to Doel 4 while considering both the chimney of Doel 3 and the tank as possible sources. Because we consider two different source locations and six measurement points, in total eight ROMs are used for the reconstruction. As illustrated in Fig. 6.7a, the reconstructed concentration profiles match the noise free measurements closely. At M1, the measurements and the reconstructed profiles match nearly perfectly. Also at M2, a close match is found although the peak concentration is slightly underestimated. Again, nearly no difference is observed between the reconstructed concentration profiles using either the noise free measurements or the noisy measurements.

In Fig. 6.7b and Fig. 6.7c, the evolution of the non-dimensional reconstructed sources σ_1^* and σ_2^* from Doel 3 and the leaking tank, respectively, are shown as a function of the non-dimensional time t^*. No pollutant was emitted from the chimney at Doel 3 and only a very small non-zero emission rate is found (Fig. 6.7b). This is the case when using noise free measurements ($\alpha = 0.0$) and when using noisy measurements ($\alpha = 0.2$) for the source reconstruction. The reconstructed release rate from the leaking tank (Fig. 6.7c) compares

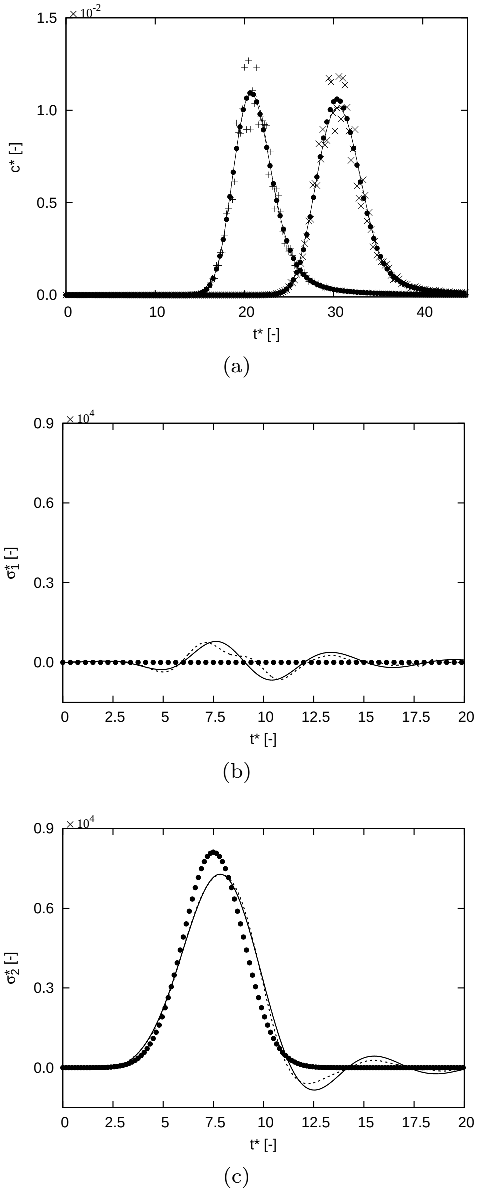

(a)

(b)

(c)

Figure 6.7: Profiles of the non-dimensional concentration $c^*(= cUL^2/R)$ (a), and the non-dimensional source $\sigma_i^*(= \sigma_i L^3/R)$ from Doel 3 (b), and from the leaking tank (c). Symbols: (●): Noise-free measurement; (+): Noisy measurement ($\alpha = 0.2$) at M1; (×): Noisy measurement ($\alpha = 0.2$) at M2. Lines: (—): Reconstructed profile using noise-free measurements; (− −): Reconstructed profile using noisy measurements.

relatively well with the true emission rate. At peak emission rate, the difference between the reconstructed peak emission rate and the true emission rate is approximately 10%. Further, a time shift of $\Delta t^* = 0.36$ is found between both peaks. The smaller peak emission rate is compensated for by a moderate overestimation of the emission rate at $t^* \approx 9 \ldots 11$ as the difference in the total amount of pollutant emitted is only 1.6% using either the noise free measurements or the noisy measurements.

Next, the simultaneous release of two Gaussian-shaped emissions from Doel 3 and the leaking tank is studied. In Fig. 6.8a, the resulting non-dimensional concentration profiles c^* observed at M1 and M2 as function of the non-dimensional time t^* is shown. It is observed that the reconstructed profiles are almost perfectly overlapping and closely match the noise-free measurements. The effect of the addition of random noise to the measurements is again negligible.

The time evolution of the non-dimensional reconstructed source σ_1^* from Doel 3 is shown in Fig. 6.8b. The profile fits acceptably well with the Gaussian profile for both the noise free and noisy measurements. The largest differences are found at peak emission rate, which is underestimated by 9.3%, and in the tail of the emission at $t^* \approx 7.5$. These are compensated for by an increased emission rate from the leaking tank at $t^* \approx 4$ and a decreased emission rate at $t \approx 8$, as shown in Fig. 6.8c. Although the reconstructed profile fits the true profile less well compared to the emission from Doel 3, the correspondence is satisfactory. Furthermore, the difference in total amount of pollutant emitted between the true emission and the reconstructed emission is 1.1% for Doel 3 and 0.34% for the tank when using noise-free measurements, and 2.8% for Doel 3 and 1.1% for the tank when using noisy measurements. Hence, despite the deviation is emission profiles, the total amount of pollutant emitted is predicted accurately by the reconstruction.

Finally, we consider the emission of a pollutant from a source location not taken into account in the forward ROMs. More specifically, the measurements are generated using an Gaussian-shaped emission from Doel 4 but only the chimney of Doel 3 and the leaking tank are regarded as possible sources. When inspecting the reconstructed concentration profiles for locations M5 and M6 in Fig. 6.9a, the measurement locations with the largest measured values, a large deviation with measurements is observed. Neither the magnitude nor the timing matches with the measurements. The reconstructed source profile from Doel 3 is shown in Fig. 6.9b. A strongly fluctuating and unphysical profile is found with a large negative peak at $t^* \approx 5$. Also the emission profile for the leaking tank shows these large fluctuations with large negative values (Fig. 6.9c). Furthermore, both source profiles show an almost perfectly inverted behaviour with a small time shift, i.e. both sources attempt to cancel each other out

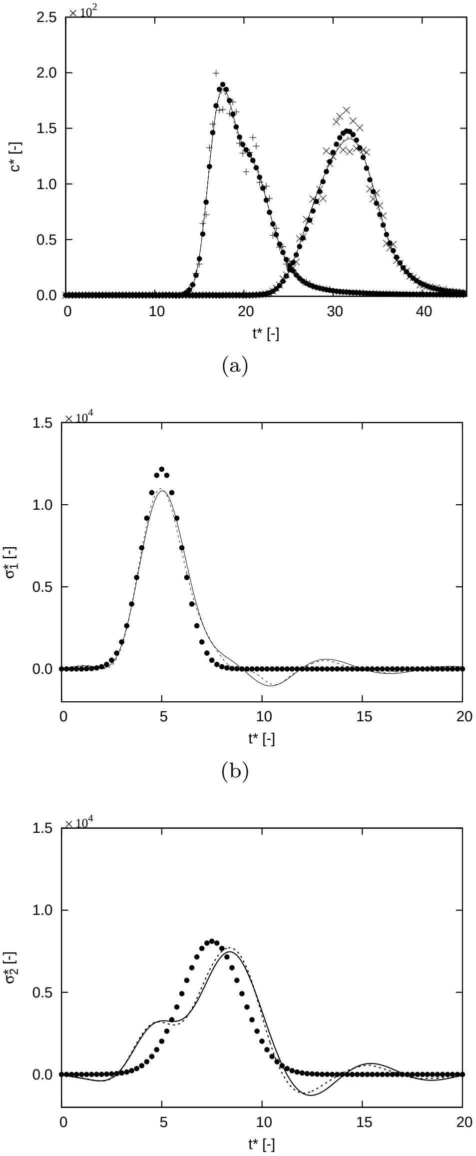

(a)

(b)

(c)

Figure 6.8: Profiles of the non-dimensional concentration $c^*(= cUL^2/R)$ (a), and the non-dimensional source $\sigma_i^*(= \sigma_i L^3/R)$ from Doel 3 (b), and from the leaking tank (c). Symbols: (●): Noise-free measurement; (+): Noisy measurement ($\alpha = 0.2$) at M1; (×): Noisy measurement ($\alpha = 0.2$) at M2. Lines: (—): Reconstructed profile using noise-free measurements; (−−): Reconstructed profile using noisy measurements.

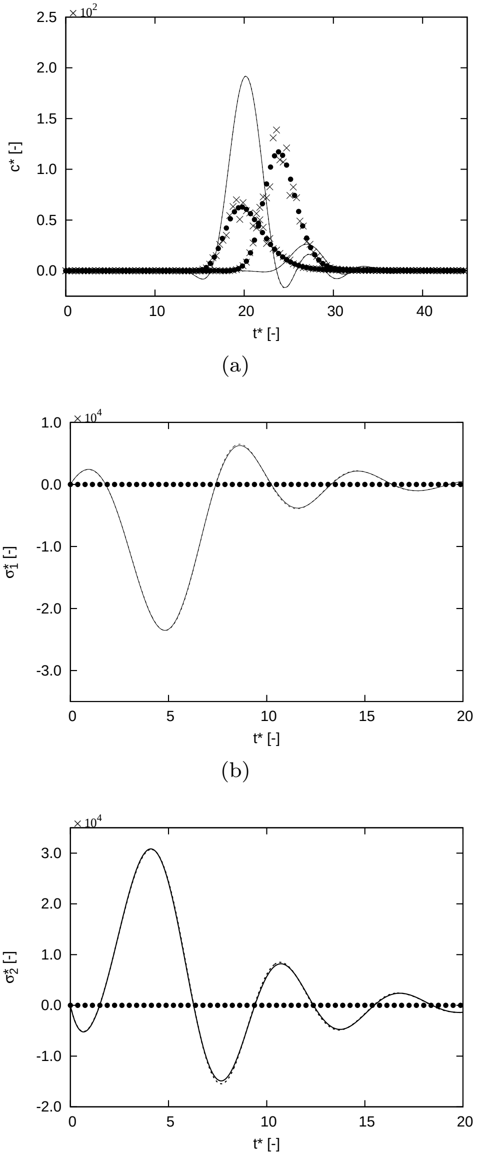

(a)

(b)

(c)

Figure 6.9: Profiles of the non-dimensional concentration $c^* (= cUL^2/R)$ (a), and the non-dimensional source $\sigma_i^* (= \sigma_i L^3/R)$ from Doel 3 (b), and from the leaking tank (c). Symbols: (●): Noise-free measurement; (+): Noisy measurement ($\alpha = 0.2$) at M5; (×): Noisy measurement ($\alpha = 0.2$) at M6. Lines: (—): Reconstructed profile using noise-free measurements; (−−): Reconstructed profile using noisy measurements.

with large negative values. This shows that it is of prime importance that all possible sources are included in the set $1 \ldots S$ of the forward ROMs. If this is not the case, unphysical signals are found characterized by large fluctuations and large negative source values.

6.5 Conclusion

In the current chapter, a fast method for the reconstruction of transient, multi-source emissions based on CFD modeling and near-range measurements, is elaborated. To this end, the problem of the source reconstruction is formulated as a regularized least squares problem comparing the measurements to model predictions. Regularization is added to the cost functional in order to obtain a well-posed problem by penalization of the non-compactness and the magnitude of the rate of change of the source. The transient three-dimensional advection-diffusion problem is used to link the source to the concentration in the domain. Moreover, by limiting the possible source locations to a finite number of possibilities, a Krylov-subspace projection-based model reduction method using the Arnoldi algorithm can be applied. The size of the resulting system is reduced to such extent that the optimal solution can be found in one step by directly solving the coupled optimality conditions. Using default tools provided by Petsc library, only a few minutes are required to obtain the optimal prediction of the sources.

To assess the approach, three cases of a time-dependent pollutant emission at the Doel Nuclear Power Station are considered. For each case, a set of artificial measurements is constructed by sampling the local pollutant concentration during a forward simulation using the full CFD model. In order to test the robustness of the methodology, 20% noise is added to these measurements. The set of artificial measurements are thus used as input for the source reconstruction methodology, and reconstructed sources are compared to the original sources.

When considering a single source, the simulation shows that the time evolution of the source can be reconstructed to a high level of accuracy. Also when considering multiple possible sources, the emission profiles match well with the profiles imposed. No significant differences in emission profiles were found between the reconstructions using the noise-free and noisy measurements. Furthermore, the estimated total amount of pollutant emitted differed no more than 2.8% for the cases considered. The methodology has therefore shown to be a robust method for the source estimation of one or multiple possible sources from measurements.

In the current work, the regularization strength is determined through knowledge of the true source profile. In general, this profile is not known as this is the purpose of the source reconstruction. It might therefore be interesting to consider alternative methods to the L-curve approach such as the Generalized Cross Validation approach (see, e.g., Ref. [52]). Further, we illustrated the importance of including all possible sources in the set of the forward ROMs. The initialization cost of a ROM however, is non-negligible. Therefore, for sources in the vicinity of each other, it might be interesting to consider parametric model order reduction (see, e.g., Ref. [96]). Also for the extension towards multiple wind directions, this might be interesting to consider. Finally, the adjoint formulation can serve as an interesting starting point for the optimization of the measurement locations.

Chapter 7

Conclusions and suggestions for future research

7.1 Conclusions

In the current dissertation, near-range atmospheric dispersion modeling using CFD was investigated in the framework of nuclear emergency preparedness and response. Computational Fluid Dynamics (CFD) simulations were preformed using both RANS turbulence modeling and LES turbulence modeling. Following an Eulerian approach for the simulation a non-buoyant, non-reactive gas in a thermally neutral atmospheric boundary layer, both dispersion cases in an open field as well as in the built environment were studied. This effort resulted in new insights and the development new models and techniques.

We introduced a simple approach to estimate, based on experiments, the correct level of variability in wind direction that is required for Reynolds-averaged simulations of pollutant dispersion in the atmosphere. In these simulations, fluctuations in wind directions are already partly accounted for by the modeled turbulence; and hence, the effective variability that should be used as a boundary condition to the simulations, needs to be lower than experimentally measured. Based on this rationale, and the turbulence level in the simulation, it is now possible to estimate the required 'external' variability. To assess the approach, we performed a series of numerical simulations covering 45 of the Prairie Grass experiments [10], i.e. 24 characterized by stable conditions, 15 characterized by neutral conditions, and 6 characterized by unstable conditions. Four different models were compared, i.e., (1) a Gaussian model, and RANS simulations, either using (2) only the mean wind direction ('mean-wind' RANS), (3) using the full wind-direction variability as observed in the experiment ('σ_α–RANS'), or (4) using a reduced level of variability ('σ_e–RANS'). We found that including wind variability significantly improves predictions over 'mean-wind' RANS models, and the Gaussian model. However, when using the full range of variability measured in experiments ('σ_α–RANS') lateral plume spreading is overpredicted. Reducing the variability by removing what is already represented in the RANS turbulence model, leads to a significant improvement of predictions. To further quantify this, we employed the model performance criteria of Chang and Hanna [30], and found that the 'σ_e–RANS' simulations are the only ones that meet all acceptance levels in the case of neutral atmospheric conditions. In the case of stable and unstable stratification, we found that the model is well capable of reproducing the centerline concentrations, meeting the model performance criteria regardless the stratification. When taking the off-centerline measurements into account, the model reproduces the high concentrations without a significant bias or scatter and improves the prediction of the lower concentrations compared to the 'mean-wind RANS' and 'σ_α–RANS' simulations.

A time-dependent dispersion model for the near-range dispersion of radioactive gases in a thermally neutral atmospheric boundary layer was developed. To this end, a CFD model using LES turbulence modeling is coupled with a gamma dose rate model based on the point-kernel method with buildup factors. The variability of the gamma fluence rate at ground level was assessed by performing a set of time-dependent simulations of a constant release of a radioactive gas into an open field. Four different release heights were considered in this study as well as two different isotopes, i.e. ^{41}Ar emitting a high energy gamma and ^{133}Xe emitting a low energy gamma. The simulations demonstrated that even with the very simple setup of the open field, a large variation in dose rate from beta radiation is observed, causing peaks in the dose rate of several orders of magnitude. Furthermore, also a strongly fluctuating gamma fluence rate with a clear lower and upper bound was observed at ground level. At a distance of approximately fifteen times the release height, the variability for both concentration and gamma fluence rate was found to be the highest, regardless of the release height or the gamma energy. Note that this observation is only valid for the current simple release geometry and neutral atmospheric stratification. For high energy gammas of ^{41}Ar, the spread on the observations is not affected by the release height while this is the case for low energy gammas of ^{133}Xe. For both cases, this spread can be reduced effectively by performing time-averaging. However, it is illustrated that neglecting this variability can result in errors up to a factor of four on the dose estimation when long-term measurements are used to estimate the resulting dose from short-term exposures. In addition, the results indicate that the gamma dose measurements from nearby sensors cannot be used to accurately estimate the dose from beta radiation. This information can be particularly useful in uncertainty quantification studies and for the optimization of measurement strategies.

A reduced order modeling method was introduced which allows to simulate the dispersion of a pollutant in a built environment faster than real-time. A Krylov-subspace projection-based model reduction method using the Arnoldi algorithm is applied for a CFD model. The method results in a stable ROM, and the algorithm is formulated in such a way that it can be used with any choice of CFD solver. We simulate the pollutant dispersion using an Eulerian approach where the concentration is formulated as a transient three-dimensional advection-diffusion problem on a steady velocity background. Three cases of a time-dependent pollutant emission were simulated using both the CFD and the ROM to assess the approach. The Doel Nuclear Power Station was selected as the subject of the study. The simulations show that for all of the cases, the ROM is well capable of reconstructing both the shape and the magnitude of the pollutant concentration without significant loss in accuracy. In addition, it is illustrated that increasing the order of the ROM, further increases the accuracy, i.e. the ROM converges towards the CFD model. After initialization, the application of this method resulted in the reduction of the computational time by a factor of 2500, running 25 times faster than real-time, including a possible dose assessment. Furthermore, when the computational cost is looked at, the reduction was more than a factor of 10^5. It is therefore clear that the ROM enables for fast dose assessment after the emission of a radioactive gas.

Further, a method for the fast reconstruction of transient, multi-source emissions based on CFD modeling and near-range measurements is elaborated. The problem of the source reconstruction is formulated as a regularised least squares problem comparing the measurements to model predictions. Regularisation is added to the cost functional in order to obtain a well-posed problem by penalisation of the non-compactness and the magnitude of the rate of change of the source. The transient three-dimensional advection-diffusion problem is used to link the source to the concentration in the domain. Moreover, by limiting the possible source locations to a finite number of possibilities, a Krylov-subspace projection-based model reduction method using the Arnoldi algorithm can be applied. The size of the resulting system is reduced to such extent that the optimal solution can be found in one step by directly solving the coupled optimality conditions. Using default tools provided by Petsc library, only a few minutes are required to obtain the optimal prediction of the sources. To assess the approach, three cases of a time-dependent pollutant emission at the Doel Nuclear Power Station are considered. For each case, a set of artificial measurements are constructed by sampling the local pollutant concentration during a forward simulation using the full CFD model. In order to test the robustness of the methodology, 20% noise is added to these measurements. The set of artificial measurements are thus used as input for the source reconstruction methodology, and reconstructed sources are compared to the original sources. When considering a single source, the simulation shows that the time evolution of the source can be reconstructed to a high level of accuracy. Also when considering multiple possible sources, the emission profiles match well with the profiles imposed. No significant differences in emission profiles were found between the reconstructions using the noise-free and noisy measurements. Furthermore, the estimated total amount of pollutant emitted differed no more than 2.8% for the cases considered. The methodology has therefore shown to be a robust method for the source estimation of one or multiple possible sources from measurements.

In summary, the current dissertation demonstrates the large potential of CFD in the framework of nuclear emergency preparedness and response. With the development of a fast model for the time-dependent pollutant dispersion simulation in the built environment, and the development of a model for fast pollutant source reconstruction based on time-dependent near-range measurements, it has been demonstrated that accurate forward and backward near-range dispersion models can be derived with a run time comparable to Gaussian or Lagrangian models. In addition, the accuracy of near-range atmospheric dispersion simulations using RANS was improved and the variability of radiological dose rate from cloud shine due to instantaneous turbulent mixing processes was examined through LESs. Finally, the new insights, models and techniques developed in this dissertation, establish a firm foundation for future research.

7.2 Future research challenges

The current dissertation presented several aspects of near-range atmospheric dispersion simulations using CFD in the framework of nuclear emergency preparedness and response. Nevertheless, many challenges remain before these can be used for on-line risk management tools. First of all, the current work was mostly limited to neutral thermal stratification. However, an extension towards non-neutral stratification of the ABL is indispensable for practical application since thermal stratification of the atmospheric boundary layer can have an important influence on the dispersion. In addition, when LES turbulence modeling is used, such an extension would also allow to extend the study on the variability of the dose rate from cloud shine to non-neutral stratification. For instance, stable stratification suppresses turbulence and, as a result, the variability of the dose rate is expected to decrease. The opposite is true for a convective boundary layer.

The reduced order modeling of the radioactive pollutant dispersion at the near-range opens new doors for research and applications in the preparedness and response phases of nuclear emergencies. Before an on-line monitoring system can be set up however, a number of research topics need to be addressed. In the current work, a ROM is constructed for the dispersion of a non-buoyant, non-reactive gas in a steady, thermally neutral boundary layer for one wind direction only. This is very limiting for the applicability of the model. In case of the occurrence of buoyancy effects due to a temperature difference between the ambient air and the gas emitted, the can be addressed by estimating an effective emission height using plume rise models (see, e.g., Ref. [75]). A non-zero emission velocity can be accounted for in a similar way. However, a direct handling in the CFD model is preferred. Extending the ROM to the dispersion of gases with significantly higher density than air remains a challenge due to the strong, non-linear coupling with the momentum equation. Further, a significant part of the initialization cost of the ROM is related to the simulation of the background velocity field. A reduction of the initialization cost of the ROM can therefore be obtained by a faster evaluation of the velocity field. Consequently, model order reduction of the velocity field can be useful to investigate. For the extension towards multiple wind directions, it might be interesting to consider parametric model order reduction (see, e.g., Ref. [96]). Also the automated selection of a suitable order of the ROM remains challenging (see, e.g., Ref. [115] and Ref. [12]). For the automated selection of the regularisation strength in cost functional of the source reconstruction problem, it might be worth investigating alternative methods to the L-curve approach such as the Generalized Cross Validation approach (see, e.g., Ref [52]). Handling source locations not taken into account in the forward ROMs remains an open question as well. Further, the inverse modeling can serve as an interesting starting point for the optimization of the measurement locations.

Finally, the experimental validation of the model will be key to convince the CFD and nuclear community of the proper operation of the model. The collection of a high quality data set is in this context essential. The releases of small but measurable quantities of radionuclides from existing nuclear installations can be used to create such a data set. Particularly interesting is that release quantities are usually well known and existing fence monitoring around these installations gives continuously data on radionuclide fluency rates and/or dose rates. Such a data set will be unique for the international community to test atmospheric dose and dispersion models at the near-range.

Appendix A

Derivation of the optimality condition

As introduced in section 6.1, the source reconstruction problem can be formulated as the following regularised least-squares minimisation problem

$$\min_{(c,\sigma,\boldsymbol{y})} \mathcal{J}(c,\sigma,\boldsymbol{y}) \tag{A.1}$$

subject to

$$\begin{cases} \dfrac{\partial c}{\partial t} + \nabla \cdot \langle \boldsymbol{u} \rangle c - \nabla \cdot \dfrac{\nu_t}{Sc_t} \nabla c & = \sigma \qquad \text{in } \Omega \times (0,T] \\ y_i & = f_i(c) \qquad \text{in } (0,T] \text{ for } i = 1 \dots M \end{cases} \tag{A.2}$$

The Lagrangian for this problem is constructed by introduction of the Lagrange multipliers $\varsigma(\boldsymbol{x},t)$ and $\varphi_i(t)$, leading to

$$\begin{aligned} \mathcal{L}(c,\sigma,\boldsymbol{y},\varsigma,\boldsymbol{\varphi}) = \frac{1}{2} \int_0^T \sum_{i=1}^{M} (y_i - \hat{y}_i)^2 \, dt + \frac{\beta}{2} \int_0^T \int_\Omega \sigma^2 d\Omega dt + \\ \frac{\gamma}{2} \int_0^T \int_\Omega \left(\frac{\partial \sigma}{\partial t} \right)^2 d\Omega dt + \int_0^T \int_\Omega \left(\frac{\partial c}{\partial t} + \nabla \cdot \langle \boldsymbol{u} \rangle c - \nabla \cdot \frac{v_t}{Sc_t} \nabla c - \sigma \right) \varsigma d\Omega dt + \\ \sum_{i=1}^{M} \int_0^T \left(-y_i + f_i \right) \varphi_i dt, \end{aligned} \tag{A.3}$$

where $\boldsymbol{\varphi} = [\varphi_1 \varphi_2 \dots \varphi_M]$. We presume that $f_i(c) = \int_\Omega \psi_i(\boldsymbol{x}) c(\boldsymbol{x}) d\Omega$. Since (A.1–A.2) is a convex problem, the optimal solution is found for $\nabla \mathcal{J}(c, \sigma, \boldsymbol{y}) = 0$. This condition is met if the variation of the Lagrangian $\mathcal{L}$ with respect to each of its variables is equal to zero. The latter is subsequently used to derive the optimality conditions.

- By imposing that for any variation δc the Gateaux differential $\mathcal{L}_c(\delta c) \equiv \frac{\mathrm{d}}{\mathrm{d}\alpha} \mathcal{L}(c + \alpha \delta c, \sigma, \boldsymbol{y}, \varsigma, \boldsymbol{\varphi})|_{\alpha=0} = 0$, we obtain

  $$0 = \int_0^T \int_\Omega \left(\frac{\partial \delta c}{\partial t} + \nabla \cdot \langle \boldsymbol{u} \rangle \delta c - \nabla \cdot \frac{v_t}{Sc_t} \nabla \delta c \right) \varsigma d\Omega dt + \sum_{i=1}^{M} \int_0^T \int_\Omega \psi_i \varphi_i \delta c d\Omega dt, \quad \text{(A.4)}$$

  which can be reformulated by applying integration by parts as

  $$0 = \int_0^T \int_\Omega \left(-\frac{\partial \varsigma}{\partial t} - \nabla \cdot \langle \boldsymbol{u} \rangle \varsigma - \nabla \cdot \frac{v_t}{Sc_t} \nabla \varsigma + \sum_{i=1}^{M} \psi_i \varphi_i \right) \delta c d\Omega dt + \int_\Omega \left[\varphi_i \delta c \right]_0^T d\Omega - \int_0^T \int_{\partial\Omega} \delta c \, \varsigma \langle \boldsymbol{u} \rangle \cdot \boldsymbol{n} dS dt + \int_0^T \int_{\partial\Omega} \delta c \frac{v_t}{Sc_t} \nabla \varsigma \cdot \boldsymbol{n} dS dt - \int_0^T \int_{\partial\Omega} \varsigma \frac{v_t}{Sc_t} \nabla \delta c \cdot \boldsymbol{n} dS dt, \quad \text{(A.5)}$$

  where $\boldsymbol{n}$ is the normal to the outer surface, and $\partial\Omega$ is the surface area. This equation can only hold for any variation δc if

  $$-\frac{\partial \varsigma}{\partial t} - \nabla \cdot \langle \boldsymbol{u} \rangle \varsigma - \nabla \cdot \frac{v_t}{Sc_t} \nabla \varsigma + \sum_{i=1}^{M} \psi_i \varphi_i = 0, \quad \text{(A.6)}$$

  the final condition is set to

  $$\varsigma(T) = 0, \quad \text{(A.7)}$$

  and if the boundary conditions for ς are set to $\varsigma(\partial\Omega_{outlet}) = 0$ and Neumann conditions at the other surfaces.

- The forward transport equation is reproduced from $\mathcal{L}_\varsigma(\delta \varsigma) = 0$, i.e.

  $$\int_0^T \int_\Omega \left(\frac{\partial c}{\partial t} + \nabla \cdot \langle \boldsymbol{u} \rangle c - \nabla \cdot \frac{v_t}{Sc_t} \nabla c - \sigma \right) \delta \varsigma d\Omega dt = 0. \quad \text{(A.8)}$$

This can only be zero for any $\delta\varsigma$ if

$$\frac{\partial c}{\partial t} + \nabla \cdot \langle \boldsymbol{u} \rangle c - \nabla \cdot \frac{v_t}{Sc_t} \nabla c = \sigma. \tag{A.9}$$

- The source can be related to the adjoint concentration by taking the variance with respect to σ, i.e. $\mathcal{L}_\sigma(\delta\sigma) = 0$ or

$$0 = \int_0^T \int_\Omega (\beta\sigma - \varsigma)\, \delta\sigma + \gamma \frac{\partial \sigma}{\partial t} \frac{\mathrm{d}\delta\sigma}{\mathrm{d}t} d\Omega dt \tag{A.10}$$

$$= \int_0^T \int_\Omega \left(\beta\sigma - \varsigma + \gamma \frac{\partial^2 \sigma}{\partial t^2} \right) \delta\sigma d\Omega dt + \int_\Omega \left[\frac{\partial \sigma}{\partial t} \delta\sigma \right]_0^T d\Omega. \tag{A.11}$$

Therefore,

$$\beta\sigma + \gamma \frac{\partial^2 \sigma}{\partial t^2} - \varsigma = 0, \tag{A.12}$$

with initial and final conditions

$$\frac{\partial \sigma}{\partial t}(0) = 0, \qquad \frac{\partial \sigma}{\partial t}(T) = 0. \tag{A.13}$$

- The relation between the local measurements y_i and concentration is derived from $\mathcal{L}_{y_i}(\delta y_i) = 0$ for every location i in the domain

$$\int_0^T (y_i + \alpha\delta y_i - \hat{y}_i - \varphi_i)\delta y_i dt = 0, \tag{A.14}$$

and therefore

$$\varphi_i = y_i - \hat{y}_i. \tag{A.15}$$

- Finally, $\mathcal{L}_{\varphi_i}(\delta\varphi_i) = 0$ for every φ_i in $\boldsymbol{\varphi}$ from which it follows that

$$\int_0^T (-y_i + f_i)\delta\varphi_i d\Omega dt = 0. \tag{A.16}$$

This can only be true for every $\delta\varphi_i$ if

$$y_i = f_i(c) \tag{A.17}$$

Variables φ_i and y_i can be eliminated by substitution of Eqs. (A.15), and (A.17) into Eq. (A.6). Therefore, the first-order optimality is reached when (boundary conditions for c included)

$$\frac{\partial c}{\partial t} + \nabla \cdot \langle \boldsymbol{u} \rangle c - \nabla \cdot \frac{v_t}{Sc_t} \nabla c = \sigma \tag{A.18a}$$

$$-\frac{\partial \varsigma}{\partial t} - \nabla \cdot \langle \boldsymbol{u} \rangle \varsigma - \nabla \cdot \frac{v_t}{Sc_t} \nabla \varsigma = \sum_{i=1}^{M} \psi_i (\hat{y}_i - f_i) \tag{A.18b}$$

$$\beta \sigma + \gamma \frac{\partial^2 \sigma}{\partial t^2} - \varsigma = 0, \tag{A.18c}$$

with initial conditions

$$c(0) = 0, \qquad \frac{\partial \sigma}{\partial t}(0) = 0, \tag{A.19}$$

final conditions

$$\varsigma(T) = 0, \qquad \frac{\partial \sigma}{\partial t}(T) = 0, \tag{A.20}$$

and boundary conditions

$$c(\partial \Omega_{inlet}) = 0, \qquad \varsigma(\partial \Omega_{outlet}) = 0. \tag{A.21}$$

At the other boundaries, Neumann boundary conditions apply to c and ς.

Bibliography

[1] Mahdi Abkar and Fernando Porté-Agel. The effect of atmospheric stability on wind-turbine wakes: A large-eddy simulation study. In *Journal of Physics: Conference Series*, volume 524, page 012138. IOP Publishing, 2014.

[2] Volkan Akçelik, George Biros, Omar Ghattas, Kevin R Long, and Bart van Bloemen Waanders. A variational finite element method for source inversion for convective–diffusive transport. *Finite Elements in Analysis and Design*, 39(8):683–705, 2003.

[3] David Amsallem and Charbel Farhat. Stabilization of projection-based reduced-order models. *International Journal for Numerical Methods in Engineering*, 91(4):358–377, 2012.

[4] Spyros Andronopoulos, Efstratios Davakis, and J Bartzis. RODOS-DIPCOT Model Description and Evaluation. Technical report, Report RODOS (RA2)-TN (09), 2009.

[5] American Nuclear Society. Working Group ANS-6.4.3 and American National Standards Institute. *American National Standard for Gamma-ray Attenuation Coefficients and Buildup Factors for Engineering Materials.* ANSI/ANS. The Society, 1992.

[6] Athanasios C Antoulas, Danny C Sorensen, and Serkan Gugercin. A survey of model reduction methods for large-scale systems. *Contemporary mathematics*, 280:193–220, 2001.

[7] Satish Balay, Shrirang Abhyankar, Mark F. Adams, Jed Brown, Peter Brune, Kris Buschelman, Victor Eijkhout, William D. Gropp, Dinesh Kaushik, Matthew G. Knepley, Lois Curfman McInnes, Karl Rupp, Barry F. Smith, and Hong Zhang. PETSc Users Manual. Technical Report ANL-95/11 - Revision 3.5, Argonne National Laboratory, 2014.

[8] Satish Balay, Shrirang Abhyankar, Mark F. Adams, Jed Brown, Peter Brune, Kris Buschelman, Victor Eijkhout, William D. Gropp, Dinesh Kaushik, Matthew G. Knepley, Lois Curfman McInnes, Karl Rupp, Barry F. Smith, and Hong Zhang. PETSc Web page. `http://www.mcs.anl.gov/petsc`, 2014.

[9] Satish Balay, William D. Gropp, Lois Curfman McInnes, and Barry F. Smith. Efficient Management of Parallelism in Object Oriented Numerical Software Libraries. In E. Arge, A. M. Bruaset, and H. P. Langtangen, editors, *Modern Software Tools in Scientific Computing*, pages 163–202. Birkhäuser Press, 1997.

[10] M. L. Barad, editor. *Project Prairie Grass, A Field Program In Diffusion. Geophysical Research Paper, No. 59, Vol I and Vol II.* Air Force Cambridge Research Center, 1958.

[11] Ulrike Baur, Peter Benner, and Lihong Feng. Model order reduction for linear and nonlinear systems: a system-theoretic perspective. *Archives of Computational Methods in Engineering*, 21(4):331–358, 2014.

[12] MA Bazaz, S Janardhanan, et al. A stopping criterion for Krylov-subspace based model order reduction techniques. In *Modelling, Identification & Control (ICMIC), 2012 Proceedings of International Conference on*, pages 921–925. IEEE, 2012.

[13] M M Be, V Chiste, C Dulieu, E Browne, V Chechev, N Kuzmenko, F G Kondev, A Luca, M Galan, A Pearce, and X Huang. *Table of radionuclides (Vol 4 - A = 133 to 252).* Editions BIPM, 2008.

[14] M M Be, V Chiste, C Dulieu, E Browne, V Chechev, N Kuzmenko, F G Kondev, A Luca, M Galan, A Pearce, and X Huang. *Table of radionuclides (Vol. 6 - A = 22 to 242).* Editions BIPM, 2011.

[15] R Bellasio and M Tamponi. MDGP: a new Eulerian 3D unsteady state model for heavy gas dispersion. *Atmospheric Environment*, 28(9):1633–1643, 1994.

[16] R Bird, W Stewart, and E Lightfoot. *Transport Phenomena*, volume vol 2. New York: Wiley, 2006.

[17] B Blocken, T Stathopoulos, P Saathoff, and X Wang. Numerical evaluation of pollutant dispersion in the built environment: comparisons between models and experiments. *Journal of Wind Engineering and Industrial Aerodynamics*, 96(10):1817–1831, 2008.

[18] B Blocken, Y Tominaga, and T Stathopoulos. CFD simulation of micro-scale pollutant dispersion in the built environment. *Building and Environment*, 64:225–230, 2013.

[19] Bert Blocken, Ted Stathopoulos, and Jan Carmeliet. CFD simulation of the atmospheric boundary layer: wall function problems. *Atmospheric environment*, 41(2):238–252, 2007.

[20] Carlos Borrego and Eberhard E Renner. *Air pollution modeling and its application XVIII*, volume 6. Elsevier, 2011.

[21] Elie Bou-Zeid, Charles Meneveau, and Marc Parlange. A scale-dependent Lagrangian dynamic model for large eddy simulation of complex turbulent flows. *Physics of Fluids (1994-present)*, 17(2):025105, 2005.

[22] G.A. Briggs, United States. Air Resources Atmospheric Turbulence, and Diffusion Laboratory. *Diffusion Estimation for Small Emissions*. NOAA, 1973.

[23] Jean-Pierre Brunel. Estimation of sensible heat flux from measurements of surface radiative temperature and air temperature at two meters: application to determine actual evaporation rate. *Agricultural and forest meteorology*, 46(3):179–191, 1989.

[24] H Bultynck and LM Malet. Evaluation of atmospheric dilution factors for effluents diffused from an elevated continuous point source. *Tellus A*, 24(5), 1972.

[25] Joost A Businger, John C Wyngaard, Y Izumi, and Edward F Bradley. Flux-profile relationships in the atmospheric surface layer. *Journal of the atmospheric Sciences*, 28(2):181–189, 1971.

[26] Johan Camps, Catrinel Turcanu, Damien Braekers, Benny Carlé, Geert Olyslaegers, Johan Paridaens, Carlos Rojas Palma, and Klaas van der Meer. The ‘NOODPLAN’ early phase nuclear emergency models: an evaluation. In *Proceedings of Third European IRPA Congress 2010 June 14-18, Helsinki, Finland*, 2010.

[27] DJ Carruthers, RJ Holroyd, JCR Hunt, WS Weng, AG Robins, DD Apsley, DJ Thompson, and FB Smith. UK-ADMS: A new approach to modelling dispersion in the earth’s atmospheric boundary layer. *Journal of wind engineering and industrial aerodynamics*, 52:139–153, 1994.

[28] Marcelo Chamecki, Charles Meneveau, and Marc B Parlange. Large eddy simulation of pollen transport in the atmospheric boundary layer. *Journal of Aerosol Science*, 40(3):241–255, 2009.

[29] ST Chan, DL Ermak, and LK Morris. FEM3 model simulations of selected Thorney Island phase I trials. *Journal of hazardous materials*, 16:267–292, 1987.

[30] J C Chang and S R Hanna. Air quality model performance evaluation. *Meteorology and Atmospheric Physics*, 87(1-3):167–196, 2004.

[31] Mauricio Chavez, Bodhisatta Hajra, Ted Stathopoulos, and Ali Bahloul. Near-field pollutant dispersion in the built environment by CFD and wind tunnel simulations. *Journal of Wind Engineering and Industrial Aerodynamics*, 99(4):330–339, 2011.

[32] Arthur B Chilton, J Kenneth Shultis, and Richard E Faw. *Principles of radiation shielding.* Prentice-Hall, 1984.

[33] Fotini Katopodes Chow, Branko Kosovic, and Stevens Chan. Source inversion for contaminant plume dispersion in urban environments using building-resolving simulations. *Journal of applied meteorology and climatology*, 47(6):1553–1572, 2008.

[34] Chia-Chi Chu, Ming-Hong Lai, and Wu-Shiung Feng. Model-order reductions for MIMO systems using global Krylov subspace methods. *Mathematics and computers in Simulation*, 79(4):1153–1164, 2008.

[35] Alan J Cimorelli, Steven G Perry, Akula Venkatram, Jeffrey C Weil, Robert J Paine, Robert B Wilson, Russell F Lee, Warren D Peters, Roger W Brode, and James O Paumier. AERMOD–Description of model formulation. Technical Report EPA-454/R-03-004, United States Environmental Protection Agency, 2004.

[36] John R Cooper, Keith Randle, and Ranjeet S Sokhi. *Radioactive releases in the environment: impact and assessment.* John Wiley & Sons, 2003.

[37] Paulo AB de Sampaio, Milton AG Junior, and Celso MF Lapa. A CFD approach to the atmospheric dispersion of radionuclides in the vicinity of NPPs. *Nuclear Engineering and Design*, 238(1):250–273, 2008.

[38] E Demael and B Carissimo. Comparative evaluation of an Eulerian CFD and Gaussian plume models based on prairie grass dispersion experiment. *Journal of Applied Meteorology and Climatology*, 47(3):888–900, 2008.

[39] Juliana P Duarte, Paulo Fernando F Frutuoso e Mel, Antonio Sérgio M Alves, and Erivaldo Mario dos Passos. Atmospheric Dispersion and dose Evaluation Due to the Fall of a Radioactive Package at a LILW Facility. *International Journal of Energy Engineering*, 3(3):119–126, 2013.

[40] T Duranova, W Raskob, R Mustonen, and T Schneider. Strategic Research Agenda of the NERIS Platform. Technical report, European Platform on Preparedness for Nuclear and Radiological Emergency Response and Recovery, April 8, 2014.

[41] AJ Dyer. A review of flux-profile relationships. *Boundary-Layer Meteorology*, 7(3):363–372, 1974.

[42] Paul W Eslinger, SR Biegalski, Ted W Bowyer, Matthew W Cooper, Derek A Haas, James C Hayes, Ian Hoffman, E Korpach, Jing Yi, Harry S Miley, et al. Source term estimation of radioxenon released from the Fukushima Dai-ichi nuclear reactors using measured air concentrations and atmospheric transport modeling. *Journal of environmental radioactivity*, 127:127–132, 2014.

[43] Jes Fenger and F Palmgren. *Urban air pollution-European aspects*, volume 1. Springer Science & Business Media, 1998.

[44] Thomas K Flesch, Lowry A Harper, Raymond L Desjardins, Zhiling Gao, and Brian P Crenna. Multi-source emission determination using an inverse-dispersion technique. *Boundary-layer meteorology*, 132(1):11–30, 2009.

[45] Thomas Foken. 50 years of the Monin–Obukhov similarity theory. *Boundary-Layer Meteorology*, 119(3):431–447, 2006.

[46] Federal Agency for Nuclear Control. Telerad - FANC|AFCN.

[47] Jörg Franke, Antti Hellsten, Heinke Schlünzen, and Bertrand Carissimo. *Best practice guideline for the CFD simulation of flows in the urban environment*. 2007.

[48] Roland W Freund. Model reduction methods based on Krylov subspaces. *Acta Numerica*, 12:267–319, 2003.

[49] Vladimír Fuka and Josef Brechler. Large eddy simulation modelling of the dispersion of radioactive particulate matter. *International Journal of Environment and Pollution*, 48(1):156–163, 2012.

[50] Eduardo F Gallego Díaz, Ruben Barbero, Daniel Cuadra, Jeronimo Domingo, and Alfredo Iranzo. Modelling with a CFD code the near-range

dispersion of particles unexpectedly released from a nuclear power plant. In *Proc. 3rd European IRPA Congress (Helsinki)*, pages 14–8, 2010.

[51] JR Garratt and RA Pielke. On the sensitivity of mesoscale models to surface-layer parameterization constants. *Boundary-layer meteorology*, 48(4):377–387, 1989.

[52] Gene H Golub, Michael Heath, and Grace Wahba. Generalized cross-validation as a method for choosing a good ridge parameter. *Technometrics*, 21(2):215–223, 1979.

[53] Pierre Gousseau, B Blocken, T Stathopoulos, and GJF Van Heijst. CFD simulation of near-field pollutant dispersion on a high-resolution grid: a case study by LES and RANS for a building group in downtown Montreal. *Atmospheric Environment*, 45(2):428–438, 2011.

[54] Akshay A Gowardhan, Eric R Pardyjak, Inanc Senocak, and Michael J Brown. A CFD-based wind solver for an urban fast response transport and dispersion model. *Environmental fluid mechanics*, 11(5):439–464, 2011.

[55] J Graham. *Fast Reactor Safety*. Elsevier, 2012.

[56] Christophe Gueibe, Lieven Vervecken, and Johan Camps. Intercomparison of dose rate calculations from atmospheric dispersion models in the near range. In *NERIS Workshop*, Milan, 2015.

[57] Shaodong Guo, Rui Yang, Hui Zhang, Wenguo Weng, and Weicheng Fan. Source identification for unsteady atmospheric dispersion of hazardous materials using Markov Chain Monte Carlo method. *International Journal of Heat and Mass Transfer*, 52(17):3955–3962, 2009.

[58] Jian Hang, Yuguo Li, Mats Sandberg, Riccardo Buccolieri, and Silvana Di Sabatino. The influence of building height variability on pollutant dispersion and pedestrian ventilation in idealized high-rise urban areas. *Building and Environment*, 56:346–360, 2012.

[59] Steven R Hanna, Gary A Briggs, and Rayford P Hosker Jr. Handbook on atmospheric diffusion. Technical report, National Oceanic and Atmospheric Administration, Oak Ridge, TN (USA). Atmospheric Turbulence and Diffusion Lab., 1982.

[60] Steven R Hanna, Michael J Brown, Fernando E Camelli, Stevens T Chan, William J Coirier, Sura Kim, Olav R Hansen, Alan H Huber, and R Michael Reynolds. Detailed simulations of atmospheric flow and dispersion in downtown Manhattan: An application of five computational

fluid dynamics models. *Bulletin of the American Meteorological Society*, 87(12):1713–1726, 2006.

[61] Steven R Hanna, Olav R Hansen, and Seshu Dharmavaram. FLACS CFD air quality model performance evaluation with Kit Fox, MUST, Prairie Grass, and EMU observations. *Atmospheric Environment*, 38(28):4675–4687, 2004.

[62] Steven R Hanna, Olav R Hansen, Mathieu Ichard, and David Strimaitis. CFD model simulation of dispersion from chlorine railcar releases in industrial and urban areas. *Atmospheric Environment*, 43(2):262–270, 2009.

[63] Per Christian Hansen. Analysis of discrete ill-posed problems by means of the L-curve. *SIAM review*, 34(4):561–580, 1992.

[64] DM Hargreaves and Nigel G Wright. On the use of the k–ε model in commercial CFD software to model the neutral atmospheric boundary layer. *Journal of Wind Engineering and Industrial Aerodynamics*, 95(5):355–369, 2007.

[65] Nicholas S Holmes and Lidia Morawska. A review of dispersion modelling and its application to the dispersion of particles: an overview of different dispersion models available. *Atmospheric Environment*, 40(30):5902–5928, 2006.

[66] Qin-Hong Hu, Jian-Qing Weng, and Jin-Sheng Wang. Sources of anthropogenic radionuclides in the environment: a review. *Journal of Environmental Radioactivity*, 101(6):426–437, 2010.

[67] Alan Huber, W Tang, A Flowe, B Bell, K Kuehlert, and W Schwarz. Development and applications of CFD simulations in support of air quality studies involving buildings. In *Proceedings of 13th joint conference on the applications of air pollution meteorology with the Air & Waste Management Association. Vancouver, British Columbia, Canada*, 2004.

[68] IAEA. *Preparedness and response for a nuclear or radiological emergency.* Number GS-R-2 in IAEA Safety Standards Series. Vienna: International Atomic Energy Agency, 2002.

[69] Imad M Jaimoukha and Ebrahim M Kasenally. Implicitly restarted Krylov subspace methods for stable partial realizations. *SIAM Journal on Matrix Analysis and Applications*, 18(3):633–652, 1997.

[70] Lutz Janicke. A random walk model for turbulent diffusion. *Reports on Environmental Physics*, 1(1):1–10, 2000.

[71] Peter R Johnston and Ramesh M Gulrajani. Selecting the corner in the l-curve approach to tikhonov regularization. *Biomedical Engineering, IEEE Transactions on*, 47(9):1293–1296, 2000.

[72] Andrew Keats, Eugene Yee, and Fue-Sang Lien. Bayesian inference for source determination with applications to a complex urban environment. *Atmospheric environment*, 41(3):465–479, 2007.

[73] K Kenis, L Vervecken, and J Camps. Gamma dose assessment in near-range atmospheric dispersion simulations. External Report ER-242, Belgian Nuclear Research Centre, 2013.

[74] Ivan V Kovalets, Spyros Andronopoulos, Alexander G Venetsanos, and John G Bartzis. Identification of strength and location of stationary point source of atmospheric pollutant in urban conditions using computational fluid dynamics model. *Mathematics and Computers in Simulation*, 82(2):244–257, 2011.

[75] Nikolay Kozarev, Nina Ilieva, and Evgeni Sokolovski. Full scale plume rise modeling in calm and low wind velocity conditions. *Clean Technologies and Environmental Policy*, 16(3):637–645, 2014.

[76] J Labovskỳ et al. Verification of CFD pollution dispersion modelling based on experimental data. *Journal of Loss Prevention in the Process Industries*, 24(2):166–177, 2011.

[77] Claudia Landman, Jürgen Päsler-Sauer, and Wolfgang Raskob. The Decision Support System RODOS. In *The Risks of Nuclear Energy Technology*, pages 337–348. Springer, 2014.

[78] Mohamed Lateb, Christian Masson, Ted Stathopoulos, and Claude Bédard. Numerical simulation of pollutant dispersion around a building complex. *Building and Environment*, 45(8):1788–1798, 2010.

[79] Brian Edward Launder and DB Spalding. The numerical computation of turbulent flows. *Computer methods in applied mechanics and engineering*, 3(2):269–289, 1974.

[80] Ádám Leelőssy, Ferenc Molnár Jr, Ferenc Izsák, Ágnes Havasi, István Lagzi, and Róbert Mészáros. Dispersion modeling of air pollutants in the atmosphere: a review. *Central European Journal of Geosciences*, 6(3):257–278, 2014.

[81] Jörg Liesen and Zdenek Strakos. *Krylov subspace methods: principles and analysis.* Oxford University Press, 2012.

[82] David J Lucia, Philip S Beran, and Walter A Silva. Reduced-order modeling: new approaches for computational physics. *Progress in Aerospace Sciences*, 40(1):51–117, 2004.

[83] Denglong Ma, Jianqiang Deng, and Zaoxiao Zhang. Comparison and improvements of optimization methods for gas emission source identification. *Atmospheric Environment*, 81:188–198, 2013.

[84] Denglong Ma, Simin Wang, and Zaoxiao Zhang. Hybrid algorithm of minimum relative entropy-particle swarm optimization with adjustment parameters for gas source term identification in atmosphere. *Atmospheric Environment*, 94:637–646, 2014.

[85] Martin C Mahoney, Silvana Lawvere, Karen L Falkner, Yuri I Averkin, Vladislav A Ostapenko, Arthur M Michalek, Kirsten B Moysich, and Philip L McCarthy. Thyroid cancer incidence trends in Belarus: examining the impact of Chernobyl. *International journal of epidemiology*, 33(5):1025–1033, 2004.

[86] George L Mellor and Tetsuji Yamada. Development of a turbulence closure model for geophysical fluid problems. *Reviews of Geophysics*, 20(4):851–875, 1982.

[87] Manju Mohan and TA Siddiqui. Analysis of various schemes for the estimation of atmospheric stability classification. *Atmospheric Environment*, 32(21):3775–3781, 1998.

[88] AS Monin and AMf Obukhov. Basic laws of turbulent mixing in the surface layer of the atmosphere. *Contrib. Geophys. Inst. Acad. Sci. USSR*, 151:163–187, 1954.

[89] Jacques Moussafir, Olivier Oldrini, Gianni Tinarelli, John Sontowski, and Catherine M Dougherty. A new operational approach to deal with dispersion around obstacles: the MSS (Micro-Swift-Spray) software suite. In *9th International Conference on Harmonisation within Atmospheric Dispersion Modelling for Regulatory Purposes*, Garmisch, 1-4 June 2004.

[90] Hiromasa Nakayama, Klara Jurcakova, and Haruyasu Nagai. Development of local-scale high-resolution atmospheric dispersion model using large-eddy simulation. Part 3: turbulent flow and plume dispersion in building arrays. *Journal of Nuclear Science and Technology*, 50(5):503–519, 2013.

[91] S Neuman, L Glascoe, B Kosovic, K Dyer, W Hanley, and J Nitao. Event reconstruction for atmospheric releases employing urban puff model UDM with stochastic inversion methodology. In *Sixth Symp. on the Urban Environment*, page J4.6, 2006.

[92] Bahram Nour-Omid, WS Dunbar, and AD Woodbury. Lanczos and Arnoldi methods for the solution of convection-diffusion equations. *Computer methods in applied mechanics and engineering*, 88(1):75–95, 1991.

[93] Asim Önder and Johan Meyers. HPC realization of a controlled turbulent round jet using OpenFOAM. *arXiv preprint arXiv:1406.7231*, 2014.

[94] JP O'Sullivan, RA Archer, and RGJ Flay. Consistent boundary conditions for flows within the atmospheric boundary layer. *Journal of Wind Engineering and Industrial Aerodynamics*, 99(1):65–77, 2011.

[95] Ying Pan, Marcelo Chamecki, and Scott A Isard. Large-eddy simulation of turbulence and particle dispersion inside the canopy roughness sublayer. *Journal of Fluid Mechanics*, 753:499–534, 2014.

[96] Heiko Panzer, Jan Mohring, Rudy Eid, and Boris Lohmann. Parametric model order reduction by matrix interpolation. *at-Automatisierungstechnik Methoden und Anwendungen der Steuerungs-, Regelungs-und Informationstechnik*, 58(8):475–484, 2010.

[97] Won Jong Park, Moon Hee Han, and Kun Jai Lee. Analysis of the distributional effects of radioactive materials on external gamma exposure. *Annals of Nuclear Energy*, 27(8):659–671, 2000.

[98] Jürgen Päsler-Sauer. Description of the atmospheric dispersion model ATSTEP. Technical Report RODOS(WG2)-TN(97)-01, Forschungszentrum Karlsruhe, 2000.

[99] Ca A Paulson. The mathematical representation of wind speed and temperature profiles in the unstable atmospheric surface layer. *Journal of Applied Meteorology*, 9(6):857–861, 1970.

[100] Bernard Philippe and Lothar Reichel. On the generation of Krylov subspace bases. *Applied Numerical Mathematics*, 62(9):1171–1186, 2012.

[101] Stephen B Pope. *Turbulent flows*. Cambridge university press, 2000.

[102] R Srinivasan Puri and Denise Morrey. A Krylov–Arnoldi reduced order modelling framework for efficient, fully coupled, structural–acoustic optimization. *Structural and Multidisciplinary Optimization*, 43(4):495–517, 2011.

[103] R Srinivasan Puri, Denise Morrey, and Jeffrey L Cipolla. A comparison between one-sided and two-sided Arnoldi-based model order reduction (MORe) techniques for fully coupled structural-acoustic analysis. *The Journal of the Acoustical Society of America*, 121(5):3097–3097, 2007.

[104] AD Quinn, M Wilson, AM Reynolds, SB Couling, and RP Hoxey. Modelling the dispersion of aerial pollutants from agricultural buildings - an evaluation of computational fluid dynamics (CFD). *Computers and Electronics in Agriculture*, 30(1):219–235, 2001.

[105] S Raza and R Avila. A 3D Lagrangian particle model for direct plume gamma dose rate calculations. *Journal of Radiological Protection*, 21(2):145, 2001.

[106] Y Rentai. Atmospheric dispersion of radioactive material in radiological risk assessment and emergency response. *Progress in Nuclear Science and Technology*, 1:7–13, 2011.

[107] R Michael Reynolds. *ALOHA™(Areal Locations of Hazardous Atmospheres) 5.0 theoretical description.* National Oceanic and Atmospheric Administration/Hazardous Materials Response and Assessment Division. Seattle, WA, 1992.

[108] PJ Richards and RP Hoxey. Appropriate boundary conditions for computational wind engineering models using the k-ϵ turbulence model. *Journal of wind engineering and industrial aerodynamics*, 46:145–153, 1993.

[109] Andrew Riddle, David Carruthers, Alan Sharpe, Christine McHugh, and Jennifer Stocker. Comparisons between FLUENT and ADMS for atmospheric dispersion modelling. *Atmospheric environment*, 38(7):1029–1038, 2004.

[110] Patrick J Roache. Perspective: a method for uniform reporting of grid refinement studies. *Journal of Fluids Engineering*, 116(3):405–413, 1994.

[111] Carlos Rojas-Palma, Helle Karina Aage, Poul Astrup, Kim Bargholz, Martin Drews, Hans E Jørgensen, Uffe Korsbech, Bent Lauritzen, Torben Mikkelsen, Søren Thykier-Nielsen, et al. Experimental evaluation of gamma fluence-rate predictions from Argon-41 releases to the atmosphere over a nuclear research reactor site. *Radiation protection dosimetry*, 108(2):161–168, 2004.

[112] AC Rudd, Alan G Robins, Jason J Lepley, and Stephen E Belcher. An inverse method for determining source characteristics for emergency response applications. *Boundary-layer meteorology*, 144(1):1–20, 2012.

[113] Nabil Ben Salem, Lionel Soulhac, Pietro Salizzoni, and Massimo Marro. Pollutant source identification in a city district by means of a street network inverse model. *International Journal of Environment and Pollution*, 55(1):50–57, 2014.

[114] SM Salim, R Buccolieri, A Chan, S Di Sabatino, and SC Cheah. Large eddy simulation of the aerodynamic effects of trees on pollutant concentrations in street canyons. *Procedia Environmental Sciences*, 4:17–24, 2011.

[115] B Salimbahrami, B Lohmann, T Bechtold, and JG Korvink. Two-sided Arnoldi algorithm and its application in order reduction of MEMS. In *Proc. 4th Mathmod*, pages 1021–1028. Citeseer, 2003.

[116] Behnam Salimbahrami and Boris Lohmann. Krylov subspace methods for the reduction of first and second order large-scale systems. In *Proc. of 8th DFMRS conference*, pages 236–251, 2004.

[117] EY Sanchez, JE Colman Lerner, A Porta, and PM Jacovkis. Accidental release of chlorine in Chicago: Coupling of an exposure model with a computational fluid dynamics model. *Atmospheric Environment*, 64:47–55, 2013.

[118] EY Sanchez, JE Colman Lerner, A Porta, and PM Jacovkis. Emergencies planning and response: Coupling an exposure model with different atmospheric dispersion models. *Atmospheric Environment*, 79:486–494, 2013.

[119] Micheal Schatzmann, Helge Rørdam Olesen, and J Franke. *COST 732 model evaluation case studies: approach and results.* COST Office, 2010.

[120] Joseph S Scire, David G Strimaitis, and Robert J Yamartino. A user's guide for the CALPUFF dispersion model. *Earth Tech, Inc. Concord, MA*, 2000.

[121] Rosa Castañé Selga, Boris Lohmann, and Rudy Eid. Stability preservation in projection-based model order reduction of large scale systems. *European Journal of Control*, 18(2):122–132, 2012.

[122] Inanc Senocak, Julien C Thibault, and Matthew Caylor. Rapid-response urban CFD simulations using a GPU computing paradigm on desktop supercomputers. In *Eighth Symposium on the Urban Environment*, page J19.2, 2009.

[123] Maithili Sharan, Jean-Pierre Issartel, and Sarvesh Kumar Singh. A point-source reconstruction from concentration measurements in low-wind stable conditions. *Quarterly Journal of the Royal Meteorological Society*, 138(668):1884–1894, 2012.

[124] Maithili Sharan, Sarvesh Kumar Singh, and JP Issartel. Least square data assimilation for identification of the point source emissions. *Pure and applied geophysics*, 169(3):483–497, 2012.

[125] L Miguel Silveira, Mattan Kamon, Ibrahim Elfadel, and Jacob White. A coordinate-transformed Arnoldi algorithm for generating guaranteed stable reduced-order models of RLC circuits. *Computer Methods in Applied Mechanics and Engineering*, 169(3–4):377–389, 1999.

[126] Sarvesh Kumar Singh, Maithili Sharan, and Jean-Pierre Issartel. Inverse modelling for identification of multiple-point releases from atmospheric concentration measurements. *Boundary-layer meteorology*, 146(2):277–295, 2013.

[127] David H Slade. METEOROLOGY AND ATOMIC ENERGY, 1968. Technical Report No. TID–24190, Environmental Science Services Administration, Silver Spring, Md. Air Resources Labs., 1968.

[128] Lionel Sombre, Jurgen Claes, and Michelle Bouchonville. Radiological Monitoring in Belgium - Summary report 2013. Technical report, FANC, September 2014.

[129] Rob Stoll and Fernando Porté-Agel. Dynamic subgrid-scale models for momentum and scalar fluxes in large-eddy simulations of neutrally stratified atmospheric boundary layers over heterogeneous terrain. *Water Resources Research*, 42(1), 2006.

[130] Roland B Stull. *An introduction to boundary layer meteorology*, volume 13. Springer Science & Business Media, 1988.

[131] Jonathon Sumner and Christian Masson. k–ε simulations of the neutral atmospheric boundary layer: analysis and correction of discretization errors on practical grids. *International Journal for Numerical Methods in Fluids*, 70(6):724–741, 2012.

[132] Wei Tang, A Huber, B Bell, and W Schwartz. Application of CFD Simulations for Short-Range Atmospheric Dispersion. In *14th Joint Conference on the Applications of Air Pollution Meteorology with the Air and Waste Management Assoc*, 2006.

[133] Hendrik Tennekes and John Leask Lumley. *A first course in turbulence*. MIT press, 1972.

[134] DC Thoman, KR O'Kula, JC Laul, MW Davis, and KD Knecht. Comparison of ALOHA and EPIcode for safety analysis applications. *Journal of Chemical Health and Safety*, 13(6):20–33, 2006.

[135] S Thykier-Nielsen, S Deme, and T Mikkelsen. Description of the atmospheric dispersion module RIMPUFF. Technical Report RODOS(WG2)-TN(98)-02, Riso National Laboratory, PO Box, 1999.

[136] John E Till and Harry Robert Meyer, editors. *Radiological assessment. A textbook on environmental dose analysis.* Oak Ridge National Lab., TN (USA), 1983.

[137] J Tixier, G Dusserre, S Rault-Doumax, J Ollivier, and C Bourely. OSIRIS: software for the consequence evaluation of transportation of dangerous goods accidents. *Environmental modelling & software*, 17(7):627–637, 2002.

[138] Yoshihide Tominaga, Akashi Mochida, Ryuichiro Yoshie, Hiroto Kataoka, Tsuyoshi Nozu, Masaru Yoshikawa, and Taichi Shirasawa. Aij guidelines for practical applications of cfd to pedestrian wind environment around buildings. *Journal of wind engineering and industrial aerodynamics*, 96(10):1749–1761, 2008.

[139] Yoshihide Tominaga and Ted Stathopoulos. Turbulent Schmidt numbers for CFD analysis with various types of flowfield. *Atmospheric Environment*, 41(37):8091–8099, 2007.

[140] Yoshihide Tominaga and Ted Stathopoulos. Numerical simulation of dispersion around an isolated cubic building: model evaluation of RANS and LES. *Building and Environment*, 45(10):2231–2239, 2010.

[141] Yoshihide Tominaga and Ted Stathopoulos. CFD simulation of near-field pollutant dispersion in the urban environment: A review of current modeling techniques. *Atmospheric Environment*, 79:716–730, 2013.

[142] Jawad S Touma. Dependence of the wind profile power law on stability for various locations. *Journal of the Air Pollution Control Association*, 27(9):863–866, 1977.

[143] D K Trubey. *New gamma-ray buildup factor data for point kernel calculations: ANS-6.4.3 standard reference data.* Washington, DC: Nuclear Regulatory Commission, 1991.

[144] Yu-Heng Tseng, Charles Meneveau, and Marc B Parlange. Modeling flow around bluff bodies and predicting urban dispersion using large eddy simulation. *Environmental science & technology*, 40(8):2653–2662, 2006.

[145] R Tulloch and KS Smith. A theory for the atmospheric energy spectrum: Depth-limited temperature anomalies at the tropopause. *Proceedings of the National Academy of Sciences*, 103(40):14690–14694, 2006.

[146] Grégory Turbelin, Sarvesh Kumar Singh, and Jean-Pierre Issartel. Reconstructing source terms from atmospheric concentration measurements: Optimality analysis of an inversion technique. *Journal of Advances in Modeling Earth Systems*, 2014.

[147] Marek Vach and Van Minh Duong. Numerical modeling of flow fields and dispersion of passive pollutants in the vicinity of the Temelin nuclear power plant. *Environmental Modeling & Assessment*, 16(2):135–143, 2011.

[148] Lieven Vervecken, Johan Camps, and Johan Meyers. Accounting for wind-direction fluctuations in Reynolds-averaged simulation of near-range atmospheric dispersion. *Atmospheric Environment*, 72:142–150, 2013.

[149] Lieven Vervecken, Johan Camps, and Johan Meyers. Dynamic dose assessment by Large Eddy Simulation of the near-range atmospheric dispersion. *Journal of Radiological Protection*, 35(1):165–178, 2015.

[150] Derek Wade and Inanc Senocak. Stochastic reconstruction of multiple source atmospheric contaminant dispersion events. *Atmospheric Environment*, 74:45–51, 2013.

[151] Yi Wang, Hongjun Song, and Kapil Pant. A reduced-order model for whole-chip thermal analysis of microfluidic lab-on-a-chip systems. *Microfluidics and nanofluidics*, 16(1-2):369–380, 2014.

[152] Jon Wieringa. Updating the davenport roughness classification. *Journal of Wind Engineering and Industrial Aerodynamics*, 41(1):357–368, 1992.

[153] Karen Willcox, Jaime Peraire, and Jacob White. An Arnoldi approach for generation of reduced-order models for turbomachinery. *Computers & fluids*, 31(3):369–389, 2002.

[154] Michael D Williams, M Brown, David Boswell, Balwinder Singh, and Eric Pardyjak. Testing of the QUIC-PLUME model with wind-tunnel measurements for a high-rise building. In *5th AMS Urban Env Conf, Vancouver, BC, Canada LA-UR-04-4296*, 2004.

[155] Allan D Woodbury, W Scott Dunbar, and Bahram Nour-Omid. Application of the Arnoldi Algorithm to the solution of the advection-dispersion equation. *Water resources research*, 26(10):2579–2590, 1990.

[156] Peng Wu and Johan Meyers. A constraint for the subgrid-scale stresses in the logarithmic region of high Reynolds number turbulent boundary layers: A solution to the log-layer mismatch problem. *Physics of Fluids (1994-present)*, 25(1):015104, 2013.

[157] Dong Xie, Hanqing Wang, and Kimberlee J Kearfott. Modeling and experimental validation of the dispersion of 222 Rn released from a uranium mine ventilation shaft. *Atmospheric Environment*, 60:453–459, 2012.

[158] Dong Xie, Hanqing Wang, Kimberlee J Kearfott, Zehua Liu, and Shunquan Mo. Radon dispersion modeling and dose assessment for uranium mine ventilation shaft exhausts under neutral atmospheric stability. *Journal of environmental radioactivity*, 129:57–62, 2014.

[159] Eugene Yee. Theory for reconstruction of an unknown number of contaminant sources using probabilistic inference. *Boundary-layer meteorology*, 127(3):359–394, 2008.

[160] Paolo Zannetti. *Air pollution modeling: theories, computational methods, and available software.* Van Nostrand Reinhold, 1990.

[161] Keni Zhang and Allan D Woodbury. A Krylov finite element approach for multi-species contaminant transport in discretely fractured porous media. *Advances in water resources*, 25(7):705–721, 2002.

[162] Xiaoping Zheng and Zengqiang Chen. Inverse calculation approaches for source determination in hazardous chemical releases. *Journal of Loss Prevention in the Process Industries*, 24(4):293–301, 2011.

Curriculum vitae

Ir. Lieven Vervecken
°15 December 1987, Geel (Belgium)

Education

October 2011 - October 2015
Doctoral Programme in Engineering
Society and Policy Support, SCK-CEN
Department of Mechanical Engineering, KULeuven
Supervisor: Prof. Dr. Ir. Johan Meyers
Co-supervisor: Dr. Johan Camps

September 2010 - August 2011
Master of Nuclear Engineering (BNEN)
Thesis: "Transient analysis of the control/safety rods injection in MYRRHA after a power excursion incident"
Supervisor: Prof. Dr. Ir. William D'haeseleer

September 2005 - July 2010
Master of Engineering: Mechanical engineering option thermotechnical sciences
Thesis: "Extended plasma modelling for the PSI-2 device"
Supervisor: Prof. Dr. Ir. Martine Baelmans

Grants and awards

June 2014: 2nd prize Young Scientists Awards (European IRPA Societies)
December 2013: 1st prize Young Scientist Award (BVS-ABR)
September 2010: BNEN Grant (BNEN)

List of publications

International peer reviewed journal articles

- Vervecken, L., Camps, J., Meyers, J. Multi-source reconstruction of near-range atmospheric dispersion using a one-shot optimisation approach. *Boundary-Layer Meteorology*, submitted for publication.
- Vervecken, L., Camps, J., Meyers, J. (2015). Stable reduced-order models for pollutant dispersion in the built environment. *Building and Environment*, 92, 360–367.
- Vervecken, L., Camps, J., Meyers, J. (2015). Dynamic dose assessment by Large Eddy Simulation of the near-range atmospheric dispersion. *Journal of Radiological Protection*, 35, 165–178.
- Vervecken, L., Camps, J., Meyers, J. (2013). Accounting for wind-direction fluctuations in Reynolds-averaged simulation of near-range atmospheric dispersion. *Atmospheric Environment*, 72, 142–150.

Papers at international scientific conferences and symposia

- Vervecken, L., Camps, J., Meyers, J. (2013). Effect of wind fluctuations on near-range atmospheric dispersion under different types of thermal stratification. In *Proceedings of the 15th International Conference on Harmonisation within Atmospheric Dispersion Modelling for Regulatory Purposes*, Madrid, Spain, 6-9 May 2013 (art.nr. H15-54) (pp. 772–777).

Abstracts, presented at international scientific conferences and symposia

- Vervecken, L., Camps, J., Meyers, J. (2015). Fast uncertainty quantification by parametric model order reduction of dispersion in the built environment. *International workshop on Uncertainty Quantification in Computational Fluid Dynamics*, Paris, France, 18-20 May 2015.
- Vervecken, L., Gueibe, C., Camps, J., Meyers, J. (2015). Real-time simulation of the near-range atmospheric dispersion using Computational Fluid Dynamics. *NERIS Workshop 2015*, Milan, Italy, 27-29 April 2015.
- Gueibe, C., Vervecken, L., Camps, J. (2015). Inter-comparison of dose rate calculations from atmospheric dispersion models in the near range. *NERIS Workshop 2015*, Milan, Italy, 27-29 April 2015.
- Vervecken, L., Camps, J., Meyers, J. (2014). Dynamic external dose assessment by LES modeling of radioactive pollutant dispersion over an open field. *Fourth European IRPA Congress*, Geneva, Switzerland, 23-27 June 2014, Abstract No. 4-3-4.
- Vervecken, L., Camps, J., Meyers, J. (2013). Application of uncertainty quantification to wind direction fluctuations in near-range atmospheric dispersion. *Workshop on Uncertainty Quantification in Computational Fluid Dynamics*, Lyon, France, 17-18 June 2013.

Abstracts, presented at local conferences and symposia

- Vervecken, L., Camps, J., Meyers, J. (2014). Large eddy simulation of radioactive pollutant dispersion over an open field for time-dependent dose assessment. *BVS-ABR Young Generation Scientific Meeting*, 19 September 2014.

FACULTY OF ENGINEERING SCIENCE
DEPARTMENT OF MECHANICAL ENGINEERING
DIVISION OF APPLIED MECHANICS AND ENERGY CONVERSION
TURBULENT FLOW SIMULATION & OPTIMIZATION
Celestijnenlaan 300 box 2420
B-3001 Heverlee
lieven.vervecken@kuleuven.be
https://www.mech.kuleuven.be/en/tme/research/tfso